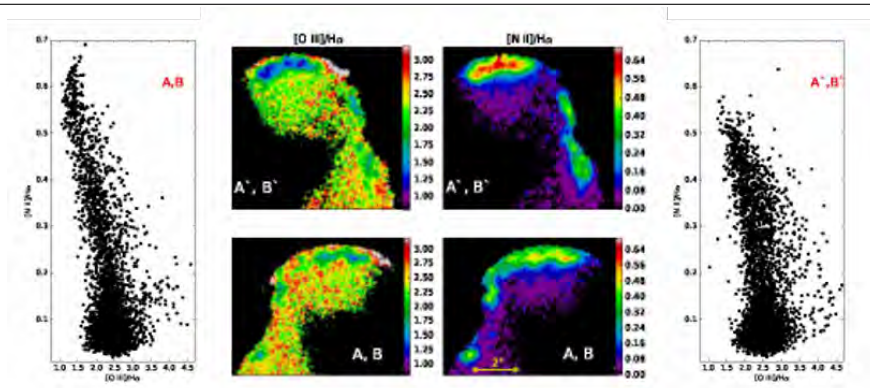

Estudio de las Propiedades Físicas de Regiones Chocadas en Nebulosas Planetarias



Director:

Dr. JORDI JOSÉ PONT

Co-Director:

Dr. DOMINGO GARCÍA SENZ

Memoria presentada para optar al grado de Doctor

Autor:

M.Sc ARJUNA CASTRILLÓN CAMACHO

UNIVERSITAT POLITÈCNICA DE CATALUNYA
DEPARTAMENT DE FÍSICA
PROGRAMA DE DOCTORAT EN FÍSICA COMPUTACIONAL I
APLICADA.

GRUP D'ASTRONOMIA I ASTROFÍSICA - GAA

Barcelona, Espanya 2021

TESIS DOCTORAL

**Estudio de las Propiedades Físicas de Regiones Chocadas en
Nebulosas Planetarias**

M.Sc ARJUNA CASTRILLÓN CAMACHO



Departament de Física

Programa de Doctorat en Física Computacional i Aplicada.

Grup d'Astronomia i Astrofísica - GAA

UNIVERSITAT POLITÈCNICA DE CATALUNYA

Barcelona, España 2021

Memoria de tesis doctoral

© ARJUNA CASTRILLON C, 2021.

Supervisor: Dr. Jordi José Pont, Departament de Física

Supervisor: Dr. Domingo García Senz, Departament de Física

Tesis Doctoral:

**ESTUDIO DE LAS PROPIEDADES FÍSICAS DE REGIONES CHOCADAS
EN NEBULOSAS PLANETARIAS**

Departament de Física

Programa de Doctorat en Física Computacional i Aplicada.

Grup d'Astronomia i Astrofísica - GAA

UNIVERSITAT POLITÈCNICA DE CATALUNYA.

ESCOLA D'ENGINYERIA DE BARCELONA EST (EEBE)

Av. d'Eduard Maristany, 16, 08019, Barcelona, Espanya

Portada: Cocientes $[\text{O III}]/H\alpha$ y $[\text{N II}]/H\alpha$, de las estructuras presentes en IC 4634 junto con sus diagramas diagnósticos.

Typeset in L^AT_EX

Barcelona, España 2021

Estudio de las Propiedades Físicas de Regiones Chocadas en Nebulosas Planetarias

ARJUNA CASTRILLÓN CAMACHO

Grup d'Astronomia i Astrofísica - GAA

Departament de Física

Programa de Doctorat en Física Computacional i Aplicada

Universitat Politècnica de Catalunya

Abstract

This work addresses several topics in the study of the episodic jets (or bullets) ejected by the central source of a Planetary nebula (PN). The presence of collimated bipolar outflows and point symmetric morphologies are commonly observed in PNe, but the underlying physical mechanism is not fully understood. To address this problem, we will focus on the determination of the observational properties of these structures (known as Fast Low Ionization Emission Regions [FLIERs] or Low Ionization Structures [LIS]) in PNe.

Firstly, I have analyzed the morphology of a sample of selected PNe in terms of anisotropic wavelet analysis applied to Hubble Space Telescope (HST) images. From this analysis, we determine the spatial distribution of FLIERs/LIS and their characteristic sizes.

Secondly, we have obtained spectroscopic data with a 2-dimensional coverage of several PNe of our sample. With these data we will be able to map the physical conditions, excitation and ionization structure of the observed bow shock-like structures (or FLIERs) which provides the effect of the photoionizing heating from the central star on shocked regions associated with bipolar jets (which we named as “irradiated shocks”).

Keywords: Planetary nebulae, Spectroscopy, bow shock, FLIERs, LIS.

Estudio de las Propiedades Físicas de Regiones Chocadas en Nebulosas Planetarias

ARJUNA CASTRILLÓN CAMACHO

Grup d'Astronomia i Astrofísica - GAA

Departament de Física

Programa de Doctorat en Física Computacional i Aplicada

Universitat Politècnica de Catalunya

Resumen

Las nebulosas planetarias juegan un papel muy importante en la evolución química de las galaxias ya que ellas son las encargadas de retornar material enriquecido al medio interestelar. Las observaciones de las nebulosas planetarias son utilizadas para determinar las abundancias químicas presentes en el medio interestelar y en todas las galaxias.

En este estudio, se analizan las propiedades y características en las estructuras a pequeña escala presentes en las nebulosas planetarias. Con este estudio se pretende evidenciar el estado evolutivo de las estrellas de masa baja e intermedia.

Este trabajo está encaminado hacia uno de los grandes temas de estudio de los episodios conocidos como “jets”, los cuales son eyectados por la estrella central de la nebulosa planetaria. La presencia de flujos bipolares colimados y morfologías con simetría puntual son comúnmente observadas en las nebulosas planetarias, pero la física presente en tales estructuras aún no es bien comprendida. Con esta tesis pretendemos enfocarnos en la determinación de las propiedades observacionales de estas estructuras llamadas FLIER's/LIS (del inglés, Fast Low Ionization Emission Regions [FLIERs] y Low Ionization Structures [LIS]) presentes en las nebulosas planetarias.

Inicialmente se analiza la morfología de una muestra de nebulosas planetarias seleccionadas de la base de datos del HST (Hubble Space Telescope), mediante la aplicación del análisis anisotrópico “wavelet”. De este análisis se determinan: primero, la distribución espacial de las estructuras de interés (FLIER's/LIS) y sus tamaños característicos; segundo, se obtienen datos espectroscópicos con cobertura bidimensional en nuestra muestra. Con estos datos podemos, trazar mapas de condiciones físicas, tales como excitación y estructura de ionización en las regiones chocadas (bow shock regions), a través de estos podemos evidenciar los efectos de la fotoionización por calentamiento provocado por la estrella central en las zonas conocidas como choques irradiados.

Palabras claves: Nebulosa planetaria, Espectroscopia, Ondas de choque, FLIERs, LIS.

Agradecimientos

En primer lugar quisiera expresar mis más sinceros agradecimientos a mi directora Dra. Angels Riera Mora, quien ya no se encuentra con nosotros y espero haga parte de una nueva generación de estrellas!! Gracias por su entrega, tenacidad y paciencia, por sus asesorías y constante apoyo. (QEPD)

A mis nuevos directores Dr. Jordi José Pont y Dr. Domingo García Senz, gracias a su apoyo en el momento oportuno, me ayudaron y motivaron a terminar mi doctorado en la Universidad Politécnica de Cataluña.

Así mismo al Grupo de Astronomía y Astrofísica - GAA- y a la Universidad Politécnica de Cataluña, por la concesión de la beca doctoral FPU.

A la Dra. Rosario López Hermoso, de la Universidad de Barcelona, pues sin su apoyo, consejo y colaboración no hubiese sido posible la finalización del segundo artículo.

A mi colega y amigo Dr. Osvaldo Aquines, por su apoyo, ánimo y colaboración cuando más necesitaba de ellos, sin recibir nunca una negativa.

A mi familia, a quienes les debo todo, gracias por su paciencia, apoyo y palabras de ánimo cuando más lo necesitaba. En especial a Jaime, mi hermano, por su gran ayuda.

A Jenny, mi esposa, amiga, socia y mi todo....gracias por su paciencia, comprensión, solidaridad, apoyo, confianza y sus palabras de ánimo cuando más se necesitaban en el desarrollo de este proyecto.

Sin el apoyo de todos y cada una de las personas mencionadas, entre otras, este trabajo nunca se habría escrito...

A todos muchas gracias!!!

Para Angels....

Y a mi estrella más brillante..Adhara

Índice general

Índice de figuras	xvii
Índice de tablas	xxv
1. Introducción	1
1.1. Nebulosas Planetarias: antecedentes	1
1.2. Evolución estelar. Post secuencia principal	5
1.2.1. Cocientes de Líneas de Emisión	12
1.2.2. Corrección de Enrojecimiento y Extinción	15
1.3. Microestructuras	17
1.3.1. Fliers, Brets, Lis, Knots, Ansaes	17
2. Motivación de la Tesis	19
2.1. Objetivos de la tesis	20
2.2. Estructura de la tesis	21
3. Observaciones y Metodología de Análisis	23
3.1. Imágenes WFPC2-HST	23
3.1.1. Descripción del instrumento	23
3.1.2. Calibración en flujo	25
3.1.3. Tratamiento de las imágenes	27
3.1.4. Selección de la muestra	28
3.1.5. Análisis Wavelet: determinación de los tamaños característicos de los FLIERs	29
3.1.6. Perfiles Unidimensionales	30
4. Análisis y simulación de la Nebulosa Protoplanetaria CRL 618	31

4.1.	Resumen de la publicación	31
4.2.	Introduction	32
4.3.	Observations	34
4.4.	Analysis	36
4.4.1.	Small-scale structure: wavelet technique	37
4.4.2.	Proper-motion measurements	39
4.5.	Results	40
4.5.1.	Small-scale structure	40
4.5.2.	Proper-motion measurements	43
4.6.	Numerical simulations	44
4.6.1.	Code description and initial setup	44
4.6.2.	Numerical results	47
4.6.3.	Comparison with observations	48
4.7.	Summary and discussion	53
5.	Análisis de una Serie Nebulosas Planetarias	59
5.1.	Resumen de la publicación	59
5.2.	Introduction	60
5.3.	Narrowband images of FLIERS in PNe	63
5.3.1.	Data Sample	63
5.3.2.	Observations and Data reduction	66
5.4.	Analysis	66
5.4.1.	Anisotropic wavelet analysis	67
5.4.2.	Emission line ratios	68
5.5.	Individual Objects	71
5.5.1.	NGC 3918	71
5.5.2.	IC 4593	72
5.5.3.	NGC 6210	75
5.5.4.	IC 4634	78
5.5.5.	NGC 6543	82
5.5.6.	NGC 7009	86
5.5.7.	Additional Objects	107
5.6.	General discussion and conclusions	110

6. Conclusiones	115
6.1. Trabajos futuros	118
Bibliografía	121
A. Apéndice 1	I
A.1. Imágenes	I
A.1.1. IC 4634	I
A.1.2. IC 4593	II
A.1.3. NGC 3918	III
A.1.4. NGC 6210	IV
A.1.5. NGC 6543	V
A.1.6. NGC 7009	VI
A.1.7. NGC 7354	VII
A.1.8. PN Hb 4	VIII
A.1.9. M 3-1	IX
A.1.10. CRL 618	X

Índice de figuras

1.1. Nebulosa M27 (Dumbbell nebula), observada por Messier en 1764. Tomada y editada de: https://esahubble.org/images/opo0306b/1	1
1.2. Diagrama de Herzprung-Russell (H-R). Ilustra las fases evolutivas de las estrellas de masa baja e intermedia (1, 5 y 10 M_{\odot}). Tomada y editada de: http://alquimiayciencias.blogspot.com.es/2013/11/cadena-proton-proton.html . . .	4
1.3. Clasificación de las estrellas por masa en la secuencia principal (parte inferior) y AGB (parte superior). Fuente: Herwig, 2005 [25]	6
1.4. Estructura interna de la estrella en fase AGB. Fuente: Lattanzio & Forestini 1999. [38]	8
1.5. Trayectorias evolutivas de combustión de H para estrellas con diferente masa inicial en modelos post-AGB. Fuente: [Blöcker, 1995].[4]	11
1.6. Curva de extinción estelar, de acuerdo con la ec. 1.6. Se ilustran dos casos, $R_v=3.1$ se refiere a un medio difuso y $R_v=5$ para el extremo de una nube molecular. Fuente Krügel (2003) [33]	15
3.1. Campo de visión WFPC2 proyectado en el plano del cielo. Fuente: Wide Field and Planetary Camera 2. Instrument Handbook [44]	24
3.2. Rendimiento del sistema WFPC2+OTA (Optical Telescope Assembly). Fuente: Wide Field and Planetary Camera 2. Instrument Handbook. [McMaster, et al. 2008], [44]	25
3.3. Curvas de transmisión para los filtros $H\alpha$ y $[N II]$. La línea punteada representa la WF/PC2 y la línea sólida la WFC3 respectivamente. Fuente: [Szyszka, et al. 2011] [66]	26

4.1.	CRL 618 in the 1998.89 (left) and 2009.60 (right) [S II] images shown to the same scale and pixel size ($0''.045$). The two frames are aligned spatially and show how the jets move outward. The images have been rotated so that the y-axis lies more or less along the J1 axis. The two jet axes used in this work are also marked. The scale is indicated by the horizontal arrow. The images are displayed with a logarithmic scale (in arbitrary units). Feature A' is labeled (see text).	35
4.2.	Bright (east) lobe in the 1998.89 (left) and 2009.60 (right) [S II] images. Several features along regions J1 and J2 are marked and labeled. Changes in the structure of the labeled features between both epochs are discussed in the text. The red arrows show the assumed identifications of corresponding knot pairs in the two epochs.	37
4.3.	Same as Fig. 4.2, but for the jets of the faint (west) lobe (labeled J1' and J2').	38
4.4.	First-epoch [S II] image of the J1 (bottom) and J2 (top) jets and the characteristic sizes of the small-scale features observed in the optical lobes ($a_{x,k}$ (left) and $a_{y,k}$ (right)) as a function of position y along the jet axis, obtained from the wavelet analysis. The $k = 1$ peaks are represented in red, $k = 2$ in green, and $k = 3$ in blue. Three examples of the compact knots (K), arc, and leading bow-shock (BS) classes are labeled.	39
4.5.	Same as Fig. 4.4, but for the faint lobe. The J1' jet is presented in the bottom panel. The J2' jet is shown in the top panel. Three examples of the compact knots (K), elongated structures (ES), and leading bow shock (BS) classes are labeled.	41
4.6.	Proper motions of the individual features in the jets of CRL 618. First-epoch [S II] image of CRL 618 together with the boxes in which the cross-correlations were made (see text). The red boxes correspond to individual knots. Features that include more than one knot (as E1, E9 and W3) are marked in green. The blue boxes were used to measure the proper motion of the J1, J2, J1' and J2' jets. The arrows show the computed proper motions. The length of each arrow is proportional to the proper motion. The vertical arrow at the top right shows a proper motion of 300 km s^{-1} .	42

4.7.	Tangential velocity as a function of distance to the central H II region. Top panel: faint lobe (J1' (circles), J2' (squares)). Bottom panel: bright lobe (J1 (circles), J2 (squares)).	44
4.8.	Synthetic [S II] emission maps obtained from models M1a (bottom panels) and M1b (top panels). The right panels display the yz projection for both models, while the left panels display the xz projection. The angle between the precession axis and the plane of sky was set to 25° for all models. The vertical color bar gives the [S II] flux in units of $\text{erg s}^{-1} \text{cm}^{-2} \text{sr}^{-1}$. The vertical and horizontal axes are given in units of 10^{17}cm	47
4.9.	As Fig. 4.8, but for models M2a (bottom panels) and M2b (top panels). . .	49
4.10.	As Fig. 4.8, but for models M3a (bottom panels) and M3b (top panels). . .	50
4.11.	Wavelet study performed on the top-left lobe or jet of the model M2b. The [S II] image obtained from this model at a $t = 120 \text{ yr}$ integration time is shown in the right panel. For each y, the location of the three maxima of the intensity map are shown as dots superimposed on this image (first maximum in red, second maximum in green and third maximum in blue). The characteristic sizes ($a_{x,k}$ in the left panel; $a_{y,k}$ in the central panel) are shown as a function of position y along the jet axis.	51
4.12.	Left panel: proper motions of the individual features in the synthetic [S II] map (model M2b) together with the boxes in which the cross-correlations were made. The red arrows show the computed proper motions. The length of each arrow is proportional to the proper motion. Right panel: proper motions of the individual knots of CRL 618, included for comparison. Both images are shown to the same spatial scale. The vertical arrow at the top right shows a proper motion of 300 km s^{-1}	52
4.13.	Tangential velocity of the individual features in the synthetic [S II] map obtained for model M1b (black), M2b (red) and M3b (green) at a $t = 120 \text{ yr}$ integration time as a function of distance to the jet injection point. . . .	53
5.1.	HST [N II] narrow-band images of the PNe of the sample (except [O III] image of NGC 6210, see text). The low-ionization features (LIS) selected for this work are NGC 3918, IC 4593, NGC 6210, IC 4634, NGC 6543 and NGC 7009. The micro-structure features are indicated by arrows	64

5.2. Additional objects. HST narrowband images [N II] images of the PNe M 3-1, Hb 4 and NGC 7354. The images have been rotated so that the symmetry axis lay parallel to the y -axis. The selected low-ionization features are marked by arrows.	65
5.3. Contour plots in zones A, A' and A'' to NGC 3918 in different emission lines, where we show the positions (x_k, y) of the maxima. The characteristic sizes $(a_{x,k}, a_{y,k})$ are shown as errorbars. Where $k = 1, 2, 3$. represent a local maximum on the intensity map. See text for more details. [N II] (top panels, color red), [O III] (middle panels, color green) and $H\alpha$ (bottom panels, color blue) of the	69
5.4. Wavelet analysis in NGC 3918 to A, A' and A'' features. Average $\langle a_x \rangle$ (left), $\langle a_y \rangle$ (middle), and the $\langle a_x \rangle / \langle a_y \rangle$ (right) ratio plotted as a function of relative distance to the central star (offsets). Blue circles correspond to $H\alpha$, green circles correspond to [O III] 5007 Å, and red circles correspond to [N II] 6584 Å.	70
5.5. [O III]/ $H\alpha$ (left panel) and [N II]/ $H\alpha$ (right panel) ratio maps of the feature jet/filament in A, A' and A''. The structure is more clear in [N II]/ $H\alpha$ of NGC 3918.	72
5.6. [O III]/ $H\alpha$ vs. [N II]/ $H\alpha$ diagnostic diagrams of morphological component (A, A' and A'') of NGC 3918. The size of the box is 64 x 128 pixels.	73
5.7. Contour plots of the knot X of IC 4593 where we show the positions (x_k, y) of the maxima. The characteristic sizes $((a_{x,k}, a_{y,k}))$ are shown as errorbars. The [N II] (top panels, red), [O III] (middle panel, greens) and the $H\alpha$ (bottom panels, blue)	74
5.8. Wavelet analysis for knot Y of IC 4593. Symbols as in Figure 5.4. See text for more details.	75
5.9. Wavelet analysis for knot X of IC 4593. Symbols as in figure 5.4. See text for more details.	76
5.10. [O III]/ $H\alpha$ (left column) and [N II]/ $H\alpha$ (right column) ratios maps of knots X (top line) and Y (bottom line) of IC 4593.	77
5.11. [O III]/ $H\alpha$ vs. [N II]/ $H\alpha$ diagnostic diagrams of morphological component X (right column) and Y (left column) of IC 4593. The size of the box is 81 x 131 pixels.	78

5.12. Profiles knots X ad Y in lines [O III], [N II] and H α of IC 4593. [O III] (Green line), [N II] (red line) and H α (Blue line).	79
5.13. Contour plots of the jet of NGC 6210, where we show the positions (x_k, y) of the maxima. The characteristic sizes $((a_{x,k}, a_{y,k}))$ are shown as errorbars. [N II] (top panels, red), [O III] (middle panels, green) and H α (bottom panels, blue).	80
5.14. Wavelet analysis to N jet in NGC 6210. Symbols as in figure 5.4 See text for more details.	81
5.15. [O III]/H α (left), [N II]/H α (middle) and [O III]/[N II] (right) emission line ratio maps of the northern FLIER of NGC 6210.	82
5.16. [O III]/H α Vs.[N II]/H α diagnostic diagram of morphological component of N jet of NGC 6210. The size of the box is 81 x 131 pixeles	83
5.17. Profiles in emission lines of [O III] (red line) , [N II] (green line) and H α (blue line) to north structure in NGC 6210.	84
5.18. Contour plots of the structures A and B of IC 4634 where we show the positions (x_k, y) of the maxima. The characteristic sizes $((a_{x,k}, a_{y,k}))$ are shown as errorbars. [N II] (top panels, red), [O III] (middle panels, green) and H α (bottom panels, blue)	85
5.19. Wavelet analysis to IC 4643 in A and B features. Average $\langle a_x \rangle$ (left), $\langle a_y \rangle$ (middle), and the $\langle a_x \rangle / \langle a_y \rangle$ (right) ratio plotted as a function of relative distance to the central star. Blue circles correspond to H α , green circles correspond to [O III] 5007 Å, and red circles correspond to [N II] 6584 Å. See text for details.	86
5.20. Wavelet analysis in A' and B' features. Symbols and distribution as in figure 5.19.	86
5.21. [O III]/H α (left column) and [N II]/H α (right column) ratios of the outer bow-shocks of IC 4634. The features A and B are plotted in first line in the panel, while the features A' and B' are plotted in the second line of panel.	87
5.22. [O III]/H α Vs. [N II]/H α diagnostic diagrams of morphological component A, B (right column) and A', B' (left column) of IC 4634. The size of the box in this case is different, the left figure is 131 x 101 pixels and the other box is 111 x 101 pixels.	88

5.23. Profile A and A' in lines [O III] (green line), [N II] (red line) and H α (blue line). In the center shows the central source.	89
5.24. Profile B and B' in lines [O III], [N II] and H α . Colors as in figure 5.23 . . .	90
5.25. Contour maps of the feature J' to NGC 6543. [N II] (top in red), [O III] (middle in green) and H α (bottom). Symbols as in figure 5.13.	90
5.26. Contour maps of the features J and F to NGC 6543. [N II] (top in red), [O III] (middle in green) and H α (bottom). Symbols as in figure 5.13.	91
5.27. Wavelet analysis to J' feature. Average $\langle a_x \rangle$ (left), $\langle a_y \rangle$ (middle), and the $\langle a_x \rangle / \langle a_y \rangle$ (right) ratio plotted as a function of relative distance to the central star. Blue circles correspond to H α , green circles correspond to [O III] 5007 Å, and red circles correspond to [N II] 6584 Å. See text for more details.	92
5.28. Wavelet analysis to F structure. Symbols as in figure 5.27 See text for more details.	93
5.29. [O III]/H α (left panels) and [N II]/H α (right panels) ratio maps of the feature J' (a and b) and features J (c and d) of NGC 6543.	94
5.30. [O III]/H α Vs. [N II]/H α diagnostic diagrams of morphological component J' (right column) and J (left column) of NGC 6543 . The size of the box is 41 x 60 pixels.	95
5.31. J and J' profiles in emission lines [O III], [N II] and H α	96
5.32. [O III]/H α (left panels) and [N II]/H α (right panels) ratio maps of the feature F' (first row) and features F (second row) of NGC 6543.	97
5.33. [O III]/H α Vs. [N II]/H α diagnostic diagrams of morphological component F' (right column) and F (left column) of NGC 6543. The size of the box is 176 x 112 pixels.	98
5.34. F' and F Profiles in emission lines [O III], [N II] and H α	99
5.35. Contour maps to the feature K4 (A and B) to NGC 7009. [N II] (top, red), [O III] (middle, green) and H α (bottom, red). Symbols as in figure 5.13. . .	100
5.36. Wavelet analysis to NGC 7009. Symbols as in figure 5.19 See text for more details.	101
5.37. Contour maps to the feature K1 to NGC 7009. [N II] (top, red), [O III] (middle, green) and H α (bottom, red). Symbols as in figure 5.13.	102

5.38. Wavelet analysis to K1 structure. Symbols as in figure 5.19 See text for more details.	103
5.39. [O III]/H α (left panels) and [N II]/H α (right panels) ratio maps of the feature K4 (A and B) (first row) and features K1 (second row). In the [O III]/H α is not visible the structure B of NGC 7009.	104
5.40. [O III]/H α Vs. [N II]/H α diagnostic diagrams of morphological component K4 (right column) and K1 (left column) of NGC 6543 . The size of the box for both structure is 64 x 128 pixels.	105
5.41. Profile in emission lines [O III] (green line), [N II] (red line) and H α (blue line) to K1 an K4 structures.	106
5.42. Contour plots of the emission lines of M 3–1 where we showing the positions (x_k, y) of the maxima. The characteristic sizes $((a_{x,k}, a_{y,k}))$ are shown as errorbars. [N II] (top panels, red) and H α (bottom panels in blue). Symbols as in figure 5.18.	107
5.43. Features of wavelets in A and B in M 3-1. Blue circles correspond to H α and red circles correspond to [N II] 6584 Å. See text for more details. . . .	108
5.44. Feature wavelet analysis to A' in M 3-1. Symbols as in figure 5.43 See text for more details.	108
5.45. Wavelet analysis in Hb 4 to N structure. Symbols as in figure 5.43 See text for more details.	109
5.46. Wavelet analysis in Hb 4 to S structure. Symbols as in figure 5.43 See text for more details.	110
5.47. [N II] contour plots of the N-jet (left) and S-jet (right) to NGC 7354, where we show the positions of the first maxima. See text for more details. . . .	111
6.1. Análisis wavelet, donde se visualiza el patrón de la forma “V”. Fuente propia.	115
6.2. Análisis wavelet, donde se visualiza el patrón de la forma diagonal. Fuente propia.	116
6.3. Cocientes de líneas de emisión. Fuente propia.	117
6.4. Diagramas diagnósticos, donde se visualizan características similares. Fuente propia.	118
6.5. Imagen de una sección espectroscópica 3D de NGC 3918. Fuente propia. . .	119
A.1. IC 4634. Fuente: https://esahubble.org/images/potw1003a/	I

A.2. IC 4593. Fuente: https://esahubble.org/images/opo0733d/	II
A.3. NGC 3918. Fuente: https://esahubble.org/images/potw1015a/	III
A.4. NGC 6210. Fuente: https://esahubble.org/images/opo9836f/	IV
A.5. NGC 6543. Fuente: https://esahubble.org/images/heic0414a/	V
A.6. NGC 7009. https://esahubble.org/images/opo9738g/	VI
A.7. NGC 7354. https://esahubble.org/images/potw1250a/	VII
A.8. PN Hb4. https://faculty.washington.edu/balick/PNIC/PNimages_by_galcoord/003-102.9.Hb4hst.jpg	VIII
A.9. M 3-1. https://www.flickr.com/photos/geckzilla/43710246990/in/photolist-29AwrA7	IX
A.10. Nebulosa protoplanetaria CRL 618. Fuente: https://esahubble.org/images-heic0004a/	X

Índice de tablas

1.1. Algunas líneas nebulares sensitivas a la temperatura. (\AA). Tomado de Dopita, M. Sutherland, R. 2005 [11]	13
1.2. Potenciales de ionización para elementos comunes en eV para diferentes estados de ionización	14
3.1. Características de las cámaras CCD de WFPC2	23
3.2. Parámetros fotométricos Photflam, rectw, exptime y $\Delta\lambda$ de calibración para los filtros F656N, F658N, F502N	27
3.3. Muestra de las Nebulosas Planetarias obtenidas del archivo del HST (MAST) y nebulosa protoplanetaria	28
4.1. HST [S II] images of CRL 618.	33
4.3. Parameters employed in the models.	46
4.2. Proper motions of identified features.	57
5.1. Features list of the sample of Planetary nebula	61
5.2. [O III]/H α type, shape and micro-structures	63

Introducción

1.1. Nebulosas Planetarias: antecedentes

El estudio de las nebulosas planetarias se inició con la observación realizada por Charles Messier en 1764 del objeto al que designó M27 (Dumbbell Nebula) (fig 1.1) en el catálogo Messier de 1781 [Messier][47]. En 1784 dicho catálogo contenía otras tres nebulosas planetarias, M57 (Ring Nebula), M76 (Little Dumbbell) y M97 (Owl) [Habing y Olofsson; 2004] [21] observadas entre 1780 y 1781 por P. Méchain, A. Darquier y C. Messier, junto con otros objetos tales como galaxias y cúmulos de estrellas.



Figura 1.1: Nebulosa M27 (Dumbbell nebula), observada por Messier en 1764. Tomada y editada de: <https://esahubble.org/images/opo0306b/1>

El término nebulosa planetaria fue propuesto por W. Herschel, en el siglo XVIII tras observar objetos como NGC 7662, NGC 3242 y NGC 7009, los cuales aparecían como

discos borrosos de luz en los incipientes telescopios de la época, aspecto muy similar al del planeta Urano descubierto por él mismo. Inicialmente se pensó que las nebulosas eran cúmulos de estrellas muy lejanos que no podían ser resueltos pero la distinción se hizo evidente con la obtención de los primeros espectros.

En 1790, Herschel al observar NGC 1514 dedujo que estos objetos eran estrellas rodeadas de gas y polvo. En 1864, W. Huggins obtuvo por primera vez un espectro de la nebulosa planetaria NGC 6543 [Huggins; 1864] [27], cien años después del descubrimiento de las primeras nebulosas planetarias. El espectro de NGC 6543 estaba dominado por tres líneas de emisión. La primera línea identificada, correspondía a la denominada serie de Balmer del H ($H\beta$) y adicionalmente se detectaban dos líneas atribuidas a un elemento desconocido al cual llamaron Nebulium. En 1867, Secchi mostró que estas tres líneas eran comunes a este tipo de objetos [Secchi; 1867][61].

En observaciones posteriores se detectaron líneas más débiles que, inicialmente, no se identificaron. Bowen en 1928 [Bowen; 1928][5] identificó las líneas que previamente habían asociado con el nuevo elemento Nebulium. Determinó que correspondían a transiciones prohibidas de líneas en emisión de estados ionizados de O^{+2} ($[O III]$), identificando también líneas de N^+ ($[N II]$) y O^+ ($[O II]$). Ahora se sabe que estas líneas no se observaban en los laboratorios terrestres, ya que las transiciones prohibidas son posibles únicamente en regiones de muy baja densidad donde la desexcitación colisional es dominante.

A principios del siglo XX, se realizaron importantes avances en el campo de la física atómica que a su vez permitieron profundizar en el estudio de las nebulosas planetarias. En el observatorio de Harvard, Margaret Mayall y Annie Jump Canon bajo la dirección de E. Pickering, obtuvieron espectros tras ubicar un prisma en frente del telescopio identificando las líneas de emisión características de las nebulosas planetarias [Griffiths; 2012][19].

En 1918, Heber Curtis en el observatorio Lick, en California, determinó la posición de muchas nebulosas planetarias en la Vía Láctea y, utilizando la espectroscopia, encontró que las nebulosas planetarias eran más parecidas a estrellas de tipo tardío que a objetos jóvenes. Menzel en 1926, sugirió que las nebulosas son ionizadas por el flujo de fotones Lyman estelares [Menzel; 1926][46], idea que fue inicialmente sugerida por Herschel en 1791 quien postuló que las nebulosas planetarias reciben su energía de las estrellas cercanas [Herschel;1791][24]. Idea que fue respaldada por Hubble en 1922 [Hubble, 1922][26], al encontrar una correlación entre el diámetro nebular y la magnitud de la estrella central.

Posteriormente, Zanstra en 1927 desarrolló el método que permite estimar la temperatura

de la estrella central a partir del cociente del flujo nebular de $H\beta$ sobre el continuo estelar y obtuvo que las estrellas centrales de las nebulosas planetarias tienen temperaturas altas, muy superiores a las de otras estrellas [Zanstra, 1927] [75].

La investigación sobre las nebulosas planetarias se centró en cuatro áreas principales en los siguientes años: (1) descubrimiento de nuevas nebulosas con líneas de emisión a partir de imágenes; (2) uso de la espectroscopia para estudiar la física nebular (fotoionización, recombinación y excitación colisional) y determinar las abundancias químicas en las nebulosas planetarias; (3) la localización de las estrellas de nebulosas planetarias en la evolución estelar y (4) mecanismos de formación de las nebulosas.

El verdadero estado evolutivo de las nebulosas planetarias fue propuesto cualitativamente en 1956 por Shklovsky, quien por primera vez sugirió que las nebulosas planetarias son descendientes de las gigantes rojas y que sus estrellas centrales evolucionan a enanas blancas [Shklovsky, 1956] [62]. El hecho que las velocidades de expansión de las nebulosas planetarias fuesen similares a las velocidades de escape de las gigantes rojas llevó a Abell y Goldreich en 1966 a sugerir que las nebulosas planetarias resultan de la expulsión de la envoltura presente en las estrellas gigantes rojas [Abell & Goldreich; 1966][1].

El siguiente problema planteado era el mecanismo responsable de la expulsión de la nebulosa. A lo largo de los años se propusieron varios modelos. La eyección podía ser el resultado de inestabilidades dinámicas [Roxburgh, 1967; Lucy, 1967; Paczynski, 1968][56, 41, 52]; inestabilidades pulsacionales [Wood, 1974][74]; oscilaciones de la envoltura debido a inestabilidades térmicas en el núcleo [Smith, 1972][65]; presión de radiación [Faulkner, 1970; Finzi, 1971][12, 14] y pulsos térmicos [Harm, 1975; Trimble, 1978][23, 67]. Todos estos modelos de eyección instantánea presentaban el mismo problema, eyectaban demasiada masa o una masa inferior a la requerida (entre otros problemas).

Shklovsky en 1956 [ShklovskyA, ShklovskyB][62, 63] e independientemente Abell y Goldreich en 1966, mostraron como las estrellas AGB podían eyectar sus envolturas mediante inestabilidades estructurales. En una década, la idea de que los “flashes” y/o las pulsaciones en la superficie podrían expulsar materia, ganó popularidad, aunque el mecanismo involucrado permanecía siendo poco claro.

El problema se resolvió con el descubrimiento de la pérdida de masa estelar que tiene lugar durante la fase AGB. Esta pérdida de masa se manifiesta mediante la emisión molecular y la emisión en el infrarrojo debida al polvo. Smith y Aller en 1969 encontraron que las estrellas centrales de las nebulosas planetarias presentaban vientos con velocidades cercanas a los

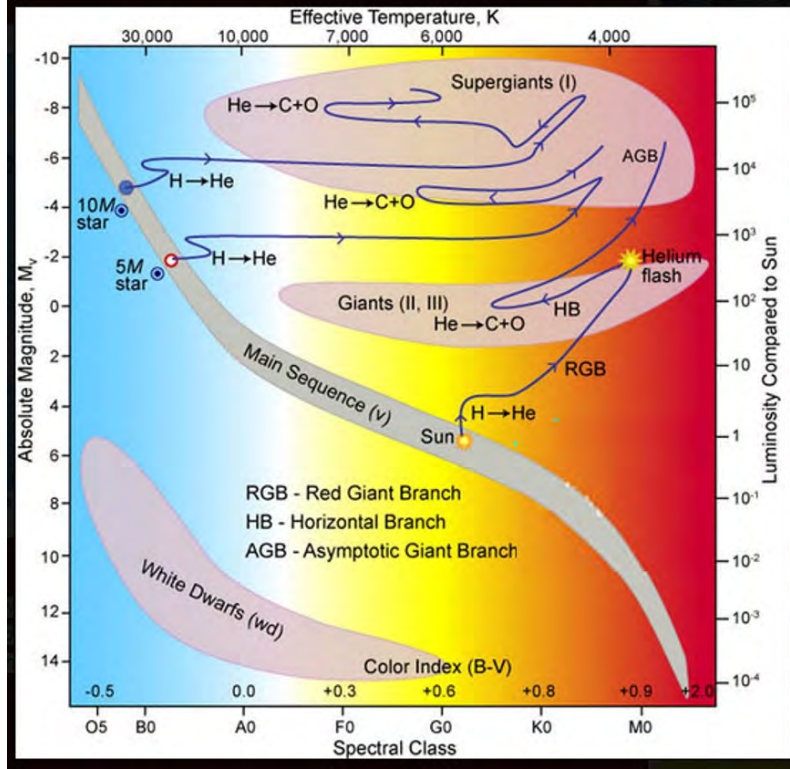


Figura 1.2: Diagrama de Hertzsprung-Russell (H-R). Ilustra las fases evolutivas de las estrellas de masa baja e intermedia (1, 5 y 10 M_\odot). Tomada y editada de: <http://alquimiayciencias.blogspot.com.es/2013/11/cadena-proton-proton.html>

$\sim 1000 \text{ km s}^{-1}$ [Smith, 1969][64]. En los siguientes años 1970 y 1971 Paczyński desarrolló un modelo estático de estrellas AGB con diferentes masas de H en su envoltura. Encontró que la estrella no evolucionaba hacia el azul hasta que la masa de H era inferior a $10^{-3} M_\odot$ (para un núcleo de $0.6 M_\odot$). Si la masa del H es inferior a este valor la estrella se moverá horizontalmente hacia la izquierda del diagrama H-R (fig 1.2) manteniendo su luminosidad constante. Adicionalmente determinó que la temperatura estelar de una gigante roja no cambia hasta que toda su envoltura es expulsada, instante en que se inicia la transición a la fase de nebulosa planetaria. Con el modelo planteado por Paczyński se inició la era moderna en el estudio de la evolución de las nebulosas planetarias [Paczyński, 1970, 1971][50, 51].

Posteriormente en 1978, Kwok y otros colaboradores propusieron que la nebulosa planetaria se forma por la interacción de los vientos estelares provenientes del núcleo de la nebulosa planetaria con los vientos liberados en la fase de gigante roja [Kwok, 1978][34], mecanismo conocido como modelo de vientos interactuantes. Para este mismo año, se creía que la pérdida de masa cesaba en este punto y que a partir de ese momento el cascarón

se expandía isotrópicamente. Ahora está bien establecido, por observaciones en el rango UV que las estrellas AGB y las post-AGB pierden masa a razón de $10^{-5} M_{\odot} \text{ yr}^{-1}$ y con velocidades cercanas a los 10 km s^{-1} [Kwok, 2000][35].

1.2. Evolución estelar. Post secuencia principal

Una nebulosa planetaria es una burbuja o toroide de gas ionizado producido por una estrella de masa baja o intermedia ($0.8 - 8.0 M_{\odot}$) [Maciel et al., 2009] [42]. Las estrellas con masa en este intervalo dominan la población estelar de nuestra galaxia. La importancia de estas estrellas se ve incrementada por la aportación de diferentes elementos al medio interestelar, resultado de procesos de nucleosíntesis, que contribuyen a la evolución química del universo. Durante su evolución, más allá de la secuencia principal (MS), estas estrellas pierden masa en forma de vientos estelares contribuyendo al enriquecimiento del medio interestelar con los elementos sintetizados (producto de la combustión de H y He) en su interior.

Los procesos de nucleosíntesis más significativos en estrellas de masa baja e intermedia tienen lugar cuando las estrellas alcanzan la rama de gigantes. El primer proceso de dragado ocurre cuando las estrellas ascienden por la rama de gigantes rojas (RGB) (fig 1.2). El dragado es el proceso convectivo de mezcla debido al cual el material resultado de la combustión de H alcanza la superficie estelar y es eyectado al medio interestelar en forma de pérdida de masa o de vientos. Las estrellas más masivas en el intervalo de masas seleccionado, sufren un segundo proceso de dragado cuando se agota el He en el núcleo, lo cual ocurre cuando la estrella inicia por segunda vez el ascenso por la rama de gigantes (a la que se designa como rama asintótica de gigantes, AGB). Durante la fase AGB se producen los mayores cambios en la composición química de la envoltura estelar. Los procesos de nucleosíntesis están gobernados por las inestabilidades térmicas que se producen en las capas donde tiene lugar la combustión de He (denominadas pulsos térmicos). Los productos de la combustión (básicamente C) alcanzan la superficie estelar como resultado de procesos recurrentes de dragado (conocido como tercer dragado). Durante el tercer dragado los elementos pesados, producto del proceso lento de captura de neutrones (s-process) alcanzan la superficie estelar. Durante los pulsos térmicos se produce la pérdida de masa o eyección de la envoltura estelar, material que formará la nebulosa planetaria.

A continuación se presenta un resumen de la evolución de estrellas con masas entre 0.8

y $8 M_{\odot}$. No es nuestro objetivo relatar de forma exhaustiva el conocimiento actual sobre evolución estelar para estrellas con estas masas. Para descripciones más completas, el lector se puede remitir a Kippenhahn y Weigert (1990); Habing y Olofsson (2004); Herwig (2005); Iliadis (2007) y Boer y Seggewiss (2008).

Todas las estrellas inician su vida en la secuencia principal convirtiendo H en He en su núcleo. Las estrellas de masa baja, según Salaris y Cassisi (2005) ($M=1.3 M_{\odot}$) [Salaris and Cassisi, 2005] [57] ó según Iben (1995) y/o Schonberner (1982) reportan un valor diferente ($M \leq 2.5 M_{\odot}$), transforman el H en He mediante el ciclo “PP”, mientras que en las estrellas de mayor masa ($2.5 - 8 M_{\odot}$) el ciclo “CNO” domina la combustión de H [Iben, 1995, Schonberner, 1981] [28, 59]. La temperatura y densidad centrales crecen debido al aumento de peso molecular asociado a la conversión de H en He hasta que se agota el H del núcleo. Una vez agotado el H en el núcleo de la estrella, éste núcleo se contrae y la estrella abandona la secuencia principal y sube por la rama de gigantes en el diagrama HR (ver fig 1.2). El aumento de tamaño de la estrella hasta alcanzar dimensiones gigantes se debe a que la combustión de H tiene ahora lugar en una capa que rodea al núcleo de ^4He .

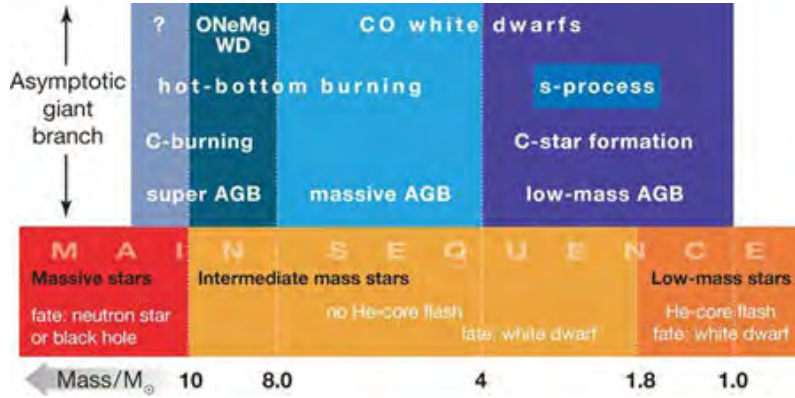


Figura 1.3: Clasificación de las estrellas por masa en la secuencia principal (parte inferior) y AGB (parte superior). Fuente: Herwig, 2005 [25]

Una vez el núcleo es de He, la ignición del núcleo depende de la masa inicial de la estrella (ver fig 1.3), si la masa inicial es menor de $1.8 M_{\odot}$ el núcleo de He llegará a ser electrónicamente degenerado cuando la estrella evolucione al extremo de la zona RGB [Herwig, 2005] [25].

En la fase RGB no hay proceso de fusión en el núcleo, por tanto éste se contrae por la acción de la gravedad y su temperatura aumenta. Este incremento de temperatura, provoca la expansión y el enfriamiento de la envoltura estelar que en consecuencia, pasa

a ser convectiva. La estrella no puede enfriarse más e inicia su ascensión por la rama de gigantes (ver fig 1.2). La convección pasa a dominar el transporte de energía en la envoltura. La envoltura convectiva penetra en la zona de combustión y como resultado los productos de la combustión de H llegan a la superficie estelar. Se produce el primer dragado, que provoca un enriquecimiento de ^4He y de los productos del ciclo CNO, fundamentalmente ^{14}N y ^{13}C así como una disminución de ^{12}C y ^{16}O . La estrella tiene ahora un radio ≈ 100 veces el radio que tenía en la secuencia principal y la mayor parte de la masa del núcleo se encuentra en una pequeña fracción del radio total. Como consecuencia, las capas de la estrella están débilmente ligadas al núcleo y se produce un aumento del ritmo de pérdida de masa.

Durante el ascenso por la zona RGB, las estrellas de masa baja e intermedia experimentan el primer proceso de dragado. Simultáneamente, el núcleo de He continua contrayéndose y se calienta y, en el caso de estrellas de baja masa, deviene degenerado. La fase RGB, finaliza cuando se alcanzan las temperaturas a las cuales se produce la ignición central de He ($\sim 10^8$ K).

La combustión de He en las estrellas de masa intermedia se produce en condiciones quiescentes. Para estas estrellas con masas entre $2 M_{\odot} \leq M \leq 8 M_{\odot}$, el núcleo se contraerá y por consiguiente la temperatura se incrementará hasta alcanzar el valor suficiente ($\approx 10^8$ K) para que se inicie la fusión del He. Por otro lado, en las estrellas con $M < 2 M_{\odot}$ eventualmente se encienden las reacciones triple- α en el punto de máxima temperatura y bajo las condiciones de degeneración. Cuando se inicia la fusión de He en C aumenta la temperatura del plasma ya que el núcleo no se puede expandir debido a su estado de degeneración. El aumento de temperatura repercute en el ritmo de combustión lo cual provoca que la ignición se produzca de forma violenta dando lugar al “core He flash” (“ignición súbita del núcleo de He”). En las estrellas RGB con masas superiores a $2 M_{\odot}$ la combustión del He tiene lugar en el núcleo no degenerado. La estrella (al igual que las estrellas de baja masa) quema el He en el núcleo convectivo mientras que se enciende la combustión de H en una capa externa. La competición entre estas dos fuentes de energía determina la presencia y extensión del camino hacia el azul que presentan estas estrellas en el diagrama HR. Los siguientes flashes de He son más débiles y finalmente se establece la combustión de He en el núcleo de forma estable. Como resultado la estrella se enfría rápidamente y disminuye su luminosidad, moviéndose hacia la rama horizontal (HB). La estrella en esta etapa quema ^4He en el núcleo convectivo e H en una capa exterior al

núcleo. La combustión del ^4He provoca el aumento de la fracción de masa de ^{12}C y ^{16}O (a través de la reacción $^{12}\text{C}(\alpha, \gamma)^{16}\text{O}$).

Una vez agotado el He del núcleo la estrella asciende por la rama de gigantes por segunda vez. La energía de la estrella proviene de la combustión de He en un cascarón (que rodea al núcleo C-O) y de una capa exterior donde se produce la combustión de H. Sobre esta capa se encuentra la envoltura convectiva. Este es el inicio de la fase AGB.

Durante la etapa temprana de la fase AGB (E-AGB) la estructura de la estrella es cualitativamente similar, independientemente de la masa estelar. La estrella consiste en un núcleo degenerado de C-O, rodeado de dos cascarones separados donde tiene lugar la combustión de He y de H. La mayor parte del volumen estelar está ocupado por la envoltura convectiva exterior (fig 1.4). En esta etapa la energía proviene de la combustión de la capa de He [Lattanzio, 2003] [36].

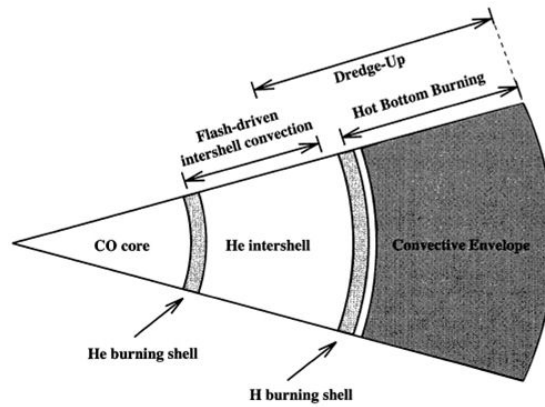


Figura 1.4: Estructura interna de la estrella en fase AGB. Fuente: Lattanzio & Forestini 1999. [38]

A medida que la estrella asciende por la AGB, la capa de He se reduce y, eventualmente, pasa a ser térmicamente inestable. Se dice que la estrella inicia la etapa de pulsos térmicos (conocida como fase TP-AGB) [Kwok, 2000; Blöcker, 1995a] [35],[4].

La fase evolutiva TP-AGB se caracteriza por la presencia de largos periodos en los cuales se produce la combustión en la capa de H (etapa conocida como fase entre pulsos), interrumpida por las inestabilidades térmicas en la capa de He que se producen cada $\approx 10^5$ años. La generación de energía durante la fase de “flash” es debida principalmente a la reacción triple- α (transformación de He en C); esta liberación de energía se produce violentamente provocando luminosidades $\leq 10^8 L_{\odot}$ durante un corto período de tiempo. La energía producida por el “flash” provoca la aparición de una región convectiva entre las capas de He

e H (zona entre capas, “intershell”), rica en ^4He y ^{12}C . Esta convección homogeniza las abundancias en esta región. Cuando la energía liberada en un pulso térmico se reduce se inicia la fase de apagado, durante la cual la enorme cantidad de energía producida durante el pulso térmico provoca la expansión de la estrella produciendo el enfriamiento del material exterior a la capa de He. Este enfriamiento provoca que finalice la combustión en la capa de H [Lattanzio, 2003; Salas, 2003][37, 58].

Al finalizar cada uno de los pulsos térmicos se produce una fase de dragado (conocida como tercer dragado). El tercer proceso de dragado es el responsable de los cambios en la composición de la superficie en estrellas de baja masa ($\leq 4 M_{\odot}$) y tiene consecuencias importantes en la nucleosíntesis de estrellas AGB de masa intermedia al producir el C que se convertirá en N en el proceso HBB (“Hot Bottom Burning”). En esta fase la envoltura convectiva exterior alcanza las regiones “intershell” donde previamente se ha producido un proceso de convección que ha mezclado el material. Durante esta etapa el carbono y otros productos resultado de la combustión de He alcanzan la superficie estelar. Los pulsos térmicos y los procesos de dragado se producen varias veces durante la fase TP-AGB. Durante cada proceso de dragado el ^{12}C formado en la capa de He alcanza la envoltura exterior, alterando el cociente C/O en la superficie, explicando la transición de estrellas tipo M a estrellas tipo C [De Boer; Seggewiss; 2008] [8]. Durante el tercer dragado los elementos pesados (Ne, Mg, Si) producidos en el proceso lento de captura de neutrones (s-process) alcanzan la superficie estelar [Iben, 1975; Karakas, 2002; Lattanzio, 2003] [29, 32, 37].

En las estrellas AGB con masas superiores a $\approx 4 M_{\odot}$ (el límite varia con la metalicidad) se produce la combustión nuclear en las zonas internas de la envoltura convectiva. Este proceso se conoce como “hot-bottom burning” (HBB). El HBB se activa cuando la temperatura en la base de la envoltura convectiva es superior a 2×10^7 K y entonces transforma el ^{12}C dragado en ^{14}N (ciclo CN) [Iben, 1995] [28] de una manera muy eficiente, lo cual evita la formación de una estrella rica en C [Cardelli et al, 1989; Pijpers & Habing, 1989] [6, 53], y adicionalmente en el HBB se crean elementos como Ne, Na, Mg, Al, Si y tendrán lugar reacciones con captura de protones. Mientras que para estrellas con $M \leq 4 M_{\odot}$ la zona convectiva no es tan profunda ni tan eficiente como en el caso anterior y por tanto no hay transporte de masa entre los cascarones de He y C [De Boer y Seggewiss, 2008] [8]. Es importante mencionar que durante la fase AGB la estrella tiene un ritmo de pérdida de masa de 10^{-7} a $10^{-6} M_{\odot} \text{ yr}^{-1}$ y una velocidad de expansión 10 a 20 km s^{-1} , formando un

viento lento. En la última etapa de la fase AGB, la estrella sufre un incremento en el ritmo de pérdida de masa (con valores entre 10^{-5} y $10^{-4} M_{\odot} \text{ yr}^{-1}$) lo cual constituye la fase de superviento [Vassiliadis & Wood, 1993] [70]. Durante la fase de superviento se expulsa la mayor parte del material que forma la envoltura de la estrella, se detiene la fusión y la estrella se contrae.

La estrella está entonces rodeada por el material expulsado, formando una envoltura circumestelar (CSE) de gas y polvo en expansión. En esta etapa, se ha formado una estrella post-AGB (a la que también nos referiremos como nebulosa proto-planetaria (PPN)) [Weidmann et al., 2015; Kamath et al., 2015, Kwok, 2000] [72, 31, 35]. A continuación, la temperatura de la estrella central aumenta en escalas de tiempo que dependen de la masa estelar.

Cuando la masa total de la nebulosa es aproximadamente igual a la masa del núcleo, es decir la masa de H que conforma la envoltura es despreciable, la envoltura se contrae, de manera que la energía gravitatoria liberada mantiene la temperatura necesaria para mantener la combustión de H en la base del cascarón. La estrella se desplaza hacia la izquierda en el diagrama HR (fig. 1.2) a, aproximadamente, luminosidad bolométrica constante, cuyo valor depende de la masa del núcleo [Paczynski, 1971] [51].

Cuando el núcleo estelar, (en adelante estrella central CS), alcanza temperaturas ≥ 25.000 K, el material circumestelar se ioniza debido a la radiación ultravioleta producida por la CS, de manera que la envoltura eyectada es visible como nebulosa planetaria. La temperatura máxima que alcanza la CS, típicamente entre 100000 y 250000 K, depende también de su masa [Tylenda, 1989] [68], la cual normalmente se encuentra entre los 0.6 y 1 M_{\odot} . Finalmente, cesa la combustión de H y la luminosidad estelar disminuye, descendiendo por el camino de enfriamiento hacia la fase de enana blanca (ver fig. 1.5). El tiempo que transcurre entre la finalización del superviento y el inicio de la fase de enana blanca depende críticamente de la masa de la envoltura de H [Tylenda, 1989] [68]. Por tanto, la evolución de la estrella depende fuertemente del mecanismo de eyección. Se obtiene que el tiempo de combustión de H es de $\sim 10^4$ años para una CS de masa 0.6 M_{\odot} y de tan solo 25 años para un núcleo de masa 1 M_{\odot} (ver figura 1.5); esta etapa es, por tanto, corta comparada con el tiempo de vida de la estrella. A su vez, la nebulosa planetaria en expansión acaba formando parte del medio interestelar.

Existe un grupo de estrellas centrales de nebulosas planetarias (30 %) que son deficientes en H y presentan intensas líneas de emisión de elementos producto de la fase de combustión de

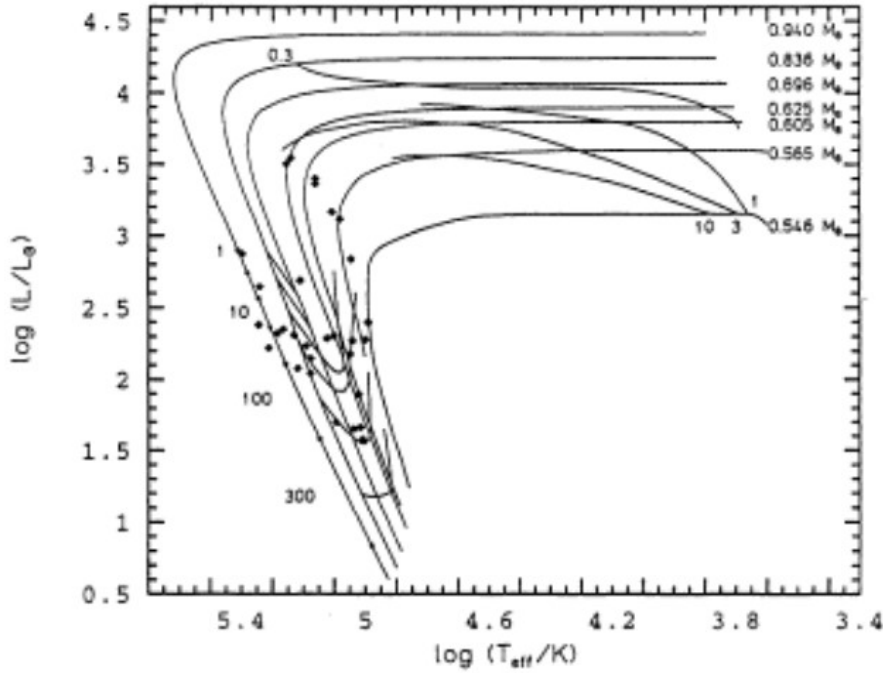


Figura 1.5: Trayectorias evolutivas de combustión de H para estrellas con diferente masa inicial en modelos post-AGB. Fuente: [Blöcker, 1995].[4]

He (C, N, O), indicando la presencia de vientos estelares con altas tasas de pérdida de masa [Acker & Neiner, 2003][2]. Las estrellas centrales de nebulosas planetarias (CSPN) con líneas de emisión se pueden clasificar en dos grupos. Las estrellas CSPN [WR] presentan atmosferas deficientes en H. Sus capas exteriores están compuestas básicamente de He, C y O [Werner & Herwig, 2006][73]. Su nombre es debido a la similitud con las estrellas masivas Wolf-Rayet (donde el corchete las distingue de sus contrapartidas masivas). La existencia de estas estrellas plantea un problema a la teoría de evolución estelar que da lugar a la formación de las estrellas centrales de una NP. En los modelos evolutivos descritos con anterioridad, la CSPN mantiene una capa externa rica en H [Vassiliadis & Wood, 1994][71], de manera que en el caso de estrellas deficientes en H se requiere de un último pulso térmico para eliminar dicha capa.

Tylenda et al. (1993) [69] analizaron el espectro de 77 CSPN con líneas de emisión. Clasificaron la mitad como estrellas [WR]; el resto mostraban líneas de emisión en las mismas longitudes de onda que las CSPN [WR] pero más débiles y estrechas. A este grupo les asignaron el nombre de “*wels*” (“weak emission-line stars”). El espectro de estas estrellas se caracteriza por la presencia del doblete de carbono C IV 5801, 5812 Å y la presencia de emisión a 4650 Å que resulta de la superposición de N III 4364 Å, 4641 Å, C III 4650

Å y C IV 4658 Å. Las estrellas “*wels*” son un grupo heterogéneo [Fogel et al., 2003] [15] que no encaja en los esquemas de clasificación establecidos [Acker & Neiner, 2003] [2], que incluye estrellas ricas y pobres en H con presencia de vientos más débiles que en las [WR]. El número de estrellas CSPN clasificadas como “*wels*” es extremadamente alto hacia el bulbo galactico [Górny et al., 2004][18]. Aparentemente, se originan a partir de poblaciones estelares diferentes a las que dan lugar a CSPN [WR].

Las propiedades del espectro que favorecen la clasificación de la estrella como “*wels*” (i.e. la presencia de CIII 5801, 5802 Å y las líneas de emisión a la longitud de onda de 4650 Å) se observan en sistemas binarios próximos (e.g., Corradi et al., 2011; Miszalski et al., 2011). En estos sistemas la estrella primaria (mayor temperatura) se detecta mediante las líneas de He II 4686, 5412 Å en absorción; la primaria a su vez irradia la estrella compañera produciendo las líneas de emisión de N III, C III y C IV. En consecuencia, [Miszalski, (2009)] [48], sugirió que algunas de las estrellas “*wels*” son sistemas binarios no identificados como tal.

El camino evolutivo propuesto para explicar la formación de estrellas CSPN sin hidrógeno en su envoltura es el escenario denominado “born again event” [Schönberner, 1979; Iben et al., 1983] [60, 30], donde la estrella sufre un último “flash” de He una vez ha abandonado la fase AGB lo cual provoca la ingestión o la expulsión de la envoltura externa de hidrógeno. Se han propuesto otras teorías para explicar la existencia de CSNP [WR], entre las cuales destacamos la interacción en un sistema binario [De Marco & Soker, 2002; De Marco, 2008] [10, 9]. [Hadjuk, Zijlstra & Gesicki (2010)] [22] detectaron el primer sistema binario en una NP [WR]. Se trata de una binaria próxima, con un periodo de 0,63 días.

1.2.1. Cocientes de Líneas de Emisión

La emisión nebular es el resultado del proceso de fotoionización de una nube de gas difuso (principalmente H) por parte de una estrella con temperaturas superiores a los 25000 K, la estrellas a estas temperaturas emiten gran cantidad de fotones UV ionizantes con energías superiores a 13,6 eV dando origen a nebulosas con alto grado de ionización el cual viene determinado por el equilibrio entre las fotoionizaciones y las recombinaciones y depende fuertemente de la temperatura de la estrella ionizante. Los fotones emitidos en el proceso de recombinación se denominan radiación difusa y pueden escapar de la nebulosa sin ser re-absorbidos (Caso A) o pueden ser absorbidos por otro átomo/ion dando lugar, en caso de tener suficiente energía, a nuevas fotoionizaciones (Caso B).

Tabla 1.1: Algunas líneas nebulares sensitivas a la temperatura. (\AA). Tomado de Dopita, M. Sutherland, R. 2005 [11]

p^2	[N II]	[O III]	[S III]
$^1S_0 \rightarrow ^1D_2$	5755	4363	6312
$^1D_2 \rightarrow ^3P_2$	6583	5007	9532
$^1D_2 \rightarrow ^3P_1$	6548	4959	9069
p^4	[O I]	[Ne III]	[Ar III]
$^1S_0 \rightarrow ^1D_2$	5577	3343	5192
$^1D_2 \rightarrow ^3D_2$	6300	3869	7136
$^1D_2 \rightarrow ^3P_1$	6363	3968	7751

En esta investigación es de interés el Caso B que se se conoce también como absorción local y en él, los electrones capturados en el proceso de recombinación puede no ir directamente al nivel fundamental sino que entran a un estado excitado cayendo a continuación en cascada por los diferentes niveles mediante transiciones radiativas hasta el nivel fundamental. En particular para este estudio estamos interesados en líneas prohibidas de tipo colisional, como [O III] (alta excitación) y/o [N II] (baja excitación), que son producidas por desexcitaciones radiativas desde niveles poblados a causa de colisiones entre iones y electrones libres. Una vez producida la colisión, la radiación y la materia pueden interactuar ya sea, emitiendo electrones (Interacción ligado-libre), absorbiéndolos (interacción libre-ligado) o sin modificar el número de electrones libres (interacción ligado-ligado). En la tabla 1.1, se listan algunas de las más importantes líneas nebulares en los niveles p^2 y p^4 que dependen fuertemente de la temperatura de la estrella.

Para determinar la estructura de ionización se debe estudiar el equilibrio de fotoionización en cada punto de la nebulosa, el cual es establecido por el balance entre la ionización y la recombinación de los electrones con los iones. Dado que el H es el elemento más abundante, se puede establecer una aproximación idealizada sobre una estructura de una nebulosa constituida exclusivamente por H que rodea a la estrella caliente. Bajo esta hipótesis la ecuación de equilibrio de ionización es:

$$n(H^0) \int_{\nu_0}^{\infty} \frac{4\pi J_{\nu}}{h\nu} a_{\nu}(H^0) d\nu = n_e n_p \alpha(H^0, T) [cm^{-3} s^{-1}] \quad (1.1)$$

donde $n(H^0)$ es la densidad de átomos de H [cm^{-3}], ν_0 la frecuencia de ionización del H,

$4\pi J_\nu$ es la energía total impactando una región por unidad de área considerada y tiempo [$erg \cdot cm^{-2} \cdot s^{-1}$] y a_ν la sección eficaz de absorción de radiación en [cm^2], n_e y n_p la densidad de electrones libres y de protones respectivamente en [cm^{-3}] y $\alpha(H^0, T)$ el coeficiente de recombinación. En esta ecuación el miembro de la izquierda, específicamente la integral, representa la cantidad de fotoionizaciones y el término de la derecha ($\alpha(H^0, T)$) representa las recombinaciones producidas. En una nebulosa Caso B las ionizaciones producidas por el campo de radiación estelar están en equilibrio con las recombinaciones a niveles excitados, pero no al nivel fundamental pues en esa situación se vuelven a producir ionizaciones compensándose ambos procesos. Para el caso de elementos pesados tales como O, N, Ne, C (elementos con número atómico mayor que 2) la ec. de equilibrio toma la forma:

$$n(X^{+i}) \int_{\nu_i}^{\infty} \frac{4\pi J_\nu}{h\nu} a_\nu d\nu = n_e n(X^{+i+1}) \alpha(H^{+i}, T) \quad (1.2)$$

Tabla 1.2: Potenciales de ionización para elementos comunes en eV para diferentes estados de ionización

Elemento	Z	I	II	III
H	1	13.6	-	-
He	2	24.6	54.4	-
C	6	11.3	24.4	47.9
N	7	14.5	29.6	47.4
O	8	13.6	35.1	54.9

donde $n(X^{+i}), n(X^{+i+1})$ representa la densidad de los estados ionizados sucesivos y ν_i la frecuencia de ionización. En la tabla 1.2, se presentan los potenciales de ionización de algunos elementos “pesados”. Es importante aclarar que la ec. 1.2 se debe resolver para todos y cada uno de los gases que circundan la zona alrededor de la estrella, teniendo además en cuenta el número total de iones de todos los estados de ionización dado por la ecuación de cierre:

$$n(X^0) + n(X^{+1}) + n(X^{+2}) + \dots + n(X^{+N}) = n(X) \quad (1.3)$$

Por último, cabe mencionar que existen muchos factores que determinan la estructura de ionización de una nebulosa como los potenciales de ionización, la sección eficaz, coeficientes de absorción, temperatura, etc. [Osterbrock, D. E & Ferland, G. j. 2006.] [49]

1.2.2. Corrección de Enrojecimiento y Extinción

El polvo existente en la línea de visión entre el objeto observado y el telescopio enrojece el espectro debido a que se dispersan más los fotones en longitudes de onda cortas (azul) que en las largas (rojas). Es fundamental, corregir de ambos efectos para obtener medidas de la intensidad real emitida por el objeto.

Se define extinción para una longitud de onda determinada A_λ , como la diferencia entre la magnitud aparente observada y la magnitud esperada sin polvo:

$$A_\lambda = m_\lambda - m_\lambda^0 \quad (1.4)$$

El enrojecimiento sufrido por un objeto, es el resultado de comparar la extinción en diferentes longitudes de onda utilizando el llamado exceso de color, definido como:

$$E(B - V) = A_B - A_V \quad (1.5)$$

Definidos estos dos parametros se obtiene una relación entre ellos, mediante la ley de extinción:

$$X(\lambda) = \frac{A_\lambda}{E(B - V)} = R_V \frac{A_\lambda}{A_V} \quad (1.6)$$

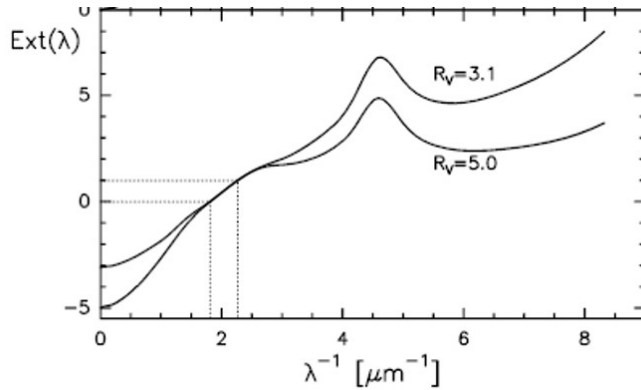


Figura 1.6: Curva de extinción estelar, de acuerdo con la ec. 1.6. Se ilustran dos casos, $R_V=3.1$ se refiere a un medio difuso y $R_V=5$ para el extremo de una nube molecular. Fuente Krügel (2003) [33]

con R_V , la curva estándar de enrojecimiento (fig.1.6), que toma el valor de 3.1 para el rango del visible. Se han realizado varios estudios que han arrojado diferentes leyes de extinción, Whitford (1958) óptico; Seaton (1979), para óptico y UV, Howarth (1983) en IR; Calzetti et al. (2000) en UV/óptico/NIR. En esta tesis se utilizará el modelo obtenido por [Cardelli et al. (1989)] [6]

$$X(\lambda) = a(\lambda)R_V + b(\lambda) \quad (1.7)$$

donde los términos $a(\lambda)$ y $b(\lambda)$ son polinomios, en unidades μm^{-1} , cuya forma depende del rango del espectro en que se trabaje. En particular, en el rango óptico ($1,1 < \lambda < 3,3$) y para $y = (1/\lambda) - 1,82$, se definen como:

$$\begin{aligned} a(\lambda) &= 1 + 0,17699y - 0,5044y^2 + 0,02427y^3 + 0,72085y^4 \\ &\quad + 0,01979y^5 - 0,77530y^6 + 0,32999y^7 \\ b(\lambda) &= 1,41338y + 2,28305y^2 + 1,07233y^3 - 5,38434y^4 \\ &\quad - 0,62251y^5 + 5,30260y^6 - 2,09002y^7 \end{aligned} \quad (1.8)$$

El flujo medido por el observador, $F(\lambda)$, es la intensidad emitida por el objeto, $I(\lambda)$, atenuada debido a la extinción:

$$F(\lambda) = I(\lambda)10^{-0,4A_\lambda} \quad (1.9)$$

dado que tal extinción no depende del objeto, sino solamente de la cantidad de polvo y de la ley de extinción utilizada, se puede escribir de la forma:

$$A_\lambda = 2,5[f(\lambda) + 1]c(H\beta) \quad (1.10)$$

donde $c(H\beta)$ es el coeficiente de enrojecimiento que informa la cantidad de polvo y $f(\lambda)$ es la función de enrojecimiento y que se define como:

$$f(\lambda) = \frac{A_\lambda}{A_{H\beta}} - 1 = \frac{X(\lambda)}{X(H\beta)} - 1 \quad \text{normalizada a } f(H\beta)=0 \quad (1.11)$$

De tal forma que el flujo observado se puede escribir de la forma:

$$F(\lambda) = I(\lambda)10^{-[f(\lambda)+1]c(H\beta)} \quad (1.12)$$

En la práctica, para estimar la extinción y el enrojecimiento y hacer la respectiva corrección se recurre al decremento de las líneas de recombinación del Hidrógeno en la serie de Balmer (con $i=\alpha, \beta, \gamma, \delta$, etc) relativas a $H\beta$:

$$\frac{F(Hi)}{F(H\beta)} = \frac{I(Hi)}{I(H\beta)} 10^{-c(H\beta)[f(Hi)-f(H\beta)]} \quad (1.13)$$

como $f(H\beta) = 0$, la ecuación 1.13, se puede reescribir de la forma:

$$\log \frac{F(Hi)/F(H\beta)}{I(Hi)/I(H\beta)} = -c(H\beta)f(Hi) \quad (1.14)$$

esta última ecuación 1.14, representa una línea recta, cuya pendiente es $c(H\beta)$, de tal forma que por un ajuste de mínimos cuadrados se puede calcular la pendiente y así obtener el valor experimental del coeficiente de enrojecimiento. El resto de parámetros del ajuste se obtiene experimentalmente: $F(Hi)/F(H\beta)$ es el flujo medido para cada línea de recombinación, $f(\lambda)$ es la función de enrojecimiento (ecuaciones 1.7 y 1.11), $I(Hi)/I(H\beta)$ son los cocientes teóricos, que son prácticamente constantes para el Hidrógeno [Osterbrock & Ferland. 2006] [49], situación característica de las nebulosas que evolucionan mediante el Caso B.

Una vez estimado el coeficiente de enrojecimiento, se pueden corregir los cocientes relativos de todas las líneas medidas para obtener la intensidad real emitida por el objeto

$$\frac{I(\lambda)}{I(H\beta)} = \frac{F(\lambda)}{F(H\beta)} 10^{c(H\beta)f(\lambda)} \quad (1.15)$$

y también calcular el valor de la extinción y el exceso de color [Fernández. (2013)] [13]

1.3. Microestructuras

Las microestructuras son pequeñas estructuras que se encuentran en las nubes que rodean los bordes de los aros de la nebulosa planetaria y son el resultado de inestabilidades. Estas fueron detectadas por primera vez como resultado de la extinción o porque su estado de ionización es mucho más bajo que el del resto de la nebulosa planetaria.

1.3.1. Fliers, Brets, Lis, Knots, Ansaes

Al estudiar las nebulosas planetarias con una alta resolución espacial se puede observar que, en muchos casos, se presentan estructuras altamente articuladas, un subgrupo de las cuales son los pares de baja ionización y/o alta velocidad dispuestos en forma simétrica respecto del núcleo, como es el caso de los chorros y asas, conocidos por su sigla en inglés FLIERs (“Fast Low Ionization Emission Regions”). Un tratamiento clásico de estas estructuras es el de [Balick et al. (1994)] [3].

Si bien el número de nebulosas con morfología bien determinada no es elevado debido fundamentalmente a que la mayoría de ellas presentan un pequeño tamaño angular, se han estimado los porcentajes sobre una muestra de 250 nebulosas de cada tipo morfológico: Round (R) 23 %, Elíptica (E) 49 %, Bipolar (B) 14 %, Cuadrupolar (Q) 3 % y de Simetría puntual (PS) 4 % [Manchado et al., 1996] [43] Observaciones espectroscópicas han mostrado que estas estructuras son formadas por gas en un estado de baja ionización,

principalmente en líneas de [N II] y [O I]. El origen y los mecanismos de aceleración de los FLIERs aún no son totalmente comprendidos.

LIS es un término acuñado por Gonçalves, que es el acrónimo de Low Ionization Structures, es muy común que aparezcan principalmente o exclusivamente líneas de emisión de baja ionización y se encuentran en la mitad de las nebulosas planetarias [Gonçalves et al., (2001)] [17].

Otros investigadores han denominado un tipo de estructuras como BRETS (Bipolar Rotating Emission Line Jets) [López, 1997; Guerrero, 2000] [40, 20], que son pares de knots con simetría puntual y con estructura en forma de S. Estos han sido detectados en una gran cantidad de nebulosas planetarias (López et al. (1993)) [39], pero presentan grandes problemas en la teorización de la evolución estelar.

Los knots son llamados en ocasiones como ansae y son más comunes en las nebulosas elípticas. La naturaleza de los nudos brillantes, presentes a lo largo del eje de muchas nebulosas planetarias y protoplanetarias elípticas y bipolares, aún es un misterio. [Meaburn et al. (1998)] [45] encontró que los knots se van moviendo radialmente, pero más lentamente que los vientos en los cuales están inmersos.

Mientras estas características pueden ser efectos intrínsecos de segundo orden atribuibles a variaciones estadísticas en las condiciones iniciales de nebulosas planetarias particulares, el hecho de que muchas estén orientadas a lo largo del eje mayor de los flujos eyectados significa que pueden ser interpretados como remanentes de una temprana fase de colimación de esos flujos.

Motivación de la Tesis

Las nebulosas planetarias son fascinantes, encantadoras y difieren bastante incluso unas de otras, su naturaleza etérea, su corto período de vida y su gran variedad de formas hace de ellas todo un reto de estudio.

El 95 % de las estrellas del universo son candidatas a evolucionar al estado de nebulosa planetaria, por tal motivo se hace fundamental el estudio de esta fase, ya que al estudiarla se revela el futuro del sistema solar. Son una fuente relativamente fácil de estudio, ya que se encuentran presentes en todo lugar del Universo y se caracterizan por presentar un espectro único con líneas muy brillantes debido a los procesos de excitación colisional que ocurren dentro de ellas.

Las nebulosas planetarias son fundamentales para el entendimiento de la evolución química de las galaxias. Entender esta fase en la evolución estelar ayuda a comprender como una galaxia evoluciona, a través de vida y la muerte de las estrellas que la constituyen. Durante sus vidas, las estrellas presentan reacciones nucleares (fusión) en su interior, sintetizando así los elementos químicos que se conocen hoy día. Durante estos procesos de fusión los elementos pesados producidos en el interior de la estrella salen a la superficie estelar para ser posteriormente eyectados y así finalmente contribuir al enriquecimiento químico de la galaxia y la formación de estrellas e incluso planetas de una nueva generación. Un profundo conocimiento de la formación y evolución de estos objetos, mejorará notablemente los modelos de evolución estelar, las teorías de interacción de vientos, así como también, los modelos de evolución química de las galaxias.

Dado que las estrellas de baja masa son consideradas como las factorías de materia en el Universo, entender su secuencia evolutiva desde la fase AGB a la fase de nebulosas planetarias es imperativo, así como también, comprender los mecanismos de eyección de masa, por ello, se hace necesario analizar y determinar las propiedades morfológicas y físicas de los choques irradiados, estudiando el calentamiento debido a los fotones estelares de las

regiones chocadas. Algo muy común en las Nebulosas Planetarias es la presencia de flujos bipolares y morfologías con simetría puntual, pero en tales estructuras aún quedan aspectos por descifrar. Explicar cuales son los agentes que modelan las nebulosas planetarias es uno de los grandes retos actuales de la teoría de la evolución estelar.

En el estudio de las nebulosas planetarias diversas morfologías han sido observadas y por consiguiente diferentes modelos teóricos han sido formulados, entre ellos: La interacción de vientos estelares (Mellema, 1993); Sistemas binarios como estrella central (Bond & Livio, 1990; Morris, 1987); Pulsos no radiales (Soker & Harpar, 1992) y la influencia de campos magnéticos (Pascoli, 1992; Soker & Harapar 1992; García-Segura et al. 1992). Para explicar la diversa morfología, se hace necesario establecer cual de los mecanismos anteriores es el dominante en los procesos de eyección de masa y por consiguiente en la morfología de la nebulosa planetaria [García, J; 2006] [16].

2.1. Objetivos de la tesis

El objetivo fundamental de esta tesis es caracterizar la morfología, la estructura de ionización de “choques irradiados”(o FLIERs) observados en un grupo amplio de nebulosas planetarias. Con estos resultados se podrán mejorar las simulaciones numéricas ya que permitirán acotar los valores de los parámetros iniciales del código hidrodinámico.

Este objetivo se puede desglosar en los siguientes puntos:

- Obtener los tamaños característicos de los FLIERs y de los cocientes de líneas de emisión a partir de las imágenes obtenidas con el Hubble Space Telescope (HST). Estos datos se obtendrán del archivo del HST (acceso libre). La limitación del uso de estas imágenes es que, en la mayoría de los casos, únicamente podemos disponer de imágenes en algunos pocos filtros ($H\alpha$ 6563Å, $[O III]$ 5007Å y $[N II]$ 6584Å).
- Estudiar las condiciones físicas del espectro en líneas de emisión, de la estructura de ionización para algunas de las nebulosas planetarias del grupo seleccionado.
- Determinar las propiedades físicas y observacionales presentes en los FLIERs (LIS).
- Establecer clases de estructuras (jets, bow shocks, knots, lobes) con base a los tamaños del análisis wavelet.

2.2. Estructura de la tesis

El objetivo de este trabajo radica en obtener la estructura de ionización de las nebulosas estudiadas, determinando la estratificación de los choques irradiados y obtener la morfología y tamaño de las microestructuras presentes.

La primera parte de la tesis está dedicada a explicar y presentar los fundamentos teóricos desarrollados hasta el momento en el estudio de la formación y evolución de las nebulosas planetarias, así como también una clasificación de estructuras y mecanismos de formación de dichas estructuras.

En el capítulo 3, se describen los aspectos técnicos de la instrumentación utilizada en las observaciones. Se describirá la WFPC2 ubicada en el HST, así como también los procesos de análisis wavelet anisotrópico, calibración en flujo, extinción y desenrojecimiento.

En el capítulo 4, se presenta el análisis, la simulación y los resultados obtenidos para la nebulosa proto-planetaria CRL 618. Estos resultados han sido ya publicados en la revista *Astronomy & Astrophysics*.

En el capítulo 5, se presentan los resultados correspondientes a las nebulosas planetarias (9 en total) que se tomaron con la WFPC2 y se han procesado en STSCi siguiendo el tratamiento estándar. El análisis se realizó utilizando las líneas de [O III], [N II] y $H\alpha$. Se utilizan estas imágenes debido a su alta resolución espacial y por su disponibilidad en la base de datos MAST. Estos resultados serán enviados próximamente a *Astronomy & Astrophysics* para su publicación.

Finalmente, se presentan las conclusiones generales de esta tesis, junto con los posibles trabajos futuros.

Observaciones y Metodología de Análisis

Para esta tesis, se trabajó con la base de datos del Hubble Space Telescope (HST). En este capítulo, se presentarán las características de la instrumentación empleada, así como también se describirán las técnicas de observación. Adicionalmente se describirán las características principales de cada uno de los objetos seleccionados (9 nebulosas planetarias y 1 nebulosa protoplanetaria) para su análisis.

3.1. Imágenes WFPC2-HST

3.1.1. Descripción del instrumento

El Objetivo científico de la WFPC2 (Wide Field and Planetary Camera 2) es proveer imágenes fotométricas precisas de objetos astronómicos sobre un amplio campo de visión, con una alta resolución angular y un amplio rango de longitudes de onda.

La cámara WFPC2 se instaló a bordo del HST, en Diciembre de 1993. Es un instrumento que permite la obtención de imágenes bidimensionales, ubicado en el centro del plano focal del telescopio espacial, lo que garantiza una alta calidad en las imágenes ya que incluye correcciones de la aberración esférica que sufre la óptica del telescopio (OTA). Cubre el rango espectral entre 1150Å y 10500Å.

Tabla 3.1: Características de las cámaras CCD de WFPC2

Cámara	Nº de Píxeles	CCD	FOV	Escala por píxel	Cociente (f/radio)
Wide Field	800x800	3	80"x80"	~ 100 marcsec	12.9
Planetary	800x800	1	35"x35"	~ 46 marcsec	28.3

El campo de visión de la WFPC2 está dividido en cuatro subcampos contiguos mediante un espejo piramidal de cuatro caras situado en el foco del HST. Se obtiene una imagen para cada uno de estos cuatro campos, mediante la utilización de cuatro cámaras y sensores CCD. Cada uno de los cuatro detectores CCDs contiene 800×800 píxeles. Tres cámaras operan con un muestreo espacial de $0.1''$ por píxel ($f/12.9$) definiendo un campo de visión proyectada en el plano del cielo en forma de “L”; la cuarta cámara, cámara planetaria, opera con un muestreo espacial de $0.046''$ por píxel ($f/28.3$). Cada imagen obtenida será un mosaico de cuatro imágenes con cocientes focales de $f/12.9$ y $f/28.3$. En la figura 3.1 se ilustra el campo de visión WFPC2 proyectado sobre el cielo. Los ejes U_2 , U_3 (o $-V_2$, $-V_3$) están definidos por el eje que traza la “Optical Telescope Assembly” (OTA) la posición angular de $-V_3$ varía de acuerdo con la dirección de apuntado y época de observación [McMaster, M., et al., 2008][44].

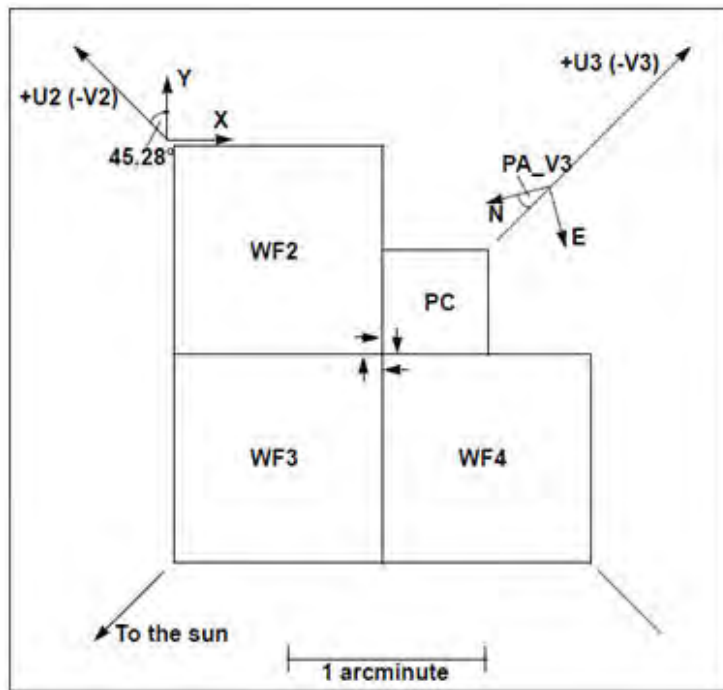


Figura 3.1: Campo de visión WFPC2 proyectado en el plano del cielo. Fuente: Wide Field and Planetary Camera 2. Instrument Hadbook [44]

El sistema WFPC2+HST presenta una eficiencia cuántica que oscila entre el 14 % para el rojo y permanece sobre el 4 % para el espectro visible. El proceso de respuesta global se muestra en la figura 3.2. La curva indica la probabilidad de que un fotón que entre por la apertura de 2.4 m del HST cerca del centro de alguno de los detectores, sea reflejado por los espejos y eventualmente sea detectado como un electrón en la CCD.

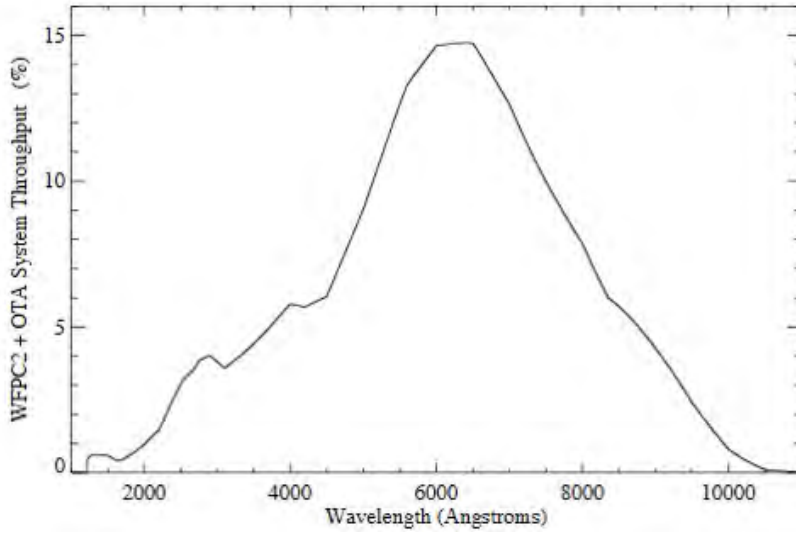


Figura 3.2: Rendimiento del sistema WFPC2+OTA (Optical Telescope Assembly). Fuente: Wide Field and Planetary Camera 2. Instrument Handbook. [McMaster, et al. 2008], [44]

La cámara cuenta con 48 filtros espectrales, incluyendo filtros de banda estrecha. Los filtros de banda estrecha permiten la obtención de imágenes en las líneas de emisión que caracterizan el espectro de una nebulosa planetaria: [O III] (4363Å) (F437N), [OIII] (5007Å) (F502N), He II (4686Å) (F469N), $H\alpha$ (6563Å) (F656N), [NII] (6583Å) (F658N), [SII] (6716Å, 6730Å) (F673N), [OI] (6300Å) (F631N), [O II] (3732Å) (F375N) entre otros [44]. Hacemos notar que el filtro F656N (generalmente atribuido a $H\alpha$) incluye una contribución de la emisión de las líneas [N II] 6548, 6583 Å, con una transmisión del 25 % respecto a $H\alpha$. Lo que indica que el 25 por ciento del conteo total de fotones en las imágenes de F656N en WF/PC2 proviene del doblete [N II] (ver fig. 3.3) [Szyszka, et al. 2011] [66].

3.1.2. Calibración en flujo

La calibración fotométrica se hace necesaria y se deriva de la observación de las estrellas estándar y de los perfiles de los filtros utilizados. Posteriormente, se establece el tipo de unidades en las cuales fue adquirida la imagen, que puede ser en unidades de cuentas (C) o en número de datos (DN) por unidad de tiempo y pixel. Esta Calibración permite convertir la imagen observada en cuentas por segundo a flujo ($\text{erg s}^{-1} \text{cm}^{-2}$) multiplicando la imagen normalizada por el factor PHOTFLAM y por el ancho del filtro (en Å) sobre el tiempo de exposición (ver tabla 3.2.)

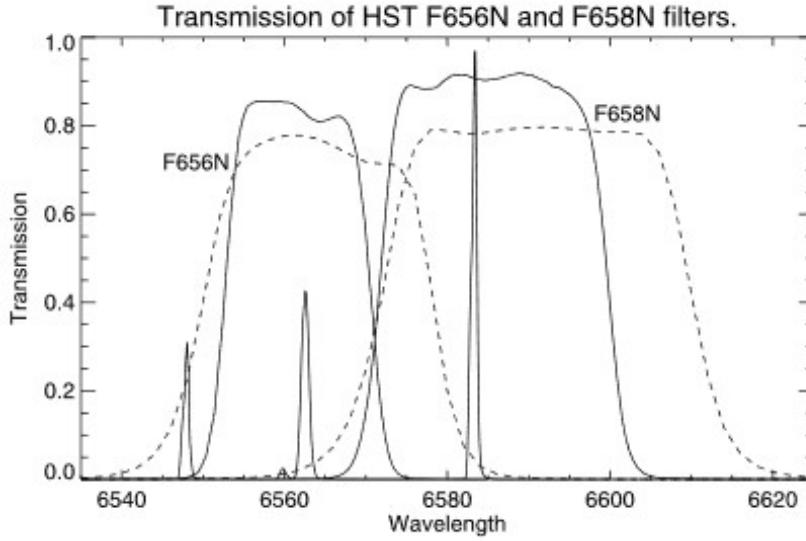


Figura 3.3: Curvas de transmisión para los filtros $H\alpha$ y $[N II]$. La línea punteada representa la WF/PC2 y la línea sólida la WFC3 respectivamente. Fuente: [Szyszka, et al. 2011] [66]

Se procede entonces a la calibración en flujo, es decir, transformar el tipo de unidades originales, que pueden ser “counts” o “counts/s”, a unidades de flujo. Según el tipo de unidades base, se trabaja con:

$$F(\lambda) = \frac{DN}{C} * \frac{PHOTFLAM * rectw}{exptime} \quad (3.1)$$

o

$$F(\lambda) = \frac{DN}{C} * PHOTFLAM * rectw \quad (3.2)$$

respectivamente.

Finalmente, se procede a calcular los parámetros fotométricos cuyos valores se actualizan en la cabecera de la imagen de la fuente observada. El parámetro “PHOTFLAM” (parámetro de sensibilidad inversa) que se define como el flujo de una fuente con flujo constante por unidad de longitud de onda (en $\text{erg s}^{-1} \text{cm}^{-2} \text{\AA}^{-1}$) que produce una cuenta por segundo (DN/s). El parámetro, “rectw” se obtiene del ancho del filtro utilizado y es proporcionado en el proceso de reducción y también depende de la época en que se realice la captura de la imagen. Por último, el “exptime”, es el tiempo de exposición de la imagen, con lo cual $F(\lambda)$ se expresa en $[\text{erg s}^{-1} \text{cm}^{-1} \text{\AA}^{-1}]$.

Tabla 3.2: Parámetros fotométricos Photflam, rectw, exptime y $\Delta\lambda$ de calibración para los filtros F656N, F658N, F502N

Nebulosa	Filtro	Photflam [$\text{erg cm}^{-2} \text{ \AA}^{-1} \text{ s}^{-1}$]	rectw	exptime [s]	$\Delta\lambda [\text{\AA}]$
IC 4634	$H\alpha$	1.461279×10^{-16}	28.349	500.0	21.5
	[N II]	1.035578×10^{-16}	29.331	500.0	28.5
	[O III]	3.004926×10^{-16}	35.82	500.0	26.9
IC 4593	$H\alpha$	$2.07546604717655 \times 10^{-17}$	28.349	1600.0	21.5
	[N II]	$1.470774839170836 \times 10^{-17}$	29.331	1600.0	28.5
	[O III]	$4.267917798427448 \times 10^{-17}$	35.82	1600.0	26.9
NGC 3918	$H\alpha$	$2.05238904494382 \times 10^{-17}$	28.349	140.0	21.5
	[N II]	$1.45442134831460 \times 10^{-17}$	29.331	1200.0	28.5
	[O III]	$4.220463483146067 \times 10^{-17}$	35.82	320.0	26.9
NGC 6210	$H\alpha$	1.461301×10^{-16}	28.349	40.0	21.5
	[N II]	1.035548×10^{-16}	29.331	400.0	28.5
	[O III]	3.00497×10^{-16}	35.82	100.0	26.9
NGC 6543	$H\alpha$	1.583134×10^{-16}	28.349	800.0	21.5
	[N II]	9.837374×10^{-17}	29.331	1000.0	28.5
	[O III]	3.451899×10^{-16}	35.82	400.0	26.9
NGC 7009	$H\alpha$	3.034700×10^{-16}	28.349	100.0	21.5
	[N II]	2.120023×10^{-16}	29.331	400.0	28.5
	[O III]	6.005390×10^{-16}	35.82	40.0	26.9
NGC 7354	[N II]	$1.470774839170836 \times 10^{-17}$	29.331	1000.0	28.5
	[O III]	$4.267917798427448 \times 10^{-17}$	35.82	620.0	26.9
PN Hb 4	$H\alpha$	$2.05238904494382 \times 10^{-17}$	29.331	600.0	28.5
	[N II]	$1.454421348314607 \times 10^{-17}$	35.82	600.0	26.9
M 3-1	$H\alpha$	$2.05238904494382 \times 10^{-17}$	29.331	600.0	28.5
	[N II]	$1.454421348314607 \times 10^{-17}$	35.82	600.0	26.9

3.1.3. Tratamiento de las imágenes

Las imágenes observadas se han calibrado utilizando el algoritmo estándar de calibración para la cámara WFPC2 (calwp2) [McMaster, M., et al., 2008] [44]. Este algoritmo incluye los pasos utilizados, en la reducción/tratamiento estándar para imágenes obtenidas con

un detector CCD, incluyendo la sustracción de la corriente de polarización (o “bias”), la sustracción de la corriente oscura (o “dark current”) y la corrección de las variaciones espaciales en la respuesta del detector (mediante la obtención de un “flat field”). El proceso de reducción incluye la corrección por distorsión geométrica (i.e., el tamaño del pixel varia a lo largo del campo de visión).

3.1.4. Selección de la muestra

El criterio de selección de la muestra de nebulosas planetarias se realiza en base a las siguientes condiciones: i) presencia de microestructuras o FLIERs (Fast Low Ionization Emission Region) (ver sección 1.3), ii) existencia de imágenes en el archivo del HST (Multi Archive Space Telescope) y iii) disponibilidad de imágenes WFPC2 en los filtros de $H\alpha$ 6563Å, [NII] 6583Å y [OIII] 5007Å, obtenidas simultáneamente. En la tabla 3.3 se listan las nebulosas planetarias seleccionadas para esta tesis.

Tabla 3.3: Muestra de las Nebulosas Planetarias obtenidas del archivo del HST (MAST) y nebulosa protoplanetaria

Objeto	Morfología	Microestructura	Filtro
IC 4634	Puntual	Jets, Knots	$H\alpha$, [N II], [O III]
IC 4593	Elíptica	Knots	$H\alpha$, [N II], [O III]
NGC 3918	Elíptica	Jets, filamentos	$H\alpha$, [N II], [O III]
NGC 6210	Puntual	Jets, knots	$H\alpha$, [N II], [O III]
NGC 6543	Elíptica	Jets	$H\alpha$, [N II], [O III]
NGC 7009	Elíptica	Jets, Knots	$H\alpha$, [N II], [O III], He II, [O I], [S II]
NGC 7354	Elíptica	Jets, jet-like	[N II], [O III]
PN Hb4	Elíptica	Knots	$H\alpha$, [N II]
M 3-1	Puntual	knots, jet-like	$H\alpha$, [N II]
CRL 618	Multipolar	jets	[S II]

Dado que las imágenes que se obtienen a partir de detectores CCD poseen contribuciones no deseadas que contaminan la mediciones se han procesado en el “Space Telescope Science Institute” (STScI) siguiendo el tratamiento estándar “pipeline”. Este tratamiento estándar consiste en eliminar los defectos mediante la aplicación de correcciones con imágenes de

calibración “bias” y “flat field”.

La corrección por “bias” consiste en eliminar un valor umbral (ruido) que se obtiene de una serie de imágenes con tiempo de exposición nulo y que se genera por la captura de información generada al leer el chip de la CCD (intrínseco al dispositivo). Una vez calculado el valor promedio se sustrae su valor de la imagen observada; mientras que para el caso del “flat field” se obtiene un valor promedio de las variaciones espaciales en la respuesta de sensibilidad del detector ante la captura de imágenes de objetos con iluminación uniforme (i.e. pantalla blanca mate) con el filtro deseado, una vez establecido tal valor se divide la imagen observada entre el valor flat field.

Una vez hechas las correcciones estándar de las imágenes se procede a recentrar las imágenes de cada nebulosa obtenidas con los diferentes filtros. Para ello se utilizaron las rutinas GEOMAP Y GEOTRAN, (del paquete de reducción IRAF) que permiten desplazar y guiar las imágenes.

3.1.5. Análisis Wavelet: determinación de los tamaños característicos de los FLIERs

Antes de determinar los tamaños característicos, las imágenes son rotadas, para que el eje vertical coincida con uno de los ejes bipolares o de simetría de la nebulosa. El estudio de la morfología y tamaño de las estructuras (lóbulos, knots o filamentos) se realiza mediante el análisis de transformadas wavelet anisotrópicas. Se ha elegido este tipo de análisis porque permite caracterizar las estructuras espaciales sin perder la información sobre la posición que ocupa dicha estructura. Se ha introducido el análisis anisotrópico porque las estructuras pueden presentar diferentes tamaños característicos en la dirección bipolar y en su perpendicular. La transformada wavelet es esencialmente una convolución, donde una función de entrada (en este caso, la región de interés de la imagen) se convoluciona con una función wavelet, que es una función cuya propiedad básica es que su integral sobre todo el espacio es nula. La transformación “wavelet” descompone la imagen en una serie de mapas con diferentes escalas.

En este caso, se ha utilizado como wavelet, la función “mexican hat”, de la forma:

$$g(r) = C(2 - r^2)e^{-r^2/2} \quad (3.3)$$

donde $r = [(x/a_x)^2 + (y/a_y)^2]^{1/2}$, siendo a_x y a_y la longitud de escala del wavelet en la dirección x- e y-, respectivamente (donde y coincide con la dirección bipolar, x es la

dirección perpendicular y C es una constante de normalización). Se elige un rango de valores para (a_x, a_y) y se calculan las convoluciones, mediante un algoritmo FFT (Fast Fourier Transform) estándar,

$$T_{a_x, a_y}(x, y) = \int \int I(x', y') g(r') dx' dy' \quad (3.4)$$

con $r' = ([(x' - x)/a_x]^2 + [(y' - y)/a_y]^2)^{1/2}$, e $I(x, y)$ es la emisión observada como función de la posición del pixel (x, y) . Con este proceso se produce un mapa transformado $T_{a_x, a_y}(x, y)$, correspondiente al mapa observado $I(x, y)$. Estas transformaciones son representaciones de la imagen que muestran las estructuras que tienen escalas similares a los valores seleccionados para la escala wavelet.

Los mapas obtenidos se usan para caracterizar el tamaño de las microestructuras y el intervalo de valores elegidos para a_x, a_y oscilan entre 1 y 60 pixeles. A partir de las imágenes observadas, se fija una posición en el eje y (eje bipolar) y se determinan los valores x_k con $k=1, 2, 3$, donde el mapa de intensidad presenta un máximo local. Para cada par de puntos (x_k, y) $I(x_k, y)$ presenta un máximo local y se determina un par (a_{x_k}, a_{y_k}) en el espacio a_x, a_y donde la transformada wavelet presenta un máximo local. De esta manera se pueden determinar los tamaños característicos de una estructura que presente un máximo de intensidad en la posición (x_k, y) [Riera et al., (2003)] [54]

3.1.6. Perfiles Unidimensionales

Para cada nebulosa planetaria se han obtenido los perfiles unidimensionales característicos de las líneas de emisión $[OIII]/H\alpha$ y $[NII]/H\alpha$, los cuales son unos excelentes indicadores de los desplazamientos de las zonas de FLIERs. A partir del cociente se extrae un perfil a lo largo de una sección de la nebulosa buscando que la sección pase a través de las zonas de interés (sean knots, lobes, etc) y a su vez pase por el centro de la nebulosa con el fin de determinar la distancia y sus posibles desplazamientos respecto a un punto común de la estructura de la nebulosa, considerando que la nebulosa sea de simetría puntual.

Es importante mencionar que la sección resulta de la agrupación de los pixeles que cubren en su totalidad las zonas de FLIERs.

Análisis y simulación de la Nebulosa Protoplanetaria CRL 618

New light on the multiple jets of CRL 618

A. Riera, P. F. Velázquez, A. C. Raga, R. Estalella, and A. Castrillón.

A&A 561, A145 (2014)

4.1. Resumen de la publicación

Las nebulosas proto-planetarias (pPNe) representan una fase transitoria en las últimas etapas de las estrellas de masa baja e intermedia. El (Los) proceso(s) que lleva la pPNe de la rama gigante asintótica esférica (AGB) a esta fase transitoria, donde eyecta gran cantidad de materia con una geometría bipolar/multipolar, no se conoce en detalle. Se sospecha que las interacciones entre estrellas en un sistema binario causan la salida de la simetría esférica.

Una vez la estrella entra en esta fase será rodeada por el material expulsado, formando una envoltura circumestelar (CSE) de gas y polvo en expansión. En esta etapa, se ha formado una estrella post-AGB o como se la conoce normalmente una nebulosa proto-planetaria (pPN)).

El objetivo de esta publicación es determinar si la existencia de una fuente binaria que expulsa un viento (desde la estrella primaria) y con una eyección de jets con geometría bipolar desde la compañera binaria, podría producir la morfología y la cinemática de los conocidos pPN multipolar CRL 618.

Aplicamos un análisis wavelet anisotrópico a las imágenes del Telescopio Espacial Hubble

(HST) [S II] de CRL 618 para determinar los tamaños característicos de varias estructuras a pequeña escala a lo largo y ancho de los chorros ópticos de CRL 618. De las imágenes de archivo [S II] HST de CRL 618 con una base de tiempo de 10,7 años, llevamos a cabo mediciones de movimiento propio de las estructuras de emisión observadas en los lóbulos de CRL 618. Se calculan seis simulaciones numéricas 3D de un chorro de velocidad de eyección en precesión dependiente del tiempo lanzado desde un estrella compañera hipotética de un sistema binario [Riera, et al., (2014)] [55]

4.2. Introduction

CRL 618 was identified as an object in transition from the asymptotic giant branch (AGB) to a planetary nebula (PN), that is in the proto-planetary nebula (pPN) phase, based on its optical, infrared and radio properties (Westerbrook et al. 1975). Groundbased optical and near-infrared imaging of CRL 618 revealed two lobes of emission separated by a dark lane. Hubble Space Telescope (HST) narrowband images revealed highly collimated outflows (or jets) showing a multipolar geometry (Trammell & Goodrich 2002). These jets are known to have high velocities in the optical lines (Carsenty & Solf 1982; and Sánchez Contreras et al. 2002). High velocities and multipolar jets are also seen in molecular gas. High-velocity features associated with the optical jets, with velocities up to 200 km s^{-1} , were detected in H_2 (Cox et al. 2003). Dense molecular gas detected in CO is also outflowing at velocities on the order of 200 km s^{-1} (Cernicharo et al. 1989; Sánchez Contreras et al. 2004; Bujarrabal et al. 2010; Soria-Ruiz et al. 2013). Recent interferometric maps of the CO $J = 1-2$ emission showed different molecular components in CRL 618: 1) a compact bipolar outflow (at a velocity higher than 200 km s^{-1}); 2) large expanding torus ($\sim 11''$) perpendicular to the outflow; 3) a compact dense torus-like core perpendicular to the outflow; and 4) an extended round halo (Sánchez Contreras et al. 2004; Sánchez Contreras & Sahai 2004; Lee et al. 2013).

Surrounding the central star, there is a compact H II region elongated in the east-west direction, detected in the centimeter and millimeter-wave continuum (Kwok & Feldman 1981; Kwok & Bignell 1984; Martín-Pintado et al. 1988). This elliptical H II region has increased in flux and size over a period of ~ 26 years (Tafoya et al. 2013).

Recently, proper-motion measurements of the outermost features of the jets of CRL 618 have been obtained from $\text{H}\alpha$ HST images with a time base of 11 years (Balick et al. 2013).

Balick et al. reported tangential velocities of $\sim 300 \text{ km s}^{-1}$.

From early ground-based observations, the optical emission from the lobes has been known to be shock-excited (Trammell et al. 1993; Sánchez Contreras et al. 2002; Riera et al. 2006). More recently, Riera et al. (2011) have analyzed the HST STIS spectra of several features of the jets of CRL 618 with unprecedented spatial resolution. Unfortunately, the slit was displaced from the leading bow-shocks. Comparing the observations with plane-parallel shock models, Riera et al. (2011) found that the shock velocities lie in a narrow range between 30 and 40 km s^{-1} , except for the $[\text{O III}]/\text{H}\beta$ line ratios which require higher shock velocities (80–90 km s^{-1}). The predicted shock velocities are significantly lower than the velocities with which the jets move outward.

Table 4.1: HST [S II] images of CRL 618.

Proposal ID	Camera	Filter	Filter center/ width (nm)	Pixel size (")	Exposure time (s)	Data sets	Observation date
6761	WFPC2	F673N	673.2/4.7	0.045	1200	u36a0107/8	1998-10-23
11580	WFPC3/UVIS	F673N	672.5/11.8	0.040	1200	ib1m02060/1/2/3/4	2009-08-08

Several models have been invoked to explain the bipolar/multipolar morphology of some pPNe. Most are based on the presence of a bipolar jet or collimated fast wind (CFW) ejected by one of the stars in a binary system (e.g., Morris 1987; Soker & Rappaport 2000). Hydrodynamical simulations with a time dependent ejection velocity and/or precessing jets have successfully reproduced the morphology of bipolar pPNe and PNe, such as the point-symmetric nebulae: Hen 3-1475 (Velázquez et al. 2004), PN K 3-35 (Velázquez et al. 2007), IC 4634 (Guerrero et al. 2008), and the Red Rectangle (Velázquez et al. 2011). In particular, there are some numerical simulations that try to reproduce the morphology and kinematics of CRL 618, such as the study of Lee & Sahai (2003), who proposed that the CFW interacts with a spherical AGB wind (see also, Lee et al. 2009); alternatively, Dennis et al. (2008) proposed that the multiple jet appearance of CRL 618 could be due to clumps moving outwards at high velocities and slightly different directions. Balick et al. (2013) have explored the nature of the jets of CRL 618 by means of 3D hydrodynamical simulations of either a bullet or a continuous jet moving through the remnant AGB wind. These authors favored the “bullet” hypothesis based on the multipolar morphology. Some studies have been carried out to explain how both mirror-and point-symmetric morphologies can be obtained from a precessing jet from a binary system (see, e.g., Raga

et al. 2009). Haro-Corzo et al. (2009) analyzed the influence of the orbital motion on the optical emission of these objects, by means of 3D hydrodynamical simulations. Their predicted [N II] emission line maps can produce different luminosities for the two lobes, as observed in CRL 618 (Sánchez Contreras et al. 2002; Riera et al. 2011).

More recently, Velázquez et al. (2012, 2013) have shown that the existence of a binary source that ejects a wind (from the primary star) and a bipolar, precessing jet with time-dependent ejection velocity (from the orbiting companion) can reproduce the multipolar geometry of pPNe. These authors have shown that the large-scale morphological characteristics of these nebulae (lobe size, semi-aperture angle, number of observed lobes) can be related to some of the parameters of the binary system.

Two sets of HST images taken with a time interval of 10.7 years are used in this paper to study the morphology and the proper motions of the jets of CRL 618. The paper is organized as follows, the observations are described in Sect. 2. In Sect. 3 we describe the wavelet technique and the procedure we applied to calculate the proper motion of the emission features of the jets of CRL 618. The results are shown in Sect. 4. We compute numerical simulations of a precessing jet with a variable ejection velocity ejected by the secondary star of a binary system, which are compared with the [S II] HST images (Sect. 5). Finally, we summarize our results in Sect. 6.

4.3. Observations

The images used in this paper to determine the proper motion of the jets of CRL 618 were retrieved from the HST Data Archive¹. Two data sets of CRL 618 were obtained with the HST through some narrowband filters. The first set of images was taken on 1998 November 23 with the Wide Field Planetary Camera 2 (WFPC2) (GO 6761, PI: Trammell), and three narrowband filters selected to isolate the [S II] 6716, 6731 Å emission lines (F673N), the [O I] 6300 Å emission line (F631N), and the H α emission (F656N). The second data set was obtained with the Wide Field Camera 3 (WFC3) on 2009 August 8 (GO 11580, PI: Balick) through three narrowband filters isolating the H α emission (F656N), the [N II] 6584 Å emission line (F658N), and the [S II] 6716, 6731 Å emission lines (F673N). Among the four narrowband filters used, the F673N and F656N are in common in both sets. Note

¹Based on observations made with the NASA/ESA Hubble Space Telescope, and obtained from the data archive at the Space Telescope Science Institute. STScI is operated by the Association of Universities for Research in Astronomy, Inc. under NASA contract NAS 5-26555.

that the $H\alpha$ (F656N) images have two components: the emission formed in the lobes and the scattered component ($H\alpha$ emission scattered by the dust outflow) (Carsenty & Solf 1982; Riera et al. 2011). We measured the proper motion of the bow-shaped and knotty features from the two [S II] images, which proved to be the most suitable because the observed emission arises from the jets. Although the filter names remained the same in both sets, their characteristics have changed (see Table 4.1). Table 4.1 presents the details of the two observations.

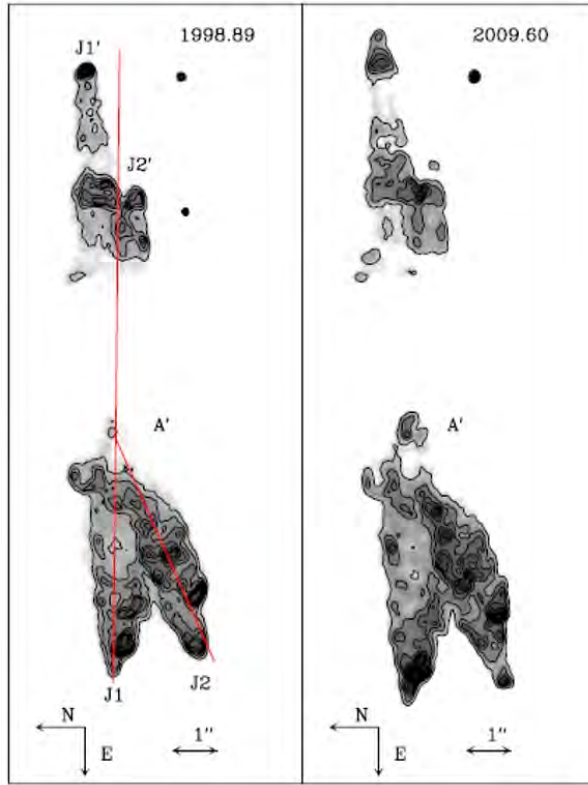


Figure 4.1: CRL 618 in the 1998.89 (left) and 2009.60 (right) [S II] images shown to the same scale and pixel size ($0''.045$). The two frames are aligned spatially and show how the jets move outward. The images have been rotated so that the y-axis lies more or less along the J1 axis. The two jet axes used in this work are also marked. The scale is indicated by the horizontal arrow. The images are displayed with a logarithmic scale (in arbitrary units). Feature A' is labeled (see text).

The first images of CRL 618 were obtained as part of the HST Cycle 6 program 6761. CRL 618 was at the center of the planetary camera which has a field of view of $36'' \times 36''$ and a plate scale of $0''.045 \text{ pixel}^{-1}$. The images were reduced through the HST WFPC2 data reduction pipeline (for a detailed description of the data reduction see Trammell &

Goodrich 2002). The second set of images was obtained as part of cycle 17 (GO 11580, PI: Balick) with the WFC3 ultraviolet and visible channel (UVIS) camera, which has a $20'' \times 20''$ field of view and a plate scale of $0''.0395 \text{ pixel}^{-1}$ (Balick et al. 2013).

The analysis started with the pipeline-reduced data products provided by the Hubble archive. The two-epoch [S II] 6716 + 6731 Å images were converted into a common reference system and rebinned to the same pixel scale ($0''.045 \text{ pixel}^{-1}$). The determination of accurate proper motions requires the multiepoch images to be registered to subpixel accuracy. When the observed field contains many background stars, image registration is easy to implement and the distortions introduced by the optical system can be corrected for. However, in the case of the two [S II] images of CRL 618 only one field star was detected in both exposures. The images were initially aligned using the absolute astrometry as returned by the pipeline reduction. Then both images were rebinned to the same pixel scale ($0''.045 \text{ pixel}^{-1}$) and aligned using the field star and the small structure seen in the innermost part of the east lobe (labeled A' in Fig. 4.1, see also Sánchez Contreras et al. 2002), which has a spectrum different from that of the lobes. Sánchez Contreras et al. (2002) proposed that this region is ionized by the UV stellar radiation and that it corresponds to the outermost parts of the H II region surrounding the star. Balick et al. (2013) proposed that A' (visible in several optical and NIR images) is the central exciting source of CRL 618. We assumed that A' is a stationary feature that was used to align the two [S II] images. The proper-motion measurements obtained with this assumption are along the jet axes (as expected), and the tangential velocity values therefore are consistent with the proper motions displayed by outflows of PNe (such as Hu 1–2, Miranda et al. 2012).

The images were aligned and rotated using the standard IRAF routines GEOMAP and GEOTRAN. The accuracy of the relative alignment between the two images is approximately 0.5 pixels (i.e., $\leq 0''.03$).

4.4. Analysis

The [S II] HST images of CRL 618 show at least four different jets in its lobes (see Fig. 4.1). We named these four jets J1, J2 (in the bright eastern lobe), and J1' and J2' in the faint lobe (as indicated in Fig. 4.1).

4.4.1. Small-scale structure: wavelet technique

The [S II] images of CRL 618 show the complex structure of its jets, with knots, arc-shaped structures, and diffuse emission. A comparison between the two epochs indicates remarkable morphological changes. Because of the complexity of the observed jets, we carried out an analysis based on wavelet transforms, which allow us to obtain a general description of the flow.

The wavelet transform decomposes an image into maps of different scales. In each map, structures with the chosen scales are prominent because they have higher coefficients than those with smaller or larger scales. Wavelet transforms have been used in different astrophysical contexts. For example, Grosdidier et al. (2001) used 2D wavelets to isolate stochastic structures of different characteristic sizes in M 1-67 from its $H\alpha$ image; Riera et al. (2003) studied the complex spatial structure of knots in HH 110 using the wavelet technique. In this paper, we are interested in identifying the characteristics of the complex spatial structure of the lobes of CRL 618 without losing the positional information. This study shares many similarities with the study of the characteristic sizes of knots along HH 110. Therefore, we adopted the procedure developed by Riera et al. (2003).

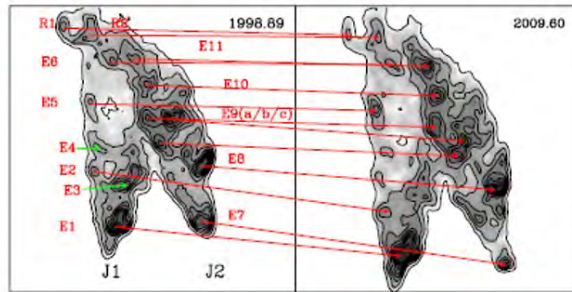


Figure 4.2: Bright (east) lobe in the 1998.89 (left) and 2009.60 (right) [S II] images. Several features along regions J1 and J2 are marked and labeled. Changes in the structure of the labeled features between both epochs are discussed in the text. The red arrows show the assumed identifications of corresponding knot pairs in the two epochs.

The two-dimensional wavelet transform analysis is used to obtain the position of the features of its lobes. We rotated the images of each jet so that the jet axis is parallel to the ordinate. The jet axes are shown in Fig. 4.1. On these rotated images, we carried out a decomposition on a basis of anisotropic wavelets, which have different sizes along and across the radial (axial) direction. Following Riera et al. (2003), we used a basis of

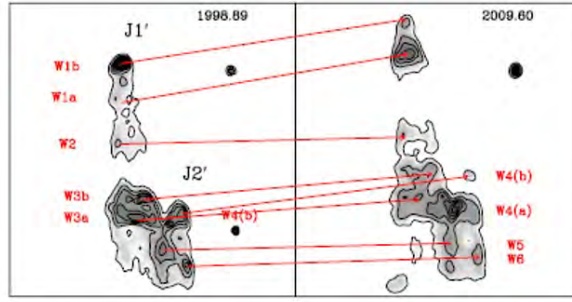


Figure 4.3: Same as Fig. 4.2, but for the jets of the faint (west) lobe (labeled J1' and J2').

“Mexican hat” wavelets of the form

$$g(r) = C(2 - r^2)e^{-r^2/2}, \quad (4.1)$$

where $r = [(x/a_x)^2 + (y/a_y)^2]^{1/2}$, $C = (a_x^2 + a_y^2)^{-1/2}$, and a_x and a_y are the scale lengths of the wavelet along the x- and y-axes respectively. Following Riera et al. (2003), we chose a range for a_x and a_y , which were taken to have integer values from 1 to 60 pixels (i.e., from $0''.045$ to $2''.70$), and we then compute the convolutions

$$T_{a_x, a_y}(x, y) = \int \int I(x', y') g(r') dx' dy', \quad (4.2)$$

where $r' = [(x' - x)/a_x]^2 + [(y' - y)/a_y]^2]^{1/2}$, and $I(x, y)$ is the observed emission map as a function of position (x, y) . These convolutions are calculated with a standard FFT algorithm.

We computed the transform maps $T_{a_x, a_y}(x, y)$ for the [SII] images for each jet at the two epochs. The convolved maps were used as follows. First, we fixed the position of y on the observed intensity map and found the values of x_k ($k = 1, 2, 3$) where the intensity map has a local maximum. For each pair (x_k, y) where $I(x, y)$ has a maximum, we determined $(a_{x,k}, a_{y,k})$ in the a_x and a_y -space where wavelet transform has a local maximum. In this way, we detected the characteristic size of a feature with an intensity maximum at (x_k, y) . The results obtained with the process described above are shown in Figs. 4.4 and 4.5. Figures 4.4 and 4.5 show the characteristic sizes of the small structures of the bright lobe (Fig. 4.4) and the faint lobe (Fig. 4.5) as a function of position along each jet axis.

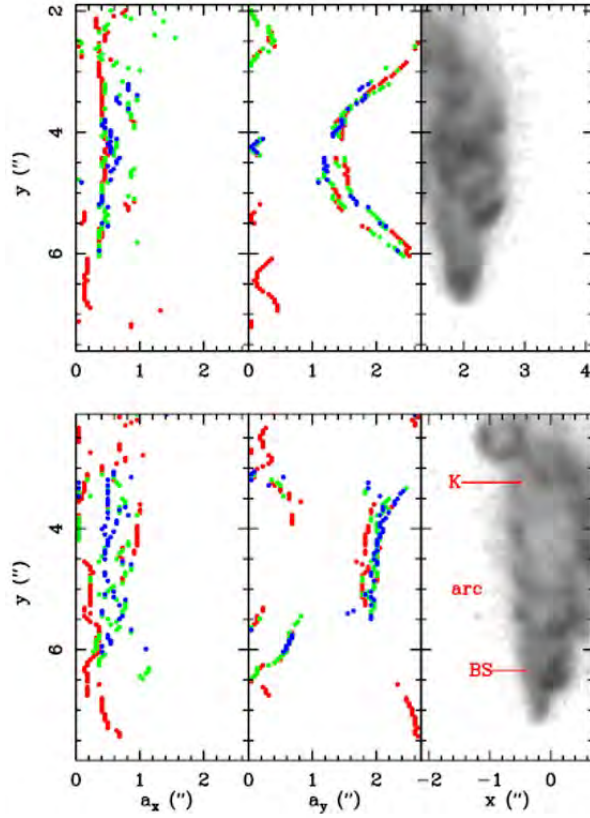


Figure 4.4: First-epoch [S II] image of the J1 (bottom) and J2 (top) jets and the characteristic sizes of the small-scale features observed in the optical lobes ($a_{x,k}$ (left) and $a_{y,k}$ (right)) as a function of position y along the jet axis, obtained from the wavelet analysis. The $k = 1$ peaks are represented in red, $k = 2$ in green, and $k = 3$ in blue. Three examples of the compact knots (K), arc, and leading bow-shock (BS) classes are labeled.

4.4.2. Proper-motion measurements

The first- and second-epoch F673N images used for the proper-motion measurements were converted into a common reference system and rotated so that the y -axis lay along the bipolar axis.

The resulting images are shown in Figs. 4.1, 4.2 and 4.3, which also show the assumed identifications of corresponding feature pairs in the two epochs. Strong changes in morphology occur over this time period. These structural changes add uncertainties to the proper-motion measurements and in a few cases even prevent their determination.

Several features within the lobes of CRL 618 exhibit significant morphological changes in the 10.7 years that passed between the two epochs. Knot E3 was a bright feature in the 1998.89 image but in the second epoch (2009.60) it faded and changed from an arc-shaped

morphology to being stretched – and more diffuse – along the jet axis. Knot E4 also faded over this time period. These changes made reliable proper motion measurements for E3 and E4 impossible. Although structure E9 (a/b/c) has varied significantly in morphology over the time period, we computed the proper motion of each knot (i.e., features E9a, E9b and E9c) and the proper motion of the whole structure.

In Fig. 4.1 one can see that some of the features show clear proper motions. We computed the two-dimensional cross correlation function of the emission detected within previously defined boxes containing the emission features under study (Fig. 4.2). We also defined four boxes (shown in Fig. 4.6) including the J1, J2, J1' and J2' emission regions. Finally, the proper motions were determined through a parabolic fit to the peak of the cross-correlation (see Reipurth et al. 1992; and López et al. 1996 for a description of this method). The uncertainty in the position of the correlation peak was estimated through the scatter of the correlation peak positions obtained from boxes different from the nominal one in 0 or ± 2 pixels (or $0.''090$) in any of its four sides. The error adopted includes the uncertainty in the relative alignment between the two images ($\leq 0.''03$) and the uncertainty in the position of the correlation peak. The uncertainty in the identification of corresponding knot pairs are not included in the errors quoted in Table 6. The numerical results are presented in Table 4.2, which includes the derived proper motions (in $\text{milliarcsec yr}^{-1}$), the tangential velocities (in km s^{-1}) for an adopted distance of 1 kpc (Goodrich 1991; Sánchez Contreras et al. 2004), and the position angle of the proper-motion vectors.

4.5. Results

4.5.1. Small-scale structure

The results obtained with the wavelet analysis are shown in Figs. 4.4 and 4.5. The distances are measured from A'.

Figure 4.4 shows $a_{x,k}$ and $a_{y,k}$ ($k = 1, 2, 3$) as a function of position (y) along the jet for the two jets identified in the bright (east) lobe. We describe the characteristic sizes of the small-scale structures along J1 to explore the information that can be extracted from the wavelet technique. At $y \simeq 3.''0$ (i.e., at knot E6) the width ranges from $0.''5$ to $0.''8$ and the size along feature E6 shows a V-shaped feature with a decrease toward the intensity peak and then increases up to $0.''6$ toward the east. At larger y (from $3.''5$ to $4.''7$) the structures become elongated with a more or less constant value of $a_{y,k} \sim 2.''0$ (i.e., a projected size

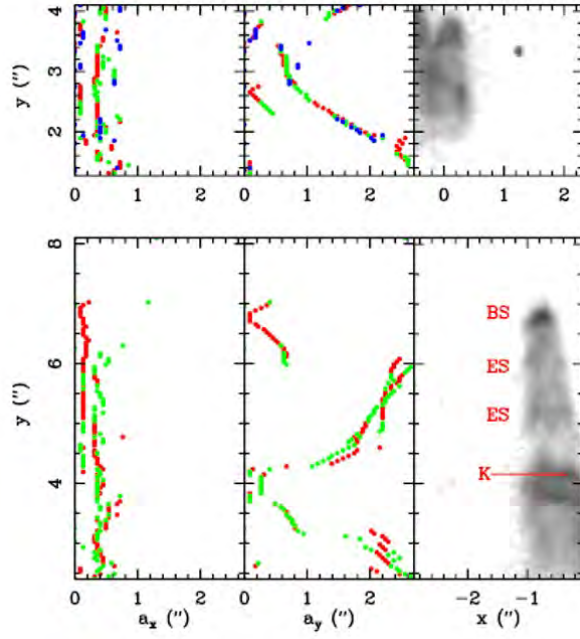


Figure 4.5: Same as Fig. 4.4, but for the faint lobe. The J1' jet is presented in the bottom panel. The J2' jet is shown in the top panel. Three examples of the compact knots (K), elongated structures (ES), and leading bow shock (BS) classes are labeled.

of 3.0×10^{16} cm at the adopted distance). At the arc including E4, $a_{y,k}$ remains constant ($\sim 1.''8$ – $2.''0$) and the characteristic width ranges from $\sim 0.''3$ to $0.''8$. At $y \simeq 5.''2$ to $5.''8$ (i.e., the arc delimited by knots E2 and E3) we see a transition from structures which are elongated along the jet axis to knotty/clumpy features characterized by widths from $0.''2$ up to $0.''7$, and $a_{y,k}$ either lower than $0.''25$ or higher than $1.''0$. Finally, knot E1 and its tail (at y distances from $6.''0$ to $7.''2$) show a V-shaped feature in the $a_{y,k}$ vs. y plot, with values from $\sim 0.''8$ at the tail to $\leq 0.''05$ (i.e. unresolved) at the intensity peak, while the $a_{x,k}$ values range from $0.''2$ to $0.''6$.

Both jets (J1 and J2) show elongated structures with similar values at the central region of each jet ($y = 3.''5$ to $5.''7$). In Fig. 4.4 we can compare the overall behavior of the width across the outflows J1 and J2 as a function of distance along the jet axis ($a_{x,k}$ vs. y). Along J1, $a_{x,k}$ decreases more or less monotonically from $\sim 1.''0$ at E6 to $0.''2$ at E1 (i.e., along $3''$). We deduce that the J1 outflow narrows with the distance to the central source with a half-opening angle $\sim 15^\circ$. J2 shows a more or less constant width (with an $a_{x,k}$ mean value of $0.''5$) for y distances up to $6.''0$ and a significantly lower value ($\leq 0.''2$) at E7. J2 is more clumpy, showing a larger number of compact knots (detected as V-shaped features in the $a_{y,k}$ vs. y plot).

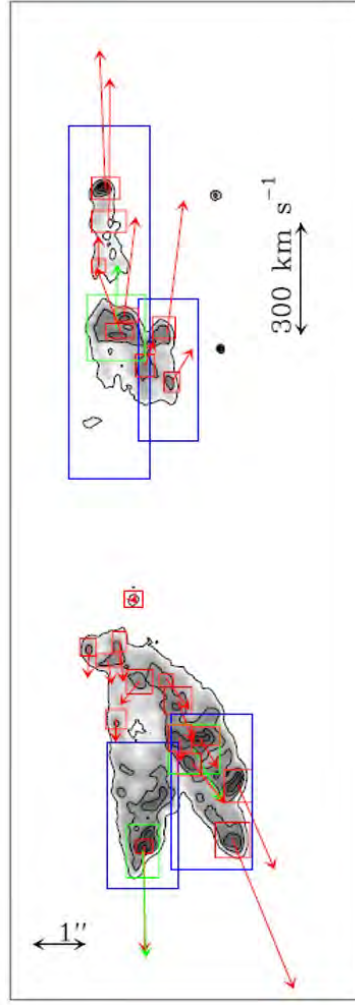


Figure 4.6: Proper motions of the individual features in the jets of CRL 618. First-epoch [S II] image of CRL 618 together with the boxes in which the cross-correlations were made (see text). The red boxes correspond to individual knots. Features that include more than one knot (as E1, E9 and W3) are marked in green. The blue boxes were used to measure the proper motion of the J1, J2, J1' and J2' jets. The arrows show the computed proper motions. The length of each arrow is proportional to the proper motion. The vertical arrow at the top right shows a proper motion of 300 km s^{-1} .

A similar analysis was applied to all jets (i.e. J1, J2, J1' and J2'). We searched for patterns in the appearance of the small-scale features based on the size across and along the jet axis. We considered morphological classes: knots (either compact knots and leading bow-shocks), elongated (along the jets axis) features, and elongated and wide arcs. The compact-knot class is composed of features that show low values of $a_{x,k}$ and $a_{y,k}$ as W3a, W3b and E11. The compact knots have sizes $\sim 6 \times 10^{15} \text{ cm}$ along and across the jet

axis. The leading bow-shocks (E1, E7, W1b) have widths ranging from 1.5×10^{15} cm to $\leq 10^{16}$ cm, while the characteristic sizes along the flow are $\leq 1.2 \times 10^{16}$ cm. The elongated features include W1a, W2 and E10, having $a_{x,k} \leq 6 \times 10^{15}$ cm and $a_{y,k} \geq 3 \times 10^{16}$ cm. The elongated and wide arc class includes the E4 arc and the E2+E3 arc, which have $a_{x,k} \leq 1.5 \times 10^{16}$ cm and $a_{y,k} \simeq 1.5$ to 3×10^{16} cm.

4.5.2. Proper-motion measurements

Figure 4.6 shows the proper-motion measurements obtained through the process described in Sect. 4.4.2. The resulting tangential velocities (for a distance of 1kpc toward CRL 618) and the position angles are given in Table 4.2. The J1' and J2' jets (west lobe) have velocities with moduli ~ 120 km s^{-1} and approximately along the jet axes. The proper motions we obtained for the outer knots of CRL 618 are roughly consistent with the proper motions of ~ 300 km s^{-1} reported by Balick et al. (2013). Balick et al. (2013) extracted their results from a pair of F606W images obtained from the ACS in 2002.6 and WFC3 in 2009.6. These authors determined the overall expansion of the outer bow-shocks by applying a magnification factor to the first image.

All the knots show proper motions in the direction of the corresponding jet axis (either the J1, J2, J1' or the J2' jet axes), with the exception of knot E6. As can be seen, there are strong velocity variations along the jets, with tangential velocities ranging from 60 km s^{-1} to 430 km s^{-1} . In Fig. 4.7, we show the tangential velocities as a function of distance d to the feature A'. As is clear from this figure, the tangential velocities rapidly increase for increasing distances from the central source. The outer (bowshock- like) knots show the highest proper-motion values, from 245 up to 430 km s^{-1} . We find the largest proper motion measurement at knot E7 (i.e., the leading bow shock-feature of the J2 jet), which shows a value ~ 430 km s^{-1} . Large proper motions were also measured in the leading bow-shocks of J1' and J2' (W1a/b, W4b) with a mean value ~ 370 km s^{-1} . Finally, knots E1 and E8 have tangential velocities that are significantly lower than the values reported above (i.e., 288 and 245 km s^{-1} respectively). The innermost knots (i.e., E5, E6, W5 and W2) have the lowest tangential velocities with values ≤ 100 km s^{-1} . Several knots at $d=3''.0$ to $6''.0$ show intermediate velocity values, which range from 100 to 200 km s^{-1} .

We calculated the kinematic age ($\tau_{kin} = (x^2 + y^2)^{1/2}/(\mu_x^2 + \mu_y^2)^{1/2}$) of the outermost bow shock-like knots. Knots E1 and E7 have a kinematic age of ~ 100 years. The W1b and W4b have kinematical ages that are younger (~ 85 years (W1b) and 50 years (W4b)).

These values agree with the age of ~ 100 yr reported by Balick et al. (2013).

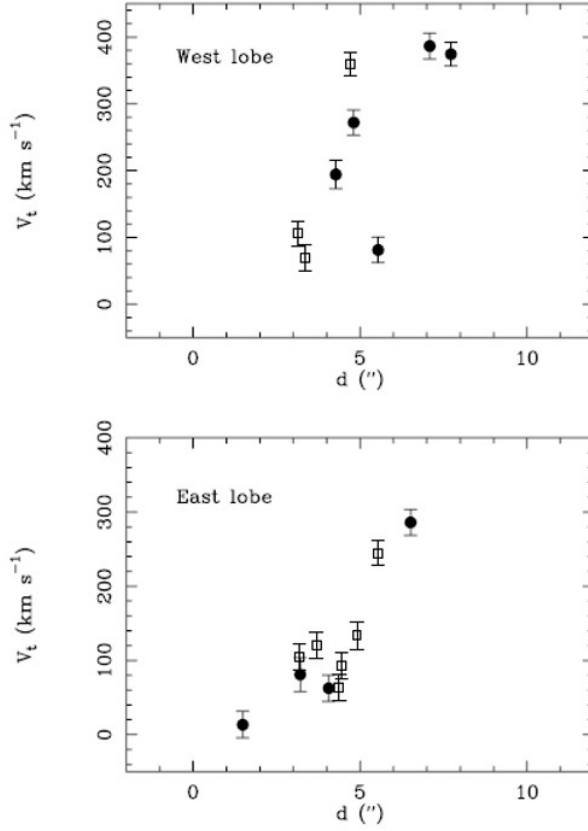


Figure 4.7: Tangential velocity as a function of distance to the central H II region. Top panel: faint lobe (J1' (circles), J2' (squares)). Bottom panel: bright lobe (J1 (circles), J2 (squares)).

4.6. Numerical simulations

4.6.1. Code description and initial setup

We calculated 3D numerical simulations with the YGUAZÚ-A hydrodynamical code (Raga et al. 2000), which integrates the gasdynamical equations with a second-order accurate scheme (in time and space) using the “flux-vector splitting” method of van Leer (1982) on a binary adaptive grid. Together with the gas-dynamic equations, several rate equations for atomic/ionic species were also integrated. These species are H I, H II, He I, He II, He III, [C II], [C III], [C IV], [N I], [N II], [N III], [O I], [O II], [O III], [O IV], [S II], and [S III] (see details of the reaction and cooling rates in Raga et al. 2002). These rate equations enable the computation of a nonequilibrium cooling function. Considering the

temperature and density distributions obtained from the numerical simulations, we can compute the [S II] $\lambda\lambda$. 6716, 6730 emission coefficients. The intensities of the forbidden lines [S II] $\lambda\lambda$ 6716, 6730 were calculated by solving five-level atom problems, using the parameters of Mendoza (1983). These intensities can be integrated along the line of sight to produce synthetic emission maps.

A computational domain of $(1.5, 1.5, 3) \times 10^{17}$ cm along the x-, y-, and z-axes, respectively, was employed. These sizes correspond to the observed angular size for a distance of 1 kpc. An adaptive Cartesian grid with five refinement levels was used, achieving a resolution of $\sim 5.9 \times 10^{14}$ cm ($\sim 0''.040$ at a distance of 1 kpc) at the finest level, corresponding to $(256 \times 256 \times 512)$ pixels in a uniform grid.

Following the work of Velázquez et al. (2012; see also Velázquez et al. 2013), we considered a precessing and a time-dependent ejection velocity jet, that is launched from the companion star of a binary system. This jet propagates into a dense and slow wind of the AGB primary star. At the initial time (and filling the whole computational domain), we imposed an isotropic, constant velocity AGB wind with a density distribution, that considers the final superwind phase of the AGB star (Mellema 1995), given by

$$\rho_w = \frac{1}{2}[(\rho_{sup} + \rho_{AGB}) + (\rho_{sup} - \rho_{AGB}) \cos \epsilon] \left(\frac{r_w}{r}\right)^2, \quad (4.3)$$

which is:

$$\epsilon = \pi \min[1, \max[0, \frac{r - (r_w + v_w t_{sup})}{v_w t_{trans}}]], \quad (4.4)$$

where r is the distance from the primary star, v_w is the terminal wind velocity, and r_w is the stellar wind radius. In Eq. (4.4) the times t_{sup} and t_{trans} indicate the duration of the superwind phase and the time of transition between the AGB wind and the superwind phase. The densities ρ_{AGB} and ρ_{sup} are calculated as

$$\rho_{AGB, sup} = \frac{\dot{M}_{AGB, sup}}{4\pi r_w^2 v_w}, \quad (4.5)$$

where \dot{M}_{AGB} and \dot{M}_{sup} are the mass loss rates of the AGB and the superphase AGB winds, respectively. Based on observational results (Neri et al. 1992; Pardo et al. 2004; Sánchez-Contreras et al. 2004; Nakashima et al. 2007; Bujarrabal et al. 2010; Lee et al. 2013), we chose $\dot{M}_{AGB} = 10^{-5} M_\odot \text{ yr}^{-1}$, $\dot{M}_{sup} = 10^{-4} M_\odot \text{ yr}^{-1}$, $v_w = 15 \text{ km s}^{-1}$, $r_w = 3.6 \times 10^{15} \text{ cm}$ (equivalent to 6 pixels in the finest grid) and a constant temperature $T_w =$

100 K (this initial constant temperature acquires a decreasing profile with distance r , as the time-integration proceeds).

Table 4.3: Parameters employed in the models.

Model	p	$q=\tau_p/\tau_o$	m_2/m_1	$\tau_o(\text{yr})$	a(AU)	Decrease
M1a	4	2	14.8	15.4	12.3	no
M1b	4	2	14.8	15.4	12.3	yes
M2a	3	3	7.0	13.7	9.1	no
M2b	3	3	7.0	13.7	9.1	yes
M3a	2	4	4.3	15.4	8.4	no
M3b	2	4	4.3	15.4	8.4	yes

The bipolar outflow was injected at the center of the computational domain inside a cylindrical volume with radius r_j and length l_j , both equal to r_w . The jet axis precesses, describing a cone with a half-opening angle α . The precession period τ_p is related to the dynamical time τ_{dyn} and the orbital period τ_o by $\tau_{dyn} = p \tau_p$ and $\tau_p = q \tau_o$, where p and q a pair of free dimensionless parameters (Velázquez et al. 2012; Velázquez et al. 2013). The jet velocity is given by

$$v_j = v_{j0}(1 + \Delta v \sin(\omega_o t)), \quad (4.6)$$

where ω_o is $2\pi/\tau_o$, v_{j0} is the mean velocity and Δv is the amplitude of velocity variation. The semiaperture angle α , the mean jet velocity v_{j0} , and the initial number density n_j were set to 15° , 400 km s^{-1} and 10^6 cm^{-3} , respectively, for all models. The amplitude of the velocity variation was set to $v_{j0}/2$ for all models. With these values for v_{j0} and n_j , the average mass-injection rate of the jet is $\dot{M}_j = 5.6 \times 10^{-5} \text{ M}_\odot \text{ yr}^{-1}$.

In $\sim 120 \text{ yr}$ (the total integration time of our simulations) the bipolar outflow injects a total mass of $1.3 \times 10^{-2} \text{ M}_\odot$. into the surrounding medium.

With these values of injected mass and mean jet velocity, the linear momentum injected by the jet (in 120 yr) is $4.4 \text{ M}_\odot \text{ km s}^{-1}$, which agrees with the observational estimate of $4 \text{ M}_\odot \text{ km s}^{-1}$ (Bujarrabal et al. 2001). The value of $q=\tau_p/\tau_o$ gives the m_2/m_1 ratio, employing the results of Terquem et al. (1999) and Raga et al. (2009) (see Table 4.3). We set $m_1 = 0.5 \text{ M}_\odot$ (of the star which launches the jets) and the eccentricity $e = 0.5$ (actually, the value of e has little influence on the overall PN morphology, see Velázquez

et al. 2013). In Table 4.3 we also list the values of the orbital period and radius employed in our models.

4.6.2. Numerical results

Velázquez et al. (2012, 2013) have shown that a precessing jet in a binary system with a time-dependent velocity produces nebulae with multipolar morphology. A quadrupolar morphology similar to CRL 618 is obtained by setting $q = 2, 3$ or 4 . Because the adopted velocity variability period is the orbital period, and to have three or four ejections for each lobe along the 120 yr, we chose $p = 4$, for the case with $q = 2$ (model M1a), $p = 3$ for $q = 3$ (model M2a), and $p = 2$ for $q = 4$ (model M3a).

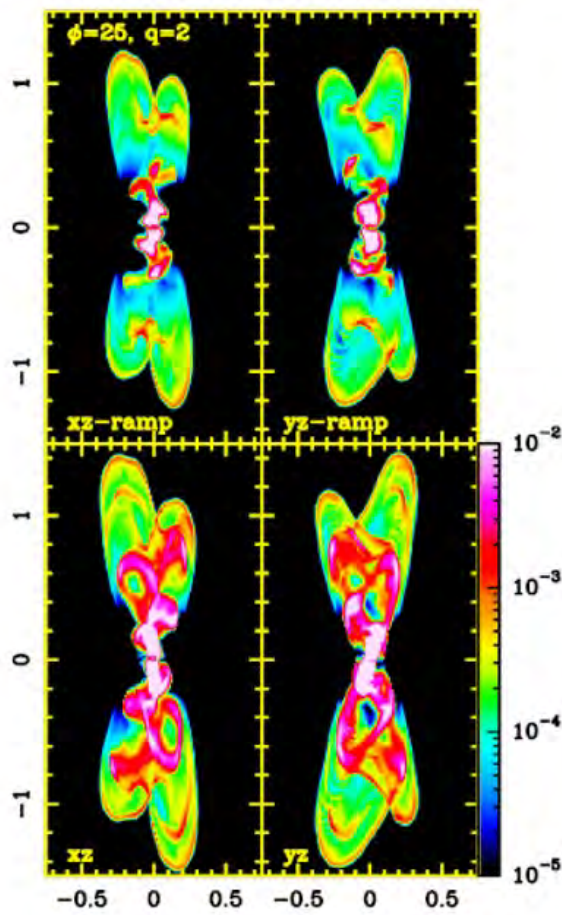


Figure 4.8: Synthetic [S II] emission maps obtained from models M1a (bottom panels) and M1b (top panels). The right panels display the yz projection for both models, while the left panels display the xz projection. The angle between the precession axis and the plane of sky was set to 25° for all models. The vertical color bar gives the [S II] flux in units of $\text{erg s}^{-1} \text{cm}^{-2} \text{sr}^{-1}$. The vertical and horizontal axes are given in units of 10^{17} cm .

We also carried out three more runs (M1b, M2b, and M3b) for which the mean velocity v_{j0} (see Eq. 4.6) was modified to be a decreasing function of time. For simplicity, we imposed a linear decrease with a rate of $3 \text{ km s}^{-1} \text{ yr}^{-1}$ (i.e. v_{j0} , after $t=120 \text{ yr}$, decreases to 10 % of its initial value).

As discussed in Sect. 4.6.3, such a systematic decrease in the ejection velocity is needed to reproduce the proper motions of CRL 618. This decrease in v_{j0} with time could be the result of the presence of a longer-period ejection velocity variability mode, but the currently observed lobes of CRL 618 do not give appropriate constraints for the amplitude and period of this mode.

From the density and temperature distributions given by the numerical simulations, synthetic [S II] emission maps were computed for all models. Figure 4.8 displays the maps obtained for models M1a (bottom panels) and M1b (top panels) for the xz and yz -projections, at an integration time of 120 yr. The synthetic maps obtained for models M2a and M2b (models M3a and M3b) are shown in Fig. 4.9 (Fig. 4.10). These maps were obtained considering that the z -axis is tilted by 25° , with respect to the plane of the sky.

To explore whether or not our predicted maps show a small-scale structure similar to that observed in the lobes of CRL 618, we applied the wavelet analysis (as described in Sect. 4.4.1) to the synthetic map of the M2b simulation (yz -projection, at an integration time of 120 yr). The scale lengths of wavelets along the x - and y -axis were taken to have integer values from 1 to 60 pixels (i.e. from $0''.04$ to $2''.40$). The results are shown in Fig. 4.11.

On these synthetic maps, we also carried out the proper motion study that was performed for the observations (described in Sect. 4.4.2). To do this, the simulations were restarted from the output corresponding to an integration time of 120 yr and were left to evolve 10 yr longer. The results of the proper-motion study are shown in Figs. 4.12 and 4.13.

4.6.3. Comparison with observations

For all the computed models, emission structures similar to the jets of CRL 618 were obtained. As mentioned above, a quadrupolar morphology is predicted for all models presented in this work (the yz -projection maps of models M3a and M3b display a bipolar morphology). All synthetic maps show leading bow-shocks together with several arcs/rings and knots with a qualitative similarity to the morphology of the jets of CRL 618.

However, our synthetic maps show an overall point-symmetric morphology, which is not observed in the CRL 618 images.

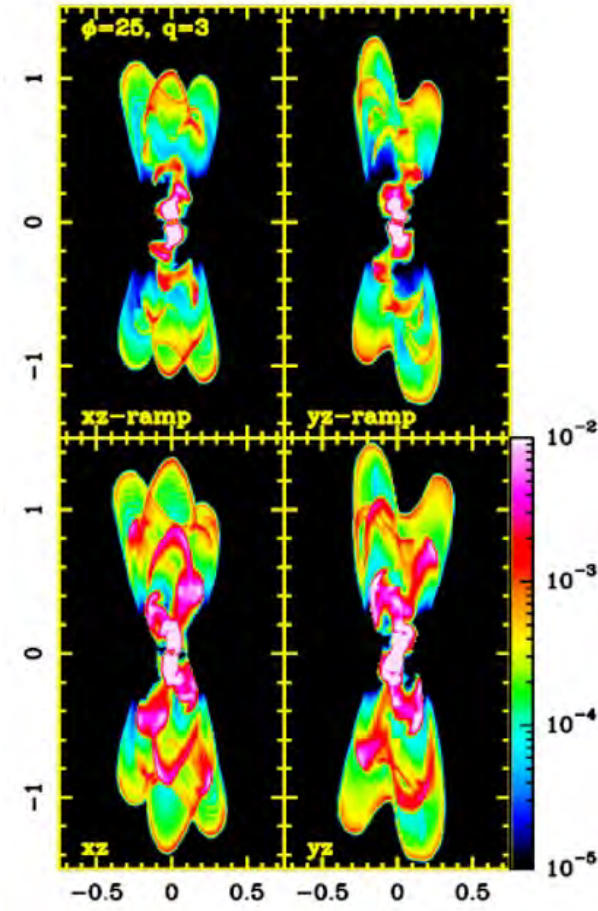


Figure 4.9: As Fig. 4.8, but for models M2a (bottom panels) and M2b (top panels).

As mentioned above, the wavelet analysis was applied to the predicted [S II] images (see Figs. 4.12 and 4.13). For this analysis, the synthetic map obtained from model M2b was rotated so that the jet axes lay parallel to the y -axis. The angular distance was measured from the jet injection point and the adopted distance to the object was 1 kpc. These figures show the $a_{x,k}$ and $a_{y,k}$ as a function of y for the two predicted jets, and the position of the local intensity maxima (i.e. (x_k, y) for $k=1, 2, 3$) are superimposed on the [S II] synthetic image.

When we applied the wavelet analysis to this synthetic image we obtained the typical sizes of the small-scale structure. The compact knots have widths across the jets $\leq 6 \times 10^{15}$ cm (i.e. $0.''4$) and show a V-shaped structure in the $a_{y,k}$ vs. y plot. Some of the leading bow-shocks (as seen in Fig. 4.11) have small widths across the jet (which are more or less constant, with $a_{x,k} \simeq 6 \times 10^{15}$ cm), and a V-shaped structure in the $a_{y,k} - y$ diagram. The elongation of these V-shaped structures decreases from $\sim 2.''0$ at their edges to $0.''1$ at the intensity peak. The wavelet analysis allows us to characterize the elongated structures with

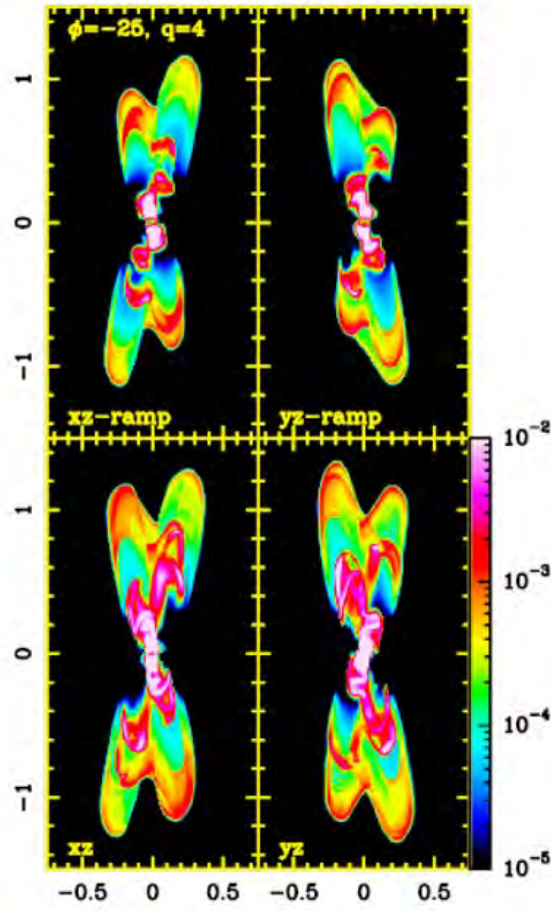


Figure 4.10: As Fig. 4.8, but for models M3a (bottom panels) and M3b (top panels).

$a_{y,k}$ values ranging from 1."2 to 2."0 (i.e. 1.8×10^{16} cm to 3×10^{16} cm) which are similar to the elongated structures detected in the jets of CRL 618. The observed morphological classes (i.e., knots, bow-shocks, elongated structures and arcs) also appear in the wavelet analysis of the predicted [S II] maps. Moreover, the sizes of the predicted emission features clearly agree with the observed ones.

We carried out the proper-motion study as described in Sect. 4.4.2, using two [S II] emission maps computed for two epochs at a 10 yr time interval. The results obtained with the model M2b (projection yz) are shown in Figs. 4.12 and 4.13. Figure 4.12 shows the boxes used for the calculation, and the resulting proper motions are shown as red arrows. We clearly see that all features show proper motions in the direction of the corresponding jet axis, a result found in all six models.

From the predictions of models a, we find tangential velocities from 200 to 500 km s⁻¹, which are higher than the observed values (see Sect. 4.5.2). The tangential velocities

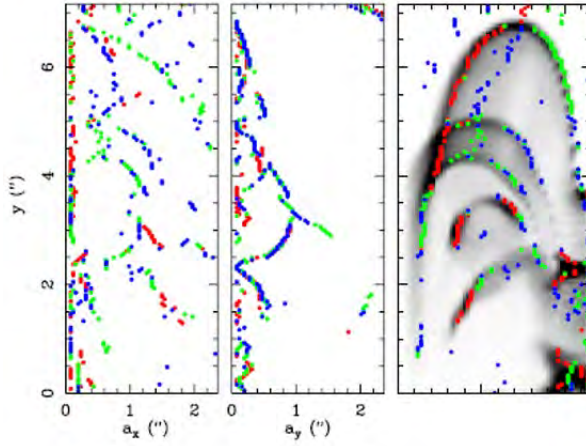


Figure 4.11: Wavelet study performed on the top-left lobe or jet of the model M2b. The [S II] image obtained from this model at a $t = 120$ yr integration time is shown in the right panel. For each y , the location of the three maxima of the intensity map are shown as dots superimposed on this image (first maximum in red, second maximum in green and third maximum in blue). The characteristic sizes ($a_{x,k}$ in the left panel; $a_{y,k}$ in the central panel) are shown as a function of position y along the jet axis.

derived from the M1a and M2a models show a quite wide dispersion, and basically no correlation is seen between the tangential velocity and the distance to the central source. To reproduce the apparent acceleration of the knots of the jet of CRL 618 with distance, it was necessary to superimpose on the periodic velocity variability a trend of decreasing ejection velocity (v_{j0}) over time. We computed three models (M1b, M2b and M3b) for which the mean jet velocity is a linear decreasing function of time. For these two models we found tangential velocities ~ 100 to 350 km s^{-1} . The results obtained for model M2b are presented in Fig. 4.13. As a function of distance d , v_t shows a quite wide scatter, and a general trend of increasing velocities from the inner knots to the leading bow-shocks. The v_t vs. d plot shows a more or less monotonic growth, reaching a value of $\sim 350 \text{ km s}^{-1}$ at the outer bow-shocks. Similar results were found for model M1b. All three models (M1b, M2b, and M3b) reproduce the distance dependence of the tangential velocities observed in CRL 618.

An obvious difference between CRL 618 and all of our models is the fact that while the models show point-symmetries between the corresponding components of the outflow lobes, CRL 618 does not show such symmetries. The point symmetrical structure in our models is a direct result of the fact that we imposed a point-symmetrical, precessing

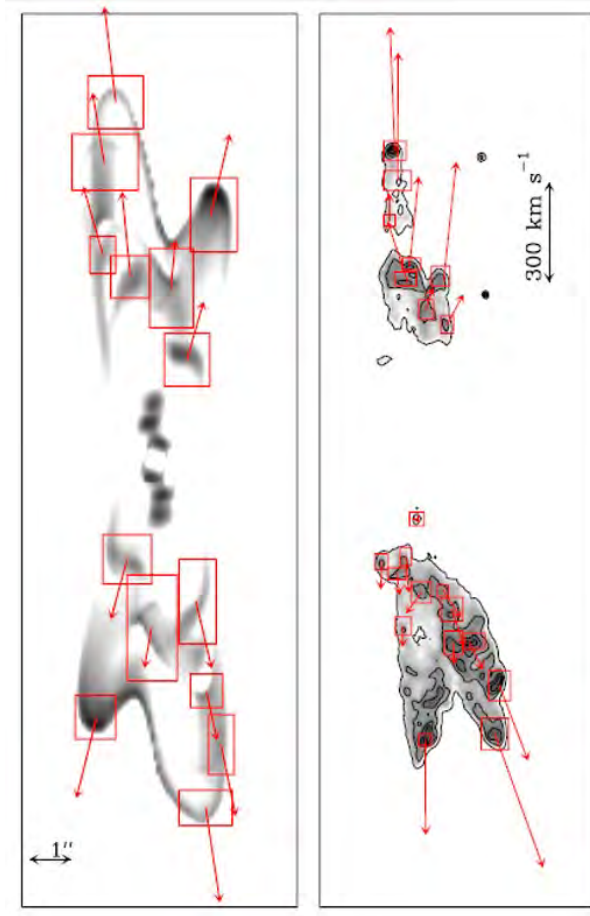


Figure 4.12: Left panel: proper motions of the individual features in the synthetic [S II] map (model M2b) together with the boxes in which the cross-correlations were made. The red arrows show the computed proper motions. The length of each arrow is proportional to the proper motion. Right panel: proper motions of the individual knots of CRL 618, included for comparison. Both images are shown to the same spatial scale. The vertical arrow at the top right shows a proper motion of 300 km s^{-1} .

jet/counterjet ejection.

This symmetry discrepancy between our models and CRL 618 indicates that the structures observed in this object do not correspond to point-symmetrical ejections. The lack of point-symmetry could be an indication of the presence of effects similar to those found in the models of Montgomery (2012), in which the tidally induced disk precession changes the point of impact of an accretion column from a mass-exchanging binary companion. This process results in clear differences between the two faces of the accretion disk and would probably result in substantial differences between the two outflow lobes produced by the inner disk regions.

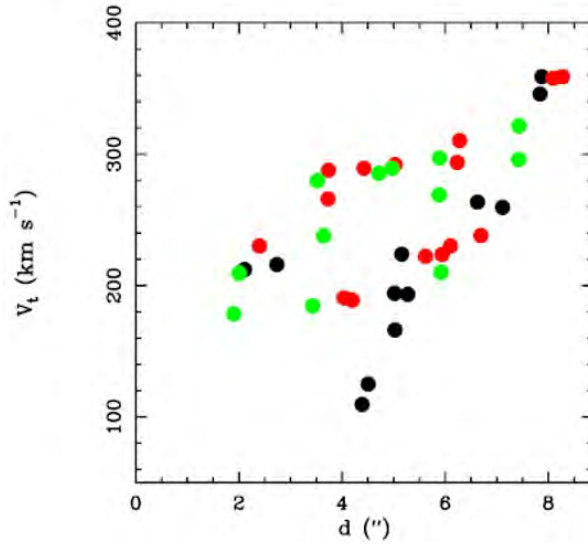


Figure 4.13: Tangential velocity of the individual features in the synthetic [S II] map obtained for model M1b (black), M2b (red) and M3b (green) at a $t = 120$ yr integration time as a function of distance to the jet injection point.

4.7. Summary and discussion

We have reanalyzed the [S II] HST images of CRL 618 obtained by Trammell & Goodrich (2002) and Balick et al. (2013). We applied an anisotropic wavelet analysis technique to calculate the characteristic sizes along and across the CRL 618 jets. From this analysis, we found four morphological classes: compact knots (which have sizes along and across the axis $\sim 6 \times 10^{15}$ cm), outermost bow-shocks (with widths ranging from $\sim 1.5 \times 10^{15}$ cm to 10^{16} cm, and sizes smaller than $\sim 1.2 \times 10^{16}$ cm along the jet), elongated features (with $a_{x,k} \leq \sim 6 \times 10^{15}$ cm, $a_{x,k} \geq 3 \times 10^{16}$ cm), and arcs.

From the archival [S II] HST images of CRL 618 with a 10.7 yr time base, we carried out proper-motion measurements of the knots, arcs, and bow-shocks observed in the lobes of CRL 618, computing the two-dimensional cross-correlation function of the emission detected within the chosen boxes. The proper motions were calculated through a parabolic fit to the peak of the cross-correlation. We found proper motions which are well-aligned with the jets axes (either the J1, J2, J1' or J2' axis), and tangential velocities ranging from 60 to 430 km s^{-1} . These velocities agree to within 15 % with the H α proper motions of Balick et al. (2013) after correcting these velocities for the distance of 0.9 kpc adopted by these authors. From our proper-motion measurements and the distance to the central

source, we calculated the kinematic age for several features. We found $\tau_{kin} \sim 50$ to 100 yr, ages increasing with the distance to the central source.

We found that the tangential velocity is a monotonically increasing function of distance d , with the highest proper motions at the outermost bow-shocks (with velocities up to 430 km s^{-1}). A ramp of increasing radial velocities versus distance is seen in the outer regions of the bright lobe of CRL 618 (Sánchez Contreras et al. 2002; Riera et al. 2009). Therefore, the jet ejection velocity shows a monotonic increase with distance to the central source, which we interpret as a systematic decrease of the ejection velocity over time.

We modeled the jets of CRL 618 as a precessing jet with a time-dependent ejection velocity that is launched from the secondary star of a binary system. The [S II] intensity maps predicted for the sinusoidal ejection velocity models have morphologies that agree with the [S II] HST images of CRL 618. The increase of the tangential velocity (and also the increase of radial velocity) with distance to the central source requires a mean jet velocity that varies over time. The dependence of the tangential velocities with distance to the central source can be reproduced when we impose a linear decrease of the mean v_{j0} over time.

From the comparisons we made between the structure and proper motions observed in CRL 618 and predictions from 3D jet simulations, we predict the presence of the following elements:

- a well-collimated, bipolar ejection,
- a precession of the outflow axis,
- an approximately periodic time-variability of the outflow velocity with a period on the order of 15 yr (the orbital one),
- a general, long-term trend of decreasing outflow velocities from dynamical timescales of ~ 50 yr toward more recent times.

It is currently not possible to say whether or not the long-term trend of decreasing outflow velocity vs. time might be part of a longer-period, quasi-periodic variability. If that were the case, new knots along the CRL 618 jets at future times would show larger proper motions. The younger present-day astronomers might yet be able to observe this effect.

Acknowledgements. A.Ri., R.E., and A.C. are partially supported by Spanish MCI grants AYA2008-06189-C03 and AYA2011-30228-C03, and FEDER funds. PFV and ACR acknowledge support from CONACyT grants 61547, 101356, 101975, 167611, and UNAM

DGAPA grant IN105312.

References

- Balick, B., Huarte-Espinosa, M., Frank, A., et al. 2013, *ApJ*, 772, 20.
- Bujarrabal, V., Castro-Carrizo, A., Alcolea, J., & Sánchez Contreras 2001, *A&A*, 377, 868.
- Bujarrabal, V., Alcolea, J., Soria-Ruiz, R., et al. 2010, *A&A*, 521, A3
- Carsenty, U., & Solf, J. 1982, *A&A*, 106, 307
- Cernicharo, J., Guelin, M., Penalver, J., Martin-Pintado, J., & Mauersberger, R. 1989, *A&A*, 222, L1
- Cox, P., Huggins, P. J., Maillart, J.-P., et al. 2003, *ApJ*, 586, L87
- Dennis, T. J., Cunningham, A. J., Frank, A., et al. 2008, *ApJ*, 679, 1327
- Goodrich, R. W. 1991, *ApJ*, 376, 654
- Grosdidier, Y., Moffat, A. F. J., Blais-Ouellette, S., Joncas, G., & Acker, A. 2001, *ApJ*, 562, 753
- Guerrero, M. A., Miranda, L. F., Riera, A., et al. 2008, *ApJ*, 683, 272
- Haro-Corzo, S. A. R., Velázquez, P. F., Raga, A. C., Riera, A., & Kajdic, P. 2009, *ApJ*, 703, L18
- Kwok, S., & Bignell, R. C. 1981, *ApJ*, 276, 544
- Kwok, S., & Feldman, P. A. 1984, *ApJ*, 247, 67
- Lee, C.-F., & Sahai, R. 2003, *ApJ*, 586, 319
- Lee, C.-F., Hsu, M.-C., & Sahai, R. 2009, *ApJ*, 696, 1630
- López, R., Riera, A., Raga, A. C., et al. 1996, *MNRAS*, 282, 470
- Martín-Pintado, J., Bujarrabal, V., Bachiller, R., Gómez-González, J., & Planesas, P. 1988, *A&A*, 204, 242
- Mendoza, C. 1983, *Proc. IAU Symp. 103, Planetary Nebulae*, ed. D. Flower (Reidel: Dordrecht), 143
- Miranda, L. F., Blanco, M., Guerrero, M. A., & Riera, A. 2012, *MNRAS*, 421, 1661
- Montgomery, M. M. 2012, *ApJ*, 753, L27
- Morris, M. 1987, *PASP*, 99, 1115
- Nakashima, J.-I., Fong, D., Hasegawa, T., et al. 2007, *AJ*, 134, 2035
- Neri, R., García-Burillo, S., Guelin, M., et al. 1992, *A&A*, 262, 544
- Pardo, J. R., Cernicharo, J., Goicoechea, J. R., & Phillips, T. G. 2004, *ApJ*, 615, 495
- Raga, A. C., Navarro-González, R., & Villagrán-Muniz, M. 2000, *Rev. Mex. Astron. Astrofis.*, 36, 67

- Raga, A. C., de Gouveia Dal Pino, E. M., Noriega-Crespo, A., Mininni, P. D., & Velázquez, P. F. 2002, *A&A*, 392, 267
- Raga, A. C., Esquivel, A., Velázquez, P. F., et al. 2009, *ApJ*, 707, L6
- Reipurth, B., Raga, A. C., & Heathcote, S. 1992, *ApJ*, 392, 145
- Riera, A., Raga, A. C., Reipurth, B., et al. 2003, *AJ*, 126, 327
- Riera, A., Binette, L., & Raga, A. C. 2006, *A&A*, 455, 203
- Riera, A., Raga, A. C., Velázquez, P. F., et al. 2009, *Protostellar Jets in Context*, eds. K. Tsinganos et al. (Berlin: Springer-Verlag), *Ap&SS Proc. Ser.*, 603
- Riera, A., Raga, A. C., Velázquez, P. F., et al. 2011, *A&A*, 533, A118
- Sánchez Contreras, C., & Sahai, R. 2004, *ApJ*, 602, 960
- Sánchez Contreras, C., Sahai, R., & Gil de Paz, A. 2002, *ApJ*, 578, 269
- Sánchez Contreras, C., Bujarrabal, V., Castro-Carrizo, A., Alcolea, J., & Sargent, A. 2004, *ApJ*, 617, 1142
- Soker, N., & Rappaport, S. 2000, *ApJ*, 538, 241
- Soria-Ruiz, R., Bujarrabal, V., & Alcolea, J. 2013, *A&A*, 559, A45
- Tafoya, D., Loinard, L., Fonfría, J. P., et al. 2013, *A&A*, 556, A35
- Terquem, C., Eislöffel, J., Papaloizou, J. C. B., & Nelson, R. P. 1999, *ApJ*, 512, L131
- Trammell, S. R., & Goodrich, R. W. 2002, *ApJ*, 579, 688
- Trammell, S. R., Dinerstein, H. L., & Goodrich, R. W. 1993, *ApJ*, 402, 249
- van Leer, B. 1982, in *Proc. Numerical Methods in Fluid Dynamics*, ed. E. Kraus (Berlin: Springer), *Lect. Notes Phys.*, 507
- Velázquez, P. F., Riera, A., & Raga, A. C. 2004, *A&A*, 419, 991
- Velázquez P. F., Gómez Y., Esquivel A., & Raga A. C. 2007, *MNRAS*, 382, 1965
- Velázquez P. F., Steffen W., Raga A. C., et al. 2011, *ApJ*, 734, 57
- Velázquez, P. F., Raga, A. C., Riera, A., et al. 2012, *MNRAS*, 419, 3529
- Velázquez, P. F., Raga, A. C., Cantó, J., Schneiter, E. M., & Riera, A. 2013, *MNRAS*, 428, 1587
- Westerbrook, W. E., Willner, S. P., Merrill, K. M., et al. 1975, *ApJ*, 202, 407

Table 4.2: Proper motions of identified features.

Feature name	x ($''$)	y ($''$)	μ_x ($'' \text{ yr}^{-1}$)	μ_y ($'' \text{ yr}^{-1}$)	$\epsilon(\nu_x)$	$\epsilon(\nu_y)$	v_t (km s^{-1})	PA (deg)
E6	-0.07	-3.21	-0.0106	-0.0133	0.005	0.0025	81 ± 23	-38 ± 18
E5	-0.52	-4.03	-0.0003	-0.0130	0.002	0.002	62 ± 18	-1 ± 16
E1	-0.02	-6.54	0.0020	-0.0608	0.002	0.002	288 ± 18	2 ± 3
E11	0.25	-3.16	0.0126	-0.0180	0.002	0.002	105 ± 18	35 ± 10
E10	0.61	-3.88	0.0084	-0.0237	0.0024	0.0021	119 ± 17	20 ± 9
E9			0.0148	-0.0298	0.0023	0.0025	158 ± 18	26 ± 7
E9a	0.65	-4.32	0.0004	-0.0134	0.0021	0.0021	64 ± 17	2 ± 16
E9b	1.04	-4.32	0.0097	-0.0170	0.0021	0.0022	93 ± 18	30 ± 11
E9c	0.88	-4.83	0.0180	-0.0235	0.0023	0.0022	141 ± 19	37 ± 8
E8	1.67	-5.28	0.0197	-0.0477	0.0021	0.0021	245 ± 18	22 ± 4
E7	1.71	-6.35	0.0330	-0.0848	0.0022	0.0051	432 ± 27	21 ± 3
W5	0.52	2.96	0.0047	0.0139	0.0021	0.0026	70 ± 19	19 ± 14
W6	0.05	3.22	0.0112	0.0192	0.0025	0.0023	106 ± 18	30 ± 10
W4(b)	0.43	3.90	0.0091	0.0750	0.0025	0.0023	360 ± 18	7 ± 3
W3(a)	-0.47	3.85	-0.0141	0.0051	0.0385	0.0030	194 ± 21	-20 ± 8
W3(b)	-0.42	4.22	0.0065	0.0570	0.0030	0.0027	272 ± 19	6 ± 4
W2	-0.87	5.30	-0.0001	0.0171	0.0021	0.0026	81 ± 19	-0 ± 12
W1(a)	-0.65	6.10	0.0004	0.8150	0.0004	0.0028	387 ± 19	0 ± 3
W1(b)	-0.76	6.87	-0.0033	0.0790	0.0022	0.0022	374 ± 18	-2 ± 3
A ^a	-0.20	-1.50	-0.0008	-0.0001	0.0021	0.0021	4 ± 18	-89 ± 76
R1 ^b	-1.12	-2.53	-0.0010	-0.0177	0.0021	0.0023	84 ± 18	-3.4 ± 12
R2-E ^b	-0.54	-2.45	0.0012	-0.0141	0.0021	0.0021	67 ± 17	4.9 ± 15
R2-W ^b	-0.60	-2.78	0.0021	-0.0230	0.0021	0.0024	109 ± 18	5.4 ± 10
E lobe J1 ^c			0.0022	-0.0610	0.0021	0.0024	289.5 ± 18	2 ± 3
E lobe J2 ^c			0.0023	-0.0460	0.0023	0.0021	243.3 ± 14	26 ± 4
W lobe J1 ^c			0.0010	0.0257	0.0021	0.0022	122.1 ± 18	2 ± 8
W lobe J2 ^c			0.0014	0.0254	0.0021	0.0021	120.7 ± 17	3 ± 8

Notes The distances x and y are measured from the position of the central compact H II region. ^(a) Reference feature. ^(b) Ring-like structure seen in the innermost part of the east lobe. ^(c) The boxes used to measure the proper motion of the east and west lobes are shown in blue in Fig.4.6.

Análisis de una Serie Nebulosas Planetarias

Jets and Bow-shock features in Planetary Nebulae

A. Castrillón; A. Riera; R. Lopez and O. Aquines

To be submitted in 2021

5.1. Resumen de la publicación

En el presente artículo se analizan las microestructuras presentes en 9 nebulosas planetarias, que cumplen los requerimientos para su análisis. Una vez elegida la muestra se aplican las rutinas de trabajo con el fin de obtener el echellograma respectivo que indique la estructura de interés para posteriormente realizar el análisis wavelet, con el fin de establecer los máximos locales en las estructuras de interés, una vez determinados estos máximos, podemos visualizar si existen patrones de ubicación en sus máximos y así poder determinar si existen zonas que permitan identificar el tipo de estructura (Knots, jets, jet-like, filamentos, lobes) presente en la nebulosa planetaria.

Posteriormente, se obtienen los cocientes $[\text{O III}]/H\alpha$ y $[\text{N II}]/H\alpha$, con estos cocientes podemos establecer zonas de estratificación a través de los diagramas diagnósticos, determinando así zonas estratificadas que indiquen la presencia de microestructuras.

Una vez confirmada la presencia de microestructuras, se realiza un análisis unidimensional en cada uno de los filtros determinado así la posición de la microestructura medida al largo del eje que conecta la estrella central de la nebulosa planetaria con la microestructura hallada. [Castrillón, et al., (2021)] [7].

5.2. Introduction

Planetary nebulae (PNe) represent the final phases of the stellar evolution of low- and intermediate-mass stars and consist of the stellar material ejected by a star with initial mass $\leq 1 - 8 M_{\odot}$. As such a star evolves off the asymptotic giant branch (AGB), its copious mass loss strips off the stellar envelope and exposes the hot stellar core. The subsequent fast stellar wind (1000 - 4000 km s⁻¹) sweeps up the slow AGB wind to form a PNe (Kwok et al. 1978).

The formation of PNe has been a topic of research for many years, in those studies, regardless a variety of mass ejection mechanisms located, including instabilities induced by the recombination (Roxburgh 1967; Lucy 1967), radiation pressure (Faulkner 1970; Finzi & Wolf 1971), relaxation in the oscillations of the shell due to the thermal instabilities in the nucleus (Smith & Rose 1972), pulsational instabilities (Kutter & Sparks 1974; Wood 1974; Tuchman et al. 1979) and thermal pulses (Härm & Schwarzschild 1975; Trimble & Sackmann 1978). Although all these ejection mechanisms are interesting, none of them successfully explain the correct amount of mass ejected. The existence of a binary system inside these objects has been proposed as a mechanism to generate multilobe morphologies in PN, as originally suggested by Bond, Liller & Mannery (1978). This idea is supported by the increasing number of binary systems found inside bipolar and multipolar PN (Velázquez et al, 2012). As a result, collimated fast winds (CWF) or jets have been proposed to operate during the post-AGB phase and be the primary agents for the shaping of Planetary Nebulae (PNe) (see, e.g., Balick & Frank 2002).

But the shape of a PN is thought to be determined by the interaction between the fast and tenuous stellar winds (e.g., Patriarchi & Perinotto 1991). Fast winds of its central star collide with the previous slow, dense wind of its asymptotic giant branch (AGB) phase. In the so-called interacting stellar winds (ISW) model of PN formation (Kwok et al. 1978), the critical parameter is the density distribution of the AGB wind (Balick 1987): a spherical symmetric AGB wind will result in a spherical PN, while a polar density gradient in the AGB wind will result in an elliptical or bipolar PN, depending on the degree of the density gradient. (Guerrero et. al, 2008)

A simplified classification of the morphology of these features shows small-scale features, collimated bipolar outflows and point symmetric morphologies, including multiple point-symmetric bubbles. This classification is based on optical imaging and ground-based spec-

Table 5.1: Features list of the sample of Planetary nebula

Object	RA(J2000) (^h ^m ^s)	Dec(J2000) (^o ' ")	Narrow Band Filters	d (kpc)	c(H β)	V _r (FLiERs) (km s ⁻¹)	References
NGC 3918	11 50 17.89	-57 10 56.64	H α , [N II], [O III]	1.639	0.40	-25, 24 ⁽¹⁾	1,2,3,4
IC 4593	16 11 44.59	12 4 17.14	H α , [N II], [O III]	2.4	0.17	10.8 ⁽¹⁾ , -5	5,2,4,6
NGC 6210	16 44 29.48	23 47 59.08	H α , [N II], [O III]	1.6	0.14	24.3 ⁽¹⁾	1,7,8,4
IC 4634	17 01 33.43	-21 49 29.41	H α , [N II], [O III]	1.3	0.34	14.1 ⁽¹⁾ , ± 20	9,10,4
NGC 6543	17 58 33.29	66 37 58.63	H α , [N II], [O III]	1.625	0.10	19.3 ⁽¹⁾ , 46 ⁽³⁾	9,11,4,12
NGC 7009	21 04 10.80	-11 21 46.53	H α , [N II], [O III]	1.154	0.16	19.5 ⁽¹⁾ , $\pm 5,5$	9,13,4,14,15
M 3-1	07 02 49.9	-31 35 29.45	H α , [N II]	6,868	0.24		9,16
Hb 4	17 41 52.7	-24 42 08.34	H α , [N II]	2.297	1.81	21.5 ⁽¹⁾	9,17,18
NGC 7354	22 40 19.73	61 17 29.45	[N II], [O III]	2.022	2.02	$\simeq -5$	9,19

Notes ⁽¹⁾ V_{exp}=expansion velocity ⁽³⁾ V_{exp} FF'= Velocity of structure FF'

(1) Stanghellini & Shaw (2008); (2) Robertson–Tessi & Garnett (2005);(3) Corradi et al. (1999);(4) Tylanda & Stasinska (1994);(5) Toalá et al. (2020);(6) Corradi et al. (1997);(7) Pottasch, Bernard–Salas and Roelling (2009); (8) Liu et al. (2004);(9) Bown, A.G.A., Vallenari, A., et al. (2018), GAIA Collaboration; (10) Guerrero et al. (2008); (11) Wesson & Liu (2004);(12) Miranda & Solf (1992);(13) Goncalves et al. (2003);(14) Reay & Atherton (1985);(15) Fernández, Schwarz & Monteiro (2004); (16) Girard et al. (2007);(17) Peña et al. (2001);(18) López, Steffen & Meaburn (1997);(19) Contreras et al. (2010).

troscopy, individual authors, but similar works added a particular name or defined a new subclass to the group, for example FLIERs by Balick, LIS by Goncalves, BRETs by Lopez, and others.

Balick and coworkers introduced the Fast Low Ionization Emission Regions (FLIERs) class, which are low-ionization knots of small sizes ($\sim 10^{16}$ cm) that come in pairs on opposite sides of the central star, and show more significant Doppler shifts than the more slowly expanding gas of the shells (Balick et al. 1993, 1994). These change to this low-ionization structures appear in the shape of knots, collimated strings, or filaments (see, e.g., Corradi et al. 1996). A subclass of point-symmetric features related to precessing or rotating bipolar outflows (BRETs) was introduced by López et al. (1993) (see also López 2000, 2002).

Goncalves et al. (2001, 2004) introduced the acronym LIS (Low Ionization Structures) and three subclasses: pair of knots, jets and jet-like structures. Goncalves et al. defined the jets as highly collimated features extended in the radial direction to the central star, which appear in opposite symmetrical pairs and shows more significant Doppler shifts than those of the main shell. LIS with a jet appearance and moving at low radial velocities are classified as jet-like features. Obviously, due to projection effects, jets can appear as jet-like features. Miszalski et al. (2009) has introduced a new description of the low ionization structures. Miszalski et al. described knots as unresolved LIS with an aspect ratio of unity, filaments as knots with an aspect ratio larger than unity, and jets are opposing bipolar outflows located well outside of the main nebula.

With the launch of the *Hubble Space Telescope* (HST), images with high angular resolution ($\leq 0''.1$) arrived. Such images revealed that most PNe show aspherical morphologies with a wide range of geometric shapes, with a significant fraction having collimated bipolar or multipolar lobes (Sahai & Trauger 1998). Therefore, we analyze the physical properties and morphology from a group of PNe to determine the structure of the small-scale features (knots, filaments and jets) and excitation conditions associated to mature PNe. To accomplish this, we use a group of images from HST in filters [O III], [N II] and $H\alpha$.

We present the ratios [O III]/ $H\alpha$ and [N II]/ $H\alpha$ and diagnostic diagrams [O III]/ $H\alpha$ vs. [N II]/ $H\alpha$ to determine excitation collisional conditions to locate the shock and to get different characteristics sizes in the different structures of our sample.

The paper is organized as follows. In Sect. 5.3, we present the data sample, observations, and data reduction. In Sect. 5.4 explain the analysis techniques (anisotropic wavelet analy-

sis, emission line ratios and diagnostic diagrams). In Sect. 5.5 we present the result for individual objects. Finally, we present the global results and conclusions in Sect. 5.6.

5.3. Narrowband images of FLIERS in PNe

5.3.1. Data Sample

Figure 5.1 shows the HST [N II] images of the PNe (except for NGC 6210 for which the HST [O III] image is shown, see below). The selected features, indicated by arrows, are prominent in the [N II] images, except the bow-shock part seen in NGC 6210, which is more prominent in the [O III] emission line. These features are low-ionization structures of small sizes with respect to the nebula's main body. These features appear in double pairs at symmetrical distances from the central source. Following the terminology introduced in the literature, the low-ionization structures observed in these PNe can be described as knots (small sizes, such as the outermost knots of IC 4593) and filaments or jet-like pairs (i.e., such as the filamentary features of NGC 6543 and the outer features seen in NGC 6543). Jets may show a leading bow-shock similar to the HH jets head where the outflows slams into the surrounding medium (such as the outermost features seen in IC 4634 and NGC 3918) (Corradi et al. 1999). Jets, ansae, knots and filaments of small scales are present in NGC 7009. (Steffen et al. 2009)

Table 5.2: [O III]/H α type, shape and micro-structures

Common name	[O III]/H α Class*	Nebular shape	Comments	Ref.
NGC 3918	AB	E, MS	PS outflows	1, 5
IC 4593	AB	MS	PS outflows	1, 2
NGC 6210	A	PS, MS	PS outflows	1, 2, 6
IC 4634	A	MS	PS outflows	1, 2
NGC 6543	AB	E, MS	PS outflows	1, 7
NGC 7009	AB	E, MS'	FLIERS	1, 2

* for more detail see Guerrero et al. 2013 table 2.

(1) Frew (2008); (2) Kwitter & Henry (1998); (5) Ercolano et al. (2003); (6) Pottasch et al. (2009); (7) Wesson & Liu (2004).

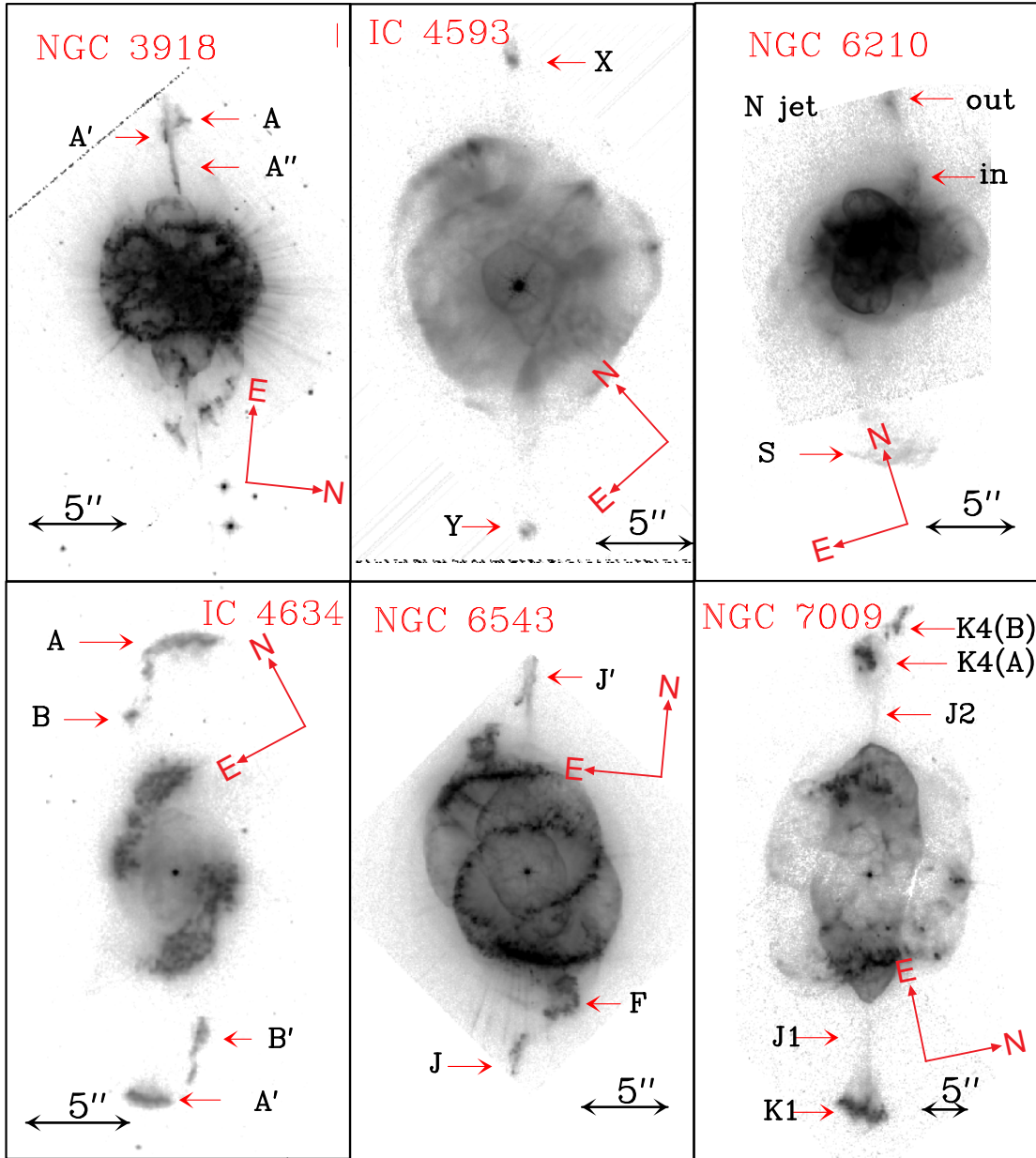


Figure 5.1: HST [N II] narrow-band images of the PNe of the sample (except [O III] image of NGC 6210, see text). The low-ionization features (LIS) selected for this work are NGC 3918, IC 4593, NGC 6210, IC 4634, NGC 6543 and NGC 7009. The micro-structure features are indicated by arrows

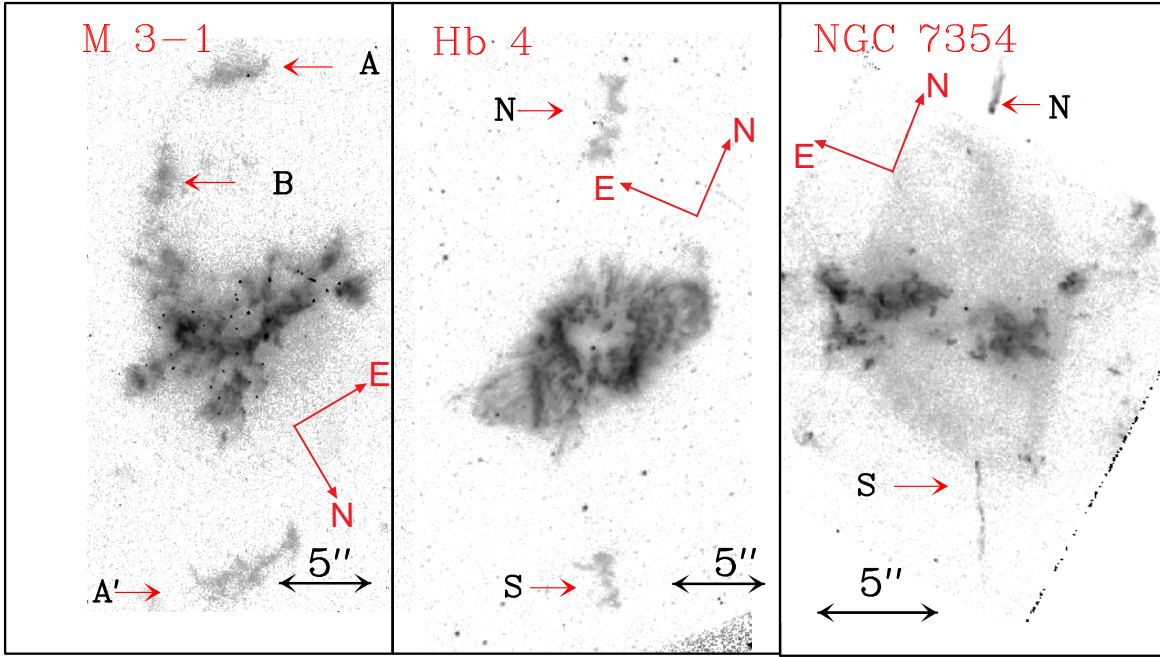


Figure 5.2: Additional objects. HST narrowband images [N II] images of the PNe M 3-1, Hb 4 and NGC 7354. The images have been rotated so that the symmetry axis lay parallel to the y -axis. The selected low-ionization features are marked by arrows.

The selected PNe are listed in Table 5.1, where we present several properties: RA, Dec, filters, d , $c(H\beta)$ is the reddening coefficient, and V_r is the radial velocity measures respect to central star of the planetary nebula.

In the table 5.2. we provide the classification of each PN and relevant information: the common name, the class or type of structure observed in $[O III]/H\alpha$ ratio maps, the morphology or nebular shape (E=elliptical, MS=multiple shell, PS=point-symmetric), and comments on the presence of collimated point-symmetric outflows or FLIERs. Most of the data in this table have been obtained from Frew(2008). We see three types of PNe, type A, type B or type AB in this sample. These types of nebulae are characterized by:

Type A PNe that present caps of enhanced $[O III]/H\alpha$ ratios at the tip of jet-like features. These bright $[O III]$ emission regions can be interpreted as bow-shock features produced by fast collimated outflows. The PNe type A are PNe NGC 3918, IC 4593, NGC 6210, IC 4634, NGC 6543 and NGC 7009.

Type B PNe surrounded by skins of enhanced $[O III]/H\alpha$ emission associated with nebular shells. In some double-shell PNe, both shells exhibit a skin of enhanced $[O III]/H\alpha$. The PNe type B are NGC 3918, IC 4593, NGC 6543 and NGC 7009. (Guerrero et al. 2013)

5.3.2. Observations and Data reduction

The selected survey searched for narrow-band images in filters F656N, F658N and F502N coeval WFPC2 images in the Hubble Legacy Archive/MAST of PNe with FLIERs. For this analysis, we obtain the survey reduced from HST archive and follow calibrated photometrically and rotated.

The F656N image is usually called the $H\alpha$ image, while the F658N is attributed to $[N II]$ emission at the wavelength 6583 Å. Note that the F656N filter includes contribution of both $[N II]$ 6548, 6583 Å emission lines, with filter transmissions relative to $H\alpha$ of Guerrero et al. consider a 38 % (33 % and 5 % respectively for both lines of $[N II]$) (Guerrero et al. 2013). The F502N filter is attributed to $[O III]$ 5007 Å.

The analysis started with the pipeline reduced data products as provided by the MAST archive. The absolute astrometry as returned by the pipeline reduction has a typical positional uncertainty of $\sim 0''.2$. To improve the relative astrometry of the images in the different filters, we identified common field stars in all filters. The images were aligned and rotated using the standard IRAF¹ routines 'geomap' and 'geotran'. The accuracy of the relative alignment between the different filters are approximately 0.5 pixels (i.e. $\leq 0''.03$). The images were then rotated so that the symmetry axis lay parallel to the y-axis.

5.4. Analysis

We intend to characterize the morphology to small-scale and to identify the regions with shocks in the complex structures of FLIERs and to introduce a new analysis to complement other similar studies for some objects NGC 3918 Corradi et al. 1999; IC 4593, NGC 3918 Gonçalves et al. 2000; IC 4634 Raga et al. 2008, A&A, 489, 1141; NGC 7009 Gonçalves et al. 2003; Hb 4 Hajian et al. 1997; NGC 6543 Balick 2004.

We present a sistematic study of a homogeneous survey of 9 PNe (type A, B and AB) from HST archive the using same filters ($H\alpha$, $[N II]$ and $[O III]$) and same spatial resolution for all survey and we study morphology for small-scale using the anisotropic wavelet analysis, this kind of research is not present in the previous studies.

¹IRAF is distributed by the National Optical Astronomy Observatories which is operated by the Association of Universities for Research in Astronomy, Inc. (AURA) under cooperative agreement with the National Science Foundation.

5.4.1. Anisotropic wavelet analysis

The wavelet transform decomposes an image into maps of different scales. In each map, structures with the chosen scales are prominent because they have higher coefficients than those with smaller or larger scales. In this paper, we are interested in studying and identifying the characteristics of complex spatial structures and the small-scale morphology of FLIERs (LIS), of a group of PNe. To reach this goal, we carried out an analysis based on wavelet transform. This analysis allows us to obtain a description of complex structures without losing of positional information.

Wavelet transforms have been used in different astrophysical contexts. For example, Grosdidier et al. (2001) used two-dimensional wavelets to isolate stochastic structures of different characteristic sizes in M 1-67 from its $H\alpha$ image; Riera et al. (2003) studied the complex spatial structure of knots in HH 110 using the wavelet technique.

In 2014, Riera et al. (2014) used the wavelet technique to study the multipolar jets of the pPN CRL 618 and to study of the characteristic sizes of knots along CRL 618. Therefore, we adopt the procedure developed by Riera et al. (2014). This study shares many similarities with our analysis.

We have rotated all images so that the symmetry axis is parallel to the ordinate. On these rotated images, we then carry out a decomposition in a basis of anisotropic wavelets, which have different sizes along and across the radial direction. We choose and have used a basis of “Mexican hat” (equation 5.1) wavelets of the form

$$g(r) = C(2 - r^2)e^{-r^2/2}, \quad (5.1)$$

where $r = [(x/a_x)^2 + (y/a_y)^2]^{1/2}$, $C = (a_x^2 + a_y^2)^{-1/2}$, and a_x and a_y are the spatial scale lengths of the wavelet along the x - and y -axis respectively. Following Riera et al. (2014) we choose a range for a_x and a_y , which are taken to have integer values of pixels (from 1 to 60 pixels, i.e. from $0''.045$ to $2''.70$) and we then compute the convolutions

$$T_{a_x, a_y}(x, y) = \int \int I(x', y') g(r') dx' dy' \quad (5.2)$$

where $r' = [(x' - x)/a_x]^2 + [(y' - y)/a_y]^2]^{1/2}$, and $I(x, y)$ is the observed emission map as a function of position (x, y) . These convolutions are calculated with a standard FFT algorithm.

We compute the transform maps $T_{a_x, a_y}(x, y)$ (equation 5.2) for the $H\alpha$, [N II] and [O III]

images for each of the selected regions. The convolved maps have been used as follows. First, on the observed intensity map we fixed the position of y and found the values of the position x_k of the knots, which correspond to intensity maxima across the jet axis. For each pair (x_k, y) where the $I(x_k, y)$ has a maximum, we determine $(a_{x,k}, a_{y,k})$ in the a_x and a_y -space where the wavelet transform has a local maximum. In this way, we detect the characteristic size of a feature with an intensity maximum at (x_k, y) .

$$\langle a_x \rangle = \frac{\sum_k a_{x,k} T_{a_{x,k}, a_{y,k}}(x_k, y)}{\sum_k T_{a_{x,k}, a_{y,k}}(x_k, y)} \quad (5.3)$$

The results obtained with the wavelet analysis are shown in figures 5.3, 5.7, 5.13, 5.18, 5.25, 5.26, 5.35 and 5.37. They represent the contour plots in the lines [N II] 6583 Å (top panels, color red), [O III] 5007 Å (middle panels, color green) and H α (bottom panels, blue color) for NGC 3918, IC 4593, NGC 6210, IC 4634, NGC 6543 and NGC 7009. All images were rotated in order to align the axis of symmetry and we represented the position of the peaks x_k for each y are shown for $k = 1, 2$ and 3 for the three images ($k=1$ (first column), $k=2$ (second column) and $k=3$ (third column)) which give an estimate of the characteristic sizes across and along the polar axis. Also shown (as error bars) are the values of $(a_{x,k}, a_{y,k})$ corresponding to each peak. Note the three maxima lay along the low-ionization structures. To quantify the observed broadening of the structure, for each position y we compute the weighted mean of the x -spatial scale (perpendicular to outflow axis). In equation 5.3, $\langle a_x \rangle$ shows as a function of position y along the PNe flow, where y is relative distance to the central star (Riera et al. 2003).

Therefore we obtained the weighted mean of the x - and y -spatial scales as a function relative to the position (offsets) of the central star along the y -axis, which are shown in figures 5.4, 5.8, 5.9, 5.14, 5.19, 5.20, 5.27, 5.28, 5.36, 5.38, 5.43, 5.44, 5.45 and 5.46.

5.4.2. Emission line ratios

In this study, we search the physical conditions from the emission line ratios in all structures from survey, in all cases we got three filters and two filters to additional objects.

“The propagation of a shock wave into a medium is expected to heat the material beyond the shocks of fast moving producing appreciable effects in intensity line ratios such as [O III]/H α with this ratio we search the regions where it is enhanced. In the regions with enhanced [O III]/H α can be ascribed to two different types of morphological structures: bow-shock structures produced by fast collimated outflows and thin skins enveloping

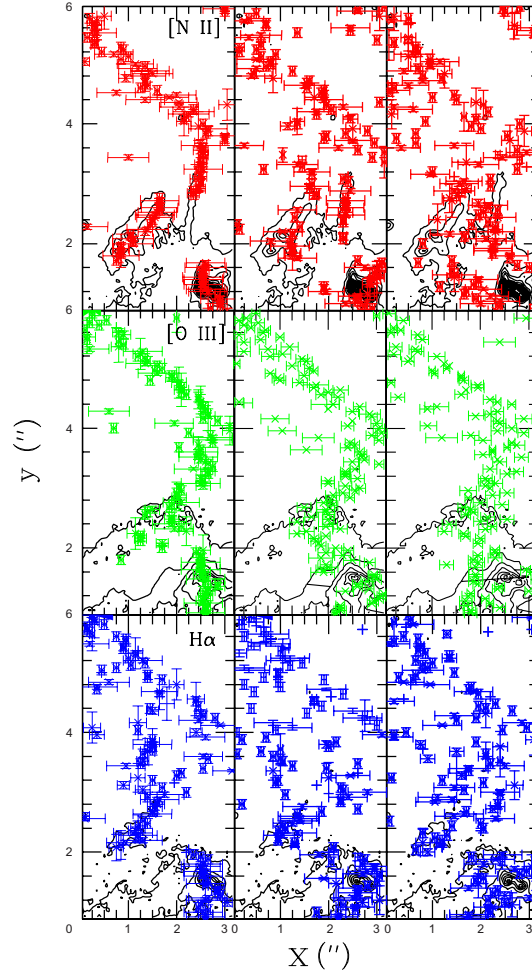


Figure 5.3: Contour plots in zones A, A' and A'' to NGC 3918 in different emission lines, where we show the positions (x_k, y) of the maxima. The characteristic sizes $(a_{x,k}, a_{y,k})$ are shown as errorbars. Where $k = 1, 2, 3$, represent a local maximum on the intensity map. See text for more details. [N II] (top panels, color red), [O III] (middle panels, color green) and H α (bottom panels, color blue) of the

expanding nebular shells. Both collimated outflows and expanding shells are therefore confirmed to generate shocks in PNe. We also find regions with depressed values of the [O III]/H α ratio, which are found mostly around density bounded PNe, where the local contribution of [N II] emission into the F656N H α filter cannot be neglected.” (For more detail see Guerrero et al, 2013.)

For each PNe, we have computed the [O III]/H α , [N II]/H α and some cases [O III]/[N II] ratio maps (fig. 5.5, 5.10, 5.15, 5.21, 5.29, 5.32 and 5.39). These ratio maps were dereddened using the logarithmic reddening constant $c(H\beta)$ listed in table 5.1 and the Cardelli et al. (1989) extinction law. The [O III]/H α (the H α image include the 25 % of the [N II] 6583

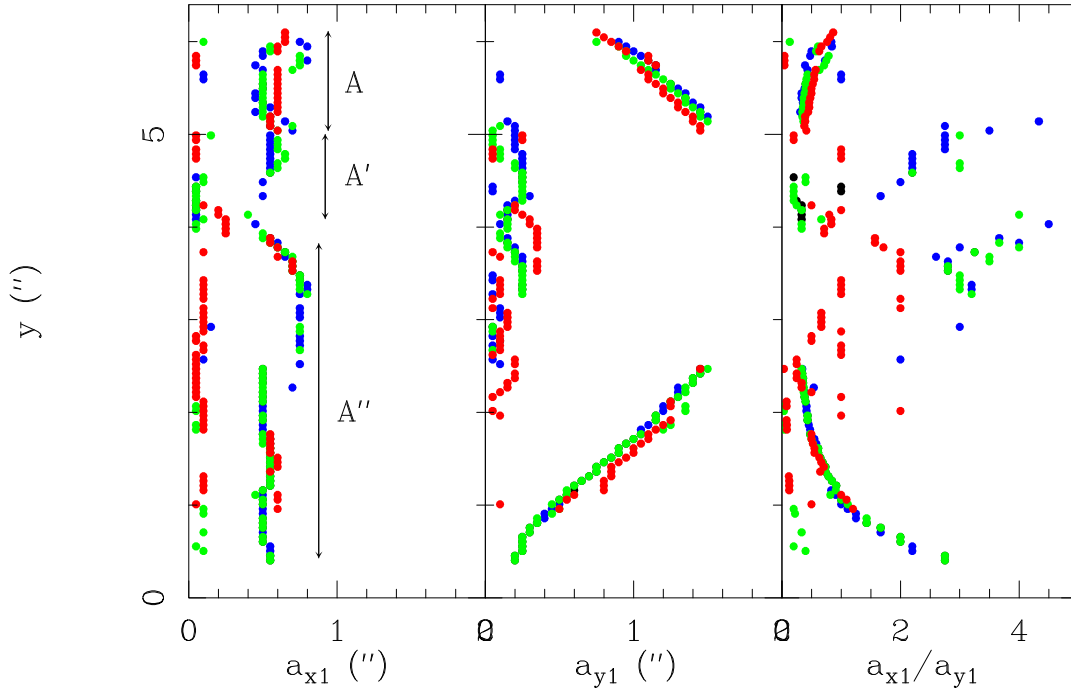


Figure 5.4: Wavelet analysis in NGC 3918 to A, A' and A'' features. Average $\langle a_x \rangle$ (left), $\langle a_y \rangle$ (middle), and the $\langle a_x \rangle / \langle a_y \rangle$ (right) ratio plotted as a function of relative distance to the central star (offsets). Blue circles correspond to H α , green circles correspond to [O III] 5007 Å, and red circles correspond to [N II] 6584 Å.

Å) and [N II]/H α ratios trace the excitation conditions across the FLIERs (Guerrero et al, 2013).

In the figs. 5.6, 5.11, 5.16, 5.22, 5.30, 5.33 and 5.40 we present diagnostic diagrams, involving emission-line ratios commonly used to discriminate photoionized nebulae from shock-excited objects. For this diagrams we use different box size, this depend of size of structure (64x128, 81x131, 111x101, 131x101, 51x84, 154x114 and 176x112 pixels) in each point indicate one value of intensity of pixel to pixel from ratios of [O III]/H α vs. [N II]/H α for each structure of survey.

Finally, we show the [N II], H α and [O III] intensity distribution in the figs. 5.12, 5.17, 5.23, 5.24, 5.31, 5.34, 5.41 the intensity over the cross section in the different regions of our PNe. We consider the Intensity vs. spatial resolution in arcsec and see the bow shock location in the different structures present in this study. The location of the slit is on a vertical axis that passes through the center of the structure (jet, Knot, filament. etc)

5.5. Individual Objects

5.5.1. NGC 3918

NGC 3918 has a complex morphology as shown by the [N II] WFPC2/HST image (figure 5.1). It has a bright inner elliptical shell with two fainter protrusions extending in the E-W direction (up/down in this study, where the image has been rotated to have the symmetry axis along the vertical axis). The inner shell is surrounded by an elliptical outer shell, which is more prominent in the [N II] emission line. The outer shell shows a network of filaments and clumps in the [N II] image. The HST images show that the outer shell also possesses faint protrusions. In addition, the nebula shows several radial filaments (prominent in the [N II] emission line, which point towards the central star.

NGC 3918 has several low-ionization structures along the inner shell's major axis. It has a thin eastern (up) jet extending out of the inner shell along its major axis. This jet/filament (feature A in Corradi et al. 1999) has two condensations at its edge that were named A' and A'' by Corradi et al. (1999), also shown in figure 5.1. On the opposite (Western/down) side of the central star there are several condensations lying at the edge of the outermost protrusion and a faint thin jet only detected in [N II]. The bright knots in the western side seem to be condensations of the outermost protrusions, and therefore are not described in the following analysis. The radial velocities along the eastern jet/filament increase linearly with the distance to the central star, with deprojected velocities from 50 to 100 km s⁻¹ (Corradi et al. 1999). We have adopted a distance 1.639 Kpc (Stanghellini and Shaw, 2008).

The results obtained from the wavelet analysis of the jet (termed A, A' and A'' in figure 5.1) are shown in figure 5.4. The characteristic sizes across the jet axis at the inner edge of A'' is $\sim 0.''5$ (i.e., 9×10^{15} cm) in [O III], H α and [N II]. At larger distances along feature A, the spatial scale $a_{x,1}$ suddenly decreases in the [N II] emission line to values $\sim 0.''1$ (i.e., 2.0×10^{15} cm, almost unresolved at the present spatial resolution), while the jet broadens in [O III] and H α (up to $0.''8$). The bright knot A' has small spatial size across the jet axis with $a_{x,1} \sim 0.''1$ (i.e., $\leq 2.0 \times 10^{15}$ cm). At further distances, the width of the jet broadens at the knot A, which shows $a_{x,1} \sim 0.''4$ to $0.''6$ in all emission lines. At the inner edge of the jet (i.e., at feature A'') the elongation $a_{y,1}$ linearly increases with the distance to the central source giving an aspect ratio $a_{x,1}/a_{y,1}$ that decreases from 2 to 0.5. At the outer edge of A'' and at the knot A' we see a transition from elongated structures to transversal

structures, where the aspect ratio $a_{x,1}/a_{y,1}$ range from 1 to 4. At the outermost knot (A) the characteristic sizes along the jet axis decreases with distance to the central source. The jet of NGC 3918 in the figure 5.5 shows large $[\text{N II}]/\text{H}\alpha$ (right panel) ratio values, which change from A to A'. At the feature A this ratio ranges from 0.5 to 1.5. Larger values are detected in A' with a mean value of 2.4. The largest values are detected in A'' where the $[\text{N II}]/\text{H}\alpha$ ratio show values in the range 2 to 3, while in the left panel show $[\text{O III}]/\text{H}\alpha$ for A structure ratio ranges from 1.0 to 1.25 and the visibles zones for A'' the ranges from 1.48 to 1.90.

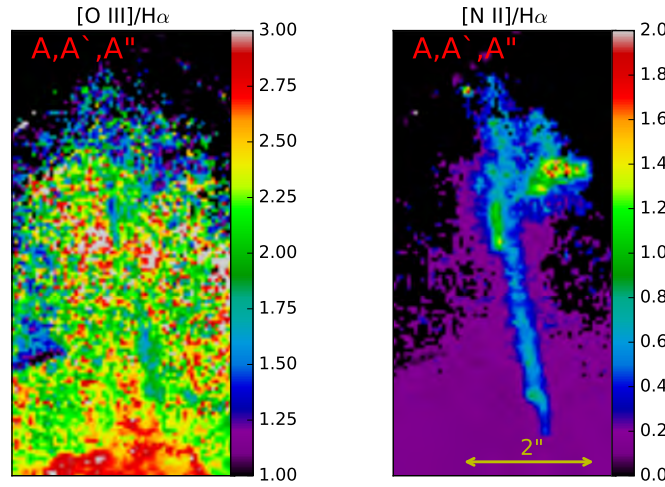


Figure 5.5: $[\text{O III}]/\text{H}\alpha$ (left panel) and $[\text{N II}]/\text{H}\alpha$ (right panel) ratio maps of the feature jet/filament in A, A' and A''. The structure is more clear in $[\text{N II}]/\text{H}\alpha$ of NGC 3918.

The figures 5.6 show the diagnostic diagram in the jet/filament A, A' and A'' having values for $[\text{N II}]/\text{H}\alpha$ between 0.1 and 1.0 while for $[\text{O III}]/\text{H}\alpha$ present values of 1.0 and 3.1.

5.5.2. IC 4593

IC 4593 is an elliptical PN with a complex system of shells and condensations. It has two ansae (i.e., low-ionization knots) at $\pm 12''$ from the central (variable) star, an outer faint halo and a number of condensations extending well beyond the bright central nebula forming a loop outside the asymmetric shell (Bohigas & Olguin 1996, Corradi et al. 1997, O'Connor et al. 1999). The distance adopted of 2.4 kpc (Toala et al. 2020).

The low-ionization knots (A and B in Corradi et al. (1997) and X and Y in O'Connor et al. (1999)) are seen as two bullets emerging from the main body of the nebula. Also, trails of material are seen connecting the bullets with the inner shell. The trails, which

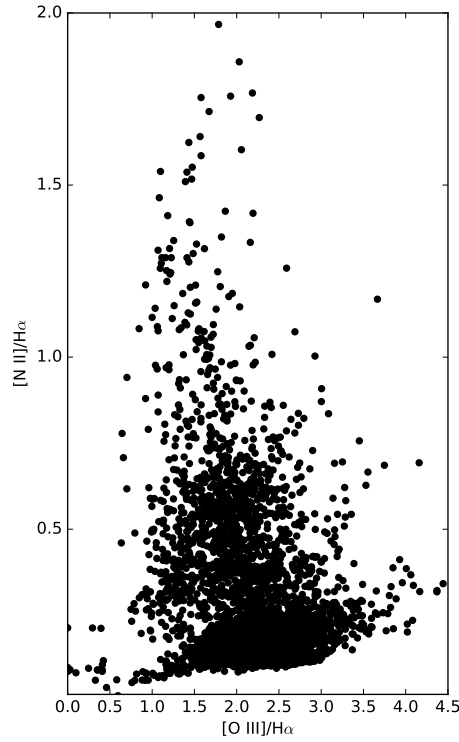


Figure 5.6: $[\text{O III}]/\text{H}\alpha$ vs. $[\text{N II}]/\text{H}\alpha$ diagnostic diagrams of morphological component (A, A' and A'') of NGC 3918. The size of the box is 64 x 128 pixels.

are brighter in $\text{H}\alpha$ and $[\text{O III}]$ images, show a conical structure that is wide at the base and narrows to an apex moving away from the central source. The conical structures have been described as jets or jet-like features (Goncalves et al. 2002).

The results obtained from the wavelet analysis of the knot X are shown in figure 5.7. Note that the three maxima are all found on the trial/jet axis. We have computed the weighed mean of the x - and y -spatial scales (i.e. $\langle a_x \rangle$, $\langle a_y \rangle$), which are shown in figures 5.8 and 5.9 as a function of relative distance to the central source. The two conical structures observed in the $\text{H}\alpha$ and $[\text{O III}]$ emission line images show a constant width of $0.6''$ (i.e., 2×10^{16} cm) in knot Y and it slightly decreases with distance to the central source in knot X (from $0''.4$ to $0''.2$ along $3''$). The elongation of the conical features ($\langle a_y \rangle$) linearly increases from the innermost region up to the apex (up to $1''.2$ or 4.3×10^{16} cm). Consequently, the aspect ratio (i.e. the $\langle a_x \rangle / \langle a_y \rangle$ ratio) rapidly decreases along the conical feature reaching a value of ~ 0.5 at both apex.

The outer knots appear as compact structures in the maps of $\text{H}\alpha$ and $[\text{N II}]$. These features are narrower in $[\text{N II}]$ than in $\text{H}\alpha$, with widths of $\sim 0''.1$ ($\leq 4 \times 10^{15}$ cm, almost unresolved

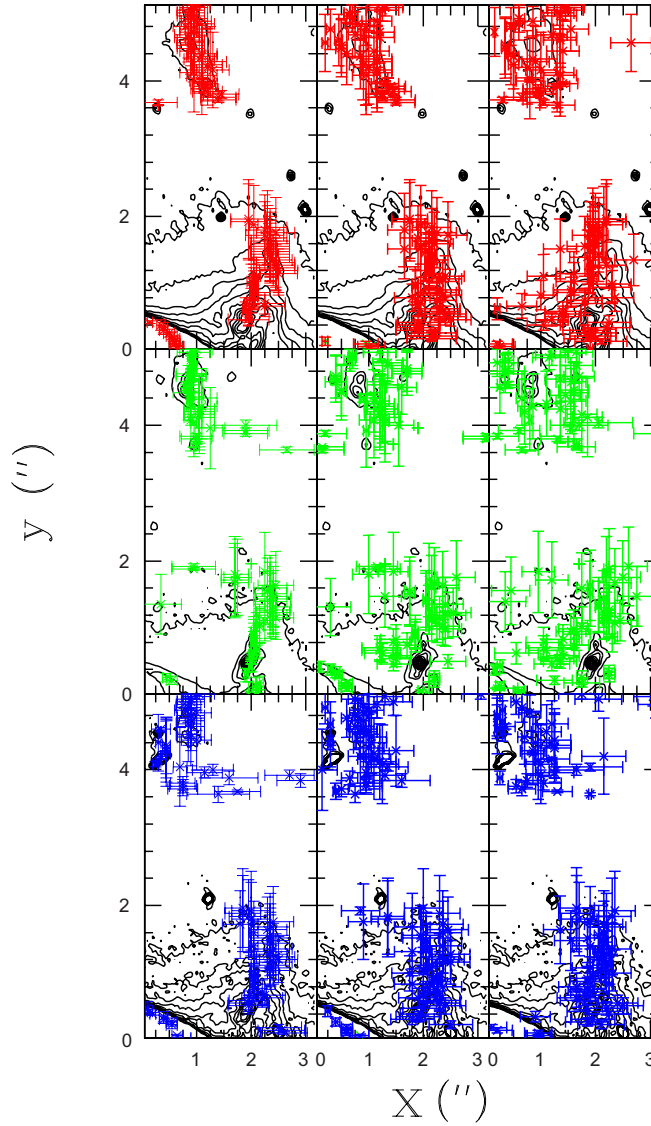


Figure 5.7: Contour plots of the knot X of IC 4593 where we show the positions (x_k, y) of the maxima. The characteristic sizes $((a_{x,k}, a_{y,k}))$ are shown as errorbars. The [N II] (top panels, red), [O III] (middle panel, greens) and the $H\alpha$ (bottom panels, blue)

at the present angular resolution).

The [N II]/ $H\alpha$ and [O III]/ $H\alpha$ emission line ratios of knots X and Y are shown in figure 5.10. The [O III] emission line is faint at both knots, where the [O III]/ $H\alpha$ ratio is almost constant with a mean value of ~ 0.35 . The [N II]/ $H\alpha$ emission line ratio show sudden variations over short distances across the knots. At the edge of knot X facing away from the central star the [N II]/ $H\alpha$ emission line ratio increases up to values $\sim 0.6 - 0.7$, while a value of 0.3 is observed behind (in the region towards the central star). Similar

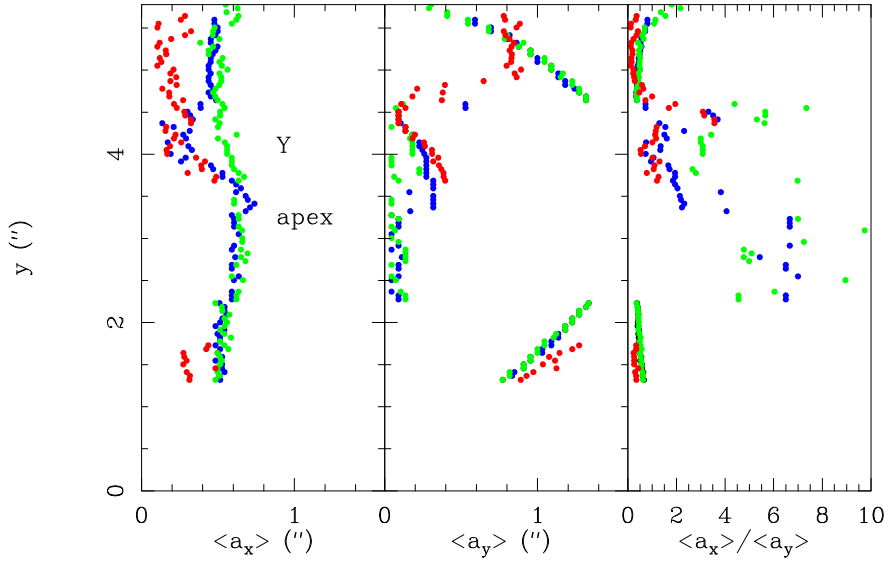


Figure 5.8: Wavelet analysis for knot Y of IC 4593. Symbols as in Figure 5.4. See text for more details.

values are observed in the $[\text{N II}]/\text{H}\alpha$ map of knot Y, where we see a central region with a mean value of 0.5 surrounded by a region of lower $[\text{N II}]/\text{H}\alpha$ ratio (~ 0.30). The conical trails are not detected in the $[\text{N II}]$ emission line, and have a $[\text{O III}]/\text{H}\alpha$ ratio ~ 1 . to 1.5. The relation between $[\text{O III}]/\text{H}\alpha$ vs. $[\text{N II}]/\text{H}\alpha$ for the knots X and Y for IC 4593 appear in the figure 5.11, we can see the behavior is very similar to IC 4634, the X structure present values between 0.4 to 0.7 in $[\text{O III}]/\text{H}\alpha$ while in $[\text{N II}]/\text{H}\alpha$ the range is 0.0 to 0.6 and Y structure present values 0.6 to 0.8 in $[\text{O III}]$ and 0.05 to 0.8 in $[\text{N II}]$ but the structure is more elongated with respect to X and the total points is less than in the fig 5.22, because the poor angular resolution ($\sim \pm 12''$).

The figure 5.12 shows the $[\text{O III}]$, $\text{H}\alpha$, $[\text{N II}]$ intensity distribution over the cross section of the X, Y knots, is almost symmetrical respect to central source (our offset), we see the position of the X peak in $\sim 11''.6$ and Y peak $\sim 12''.7$. This graph reveals the apparent spatial separation between the different lines, but for $\text{H}\alpha$, $[\text{N II}]$ we observe similar spatial distribution while for the $[\text{O III}]$ intensity maximum in $\sim 0''.10$ towards the west and east respectively for both structures (X, Y) respect to $\text{H}\alpha$ peak.

5.5.3. NGC 6210

NGC 6210 is an irregular PN located at an unusually high latitude. The brightest central part of the nebula shows small scale structure with the brightest part towards the N of the

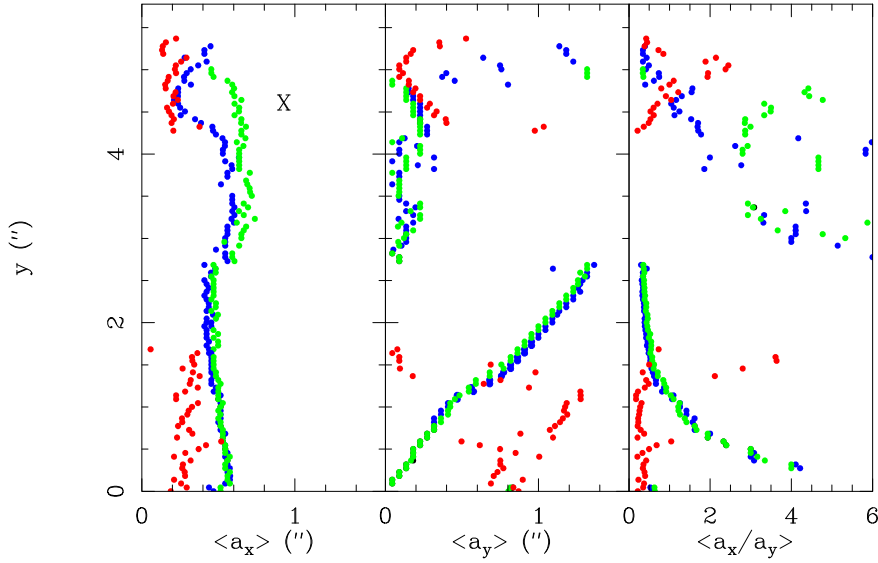


Figure 5.9: Wavelet analysis for knot X of IC 4593. Symbols as in figure 5.4. See text for more details.

central star (see Figure 1 in Pottasch, Bernard-Salas and Roeling 2009). The bright core is surrounded by a fainter nebula, containing a pair of ansae (i.e., FLIERs) on opposing sides (at $12''$ N and S of the nucleus) (Figure 5.1). An expansion distance of (1.6 ± 0.4) kpc was determined by Hajian, Terzian and Bignell (1995) and confirmed by Pottasch, Bernard-Salas and Roelling (2009).

The results obtained from the wavelet analysis of NGC 6210 are shown in figures 5.13 and 5.14. The southern FLIER is very faint in $[\text{N II}]$ and $\text{H}\alpha$ and, therefore, has not been analyzed. The northern FLIER shows an inner feature with a jet-like morphology and an outermost knot. In the following, we describe the morphology of this FLIER from the first maxima (i.e. $a_{x,1}$ and $a_{y,1}$). The width $a_{x,1}$ of the inner feature is unresolved at the present spatial resolution, which is $\leq 2 \times 10^{15}$ cm at the distance of 1.6 kpc; this feature abruptly broadens up to $0''.6$ (1.6×10^{16} cm). The characteristic scale $a_{y,1}$ of this feature linearly increases with distance from the source, resulting in an aspect ratio $a_{x,1}/a_{y,1} \leq 1$ and decreasing with distance to the source. At the outermost knot, the width $a_{x,1} \sim 0''.5$ in $\text{H}\alpha$ and $[\text{O III}]$, and it is unresolved in the $[\text{N II}]$ emission line. At this position, the knot is an elongated feature.

The $[\text{N II}]/\text{H}\alpha$ and $[\text{O III}]/\text{H}\alpha$ image ratios of the northern FLIER are shown in figure 5.15. In this figure, we have also included the $[\text{O III}]/[\text{N II}]$ ratio. The $[\text{O III}]/\text{H}\alpha$ ratio map

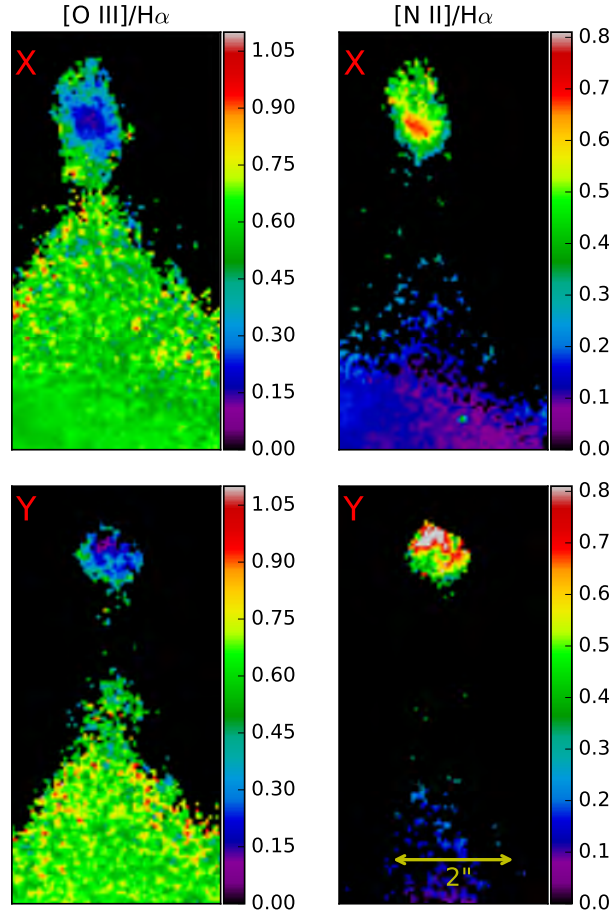


Figure 5.10: $[O III]/H\alpha$ (left column) and $[N II]/H\alpha$ (right column) ratios maps of knots X (top line) and Y (bottom line) of IC 4593.

don't show a spatial gradient in the inner jet and the outermost knot, showing a value from 3 to 4. The $[N II]/H\alpha$ emission line ratio shows a value ~ 0.25 at the inner jet. The $[N II]/H\alpha$ ratio shows a variation across the outermost knot, reaching values up to 0.6. The $[O III]/[N II]$ line ratio map illustrates that the inner and outer jet have similar excitation conditions, lower than the rest of the nebula.

The figure 5.16 shows the diagnostic diagram of small structure (ansae) of part N on the PN and the figure 5.17 shows the intensity distribution in the lines $[O III]$, $[N II]$ and $H\alpha$ of N structure with location $7''.24$, $7''.18$ and $7''.20$ respectively, we see very similar spatial distribution in all lines and the S structure is not visible.

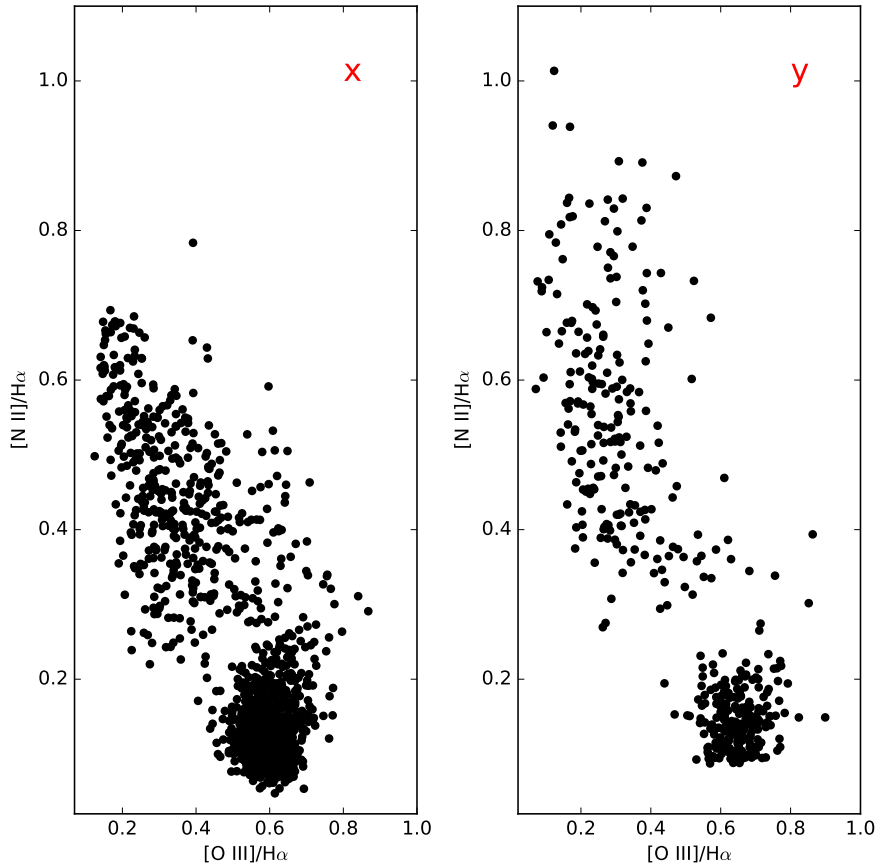


Figure 5.11: $[\text{O III}]/\text{H}\alpha$ vs. $[\text{N II}]/\text{H}\alpha$ diagnostic diagrams of morphological component X (right column) and Y (left column) of IC 4593. The size of the box is 81 x 131 pixels.

5.5.4. IC 4634

IC 4634 is an archetype of point-symmetric PNe (see Fig.5.1), with two pairs of jets ending in broad bow-shock features (named as A, A' by Guerrero et al. (2008)). The outermost bow shock-like structure lies 10'' NW of the central star. The counter bow-shock (A') is symmetrical, on the opposite side of the central source. A chain of knots extends towards the central source from both A and A', ending in a smaller sized bow-shock labeled B and B'. This PN is at a distance of 1.3 kpc (Bown, A.G.A., Vallenari, A., et al. (2018), GAIA Collaboration).

Figures 5.19 and 5.20 show the characteristic sizes across ($\langle a_x \rangle$) and along ($\langle a_y \rangle$) the NW and SE structures as a function of relative distance to the central source. These structures are characterized by strong similarities and some differences.

We first describe the characteristic widths (i.e., sizes across the polar axis) of the FLIERs.

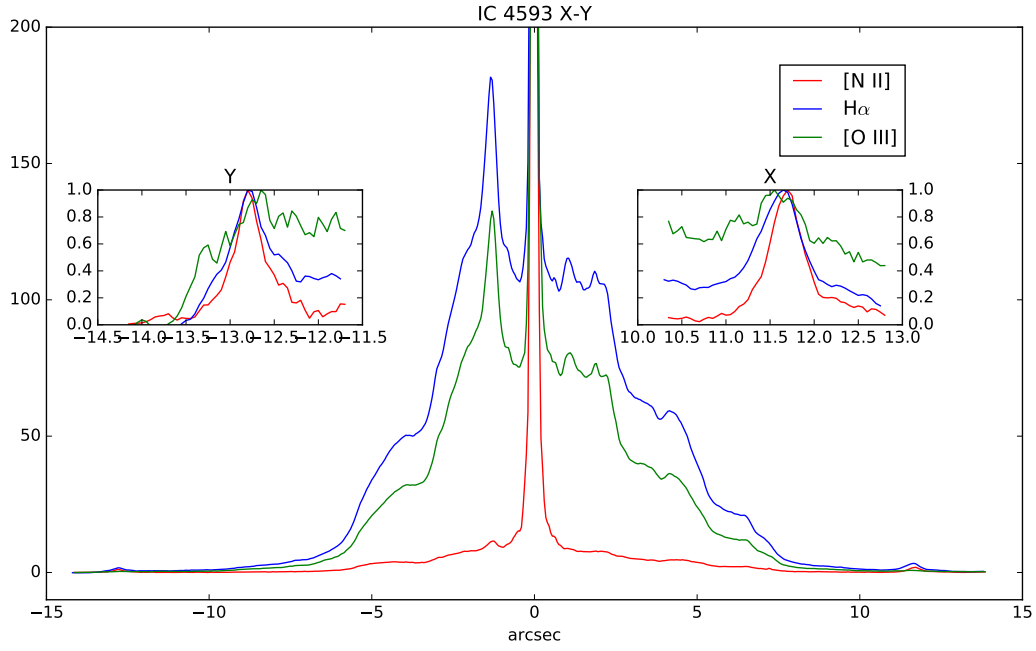


Figure 5.12: Profiles knots X and Y in lines [O III], [N II] and H α of IC 4593. [O III] (Green line), [N II] (red line) and H α (Blue line).

Along knots B and B' (the innermost regions) the width of the jet is more or less constant with values ranging from $0''.2$ to $0''.4$ (i.e., from 7.5×10^{15} to 1.4×10^{16} cm). At the outer edge of B and B' (i.e. the chain of knots) the width of the jet decreases with distance to the source (down to values $\sim 0''.2$). At the inner edge of the bow-shocks A and A', we see that $\langle a_x \rangle$ suddenly grows with the presence of large structures across the flow. The width of the features A and A' in the emission line of [N II] shows a mean value of $0''.8$ (3×10^{16} cm). These features are wider in the H α and [O III] images ($\sim 1''.2$).

The characteristic sizes along the jet show a V-shaped feature in the $\langle a_y \rangle - y$ plot, with a decrease in the size towards the intensity peak and increasing up to $1''.0$ to $1''.5$ (i.e., from 3.5×10^{16} – 5×10^{16} cm) moving downstream.

There is a noticeable spatial displacement of the peak of [N II] in B, B' with respect to the peak in the [O III] or H α emission lines. The spatial shift in the peak of [N II] at the leading (outward-facing) edge of B and B' is $0''.2$ (7.5×10^{15} cm) (B) and $0''.45$ (1.5×10^{16} cm) (B').

The chain of knots is clearly wider in [O III] and H α than in [N II]. The largest transversal structures (i.e. large $\langle a_x \rangle / \langle a_y \rangle$ ratio) are the outermost bow-shocks A and A' (with an aspect ratio up to 8). At the chain of knots in the intermediate region, the width

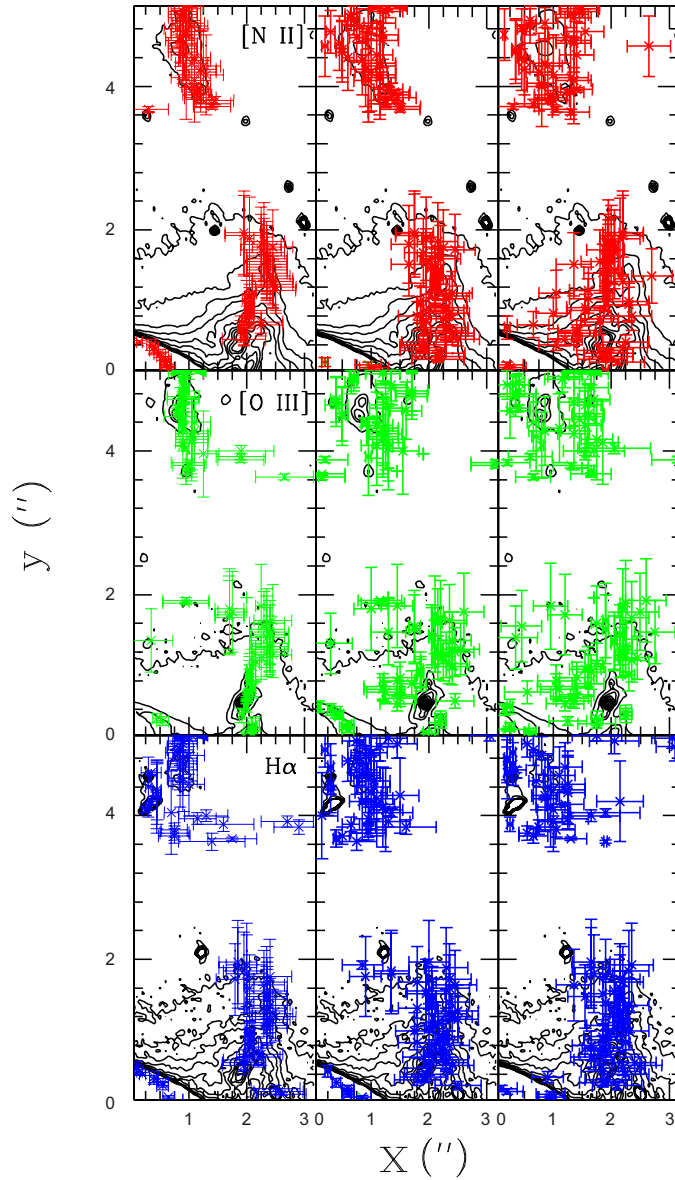


Figure 5.13: Contour plots of the jet of NGC 6210, where we show the positions (x_k, y) of the maxima. The characteristic sizes $((a_{x,k}, a_{y,k}))$ are shown as errorbars. [N II] (top panels, red), [O III] (middle panels, green) and $H\alpha$ (bottom panels, blue).

narrows with distance to the source (i.e. from B (B') to A (A')) showing an aspect ratio that decreases from ~ 4 to 1. There are noticeable differences in the aspect ratio of B and B', where the bow-shock B' is narrower (with a ratio $\langle a_x \rangle / \langle a_y \rangle \leq 1$). The low-ionization feature B shows an aspect ratio similar to that of feature A.

Figure 5.21 shows the [O III]/ $H\alpha$ and [N II]/ $H\alpha$ emission line ratios of the jets of IC 4634, which are characterized by the presence of abrupt changes in the ratio maps. We briefly

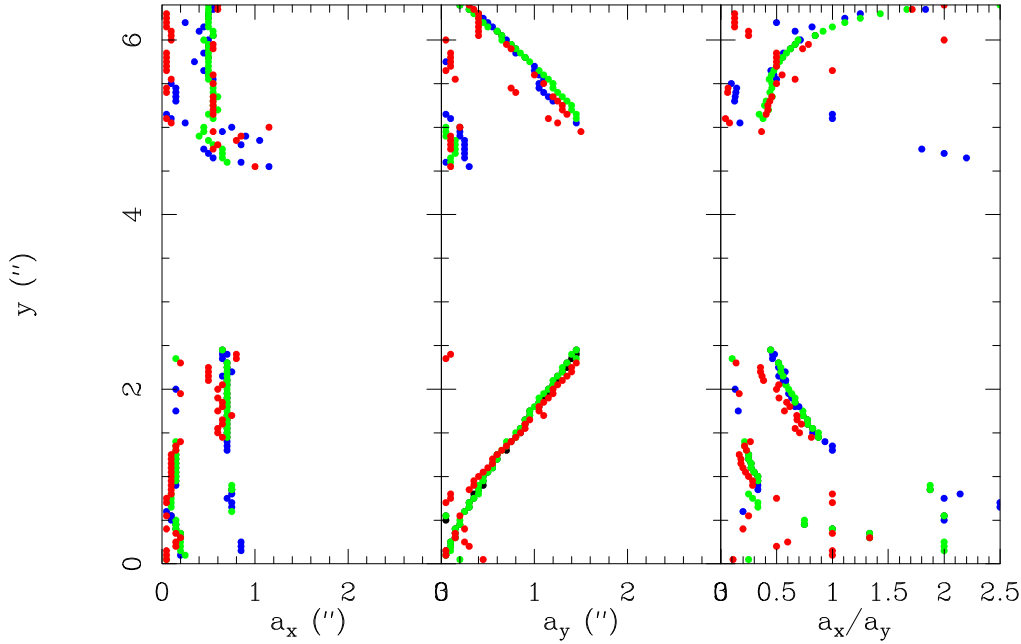


Figure 5.14: Wavelet analysis to N jet in NGC 6210. Symbols as in figure 5.4 See text for more details.

discussed the main properties of these maps. For a more detailed description see Guerrero et al, 2008. At the leading edge of A and A', the [O III] emission is enhanced, with a [O III]/H α values from 3 to 4. The presence of this skin of [O III] is discussed in Guerrero et al. (2013). Both A and A' show faint wings also more prominent in [O III] (with [O III]/H α values $\sim 3 - 4$). The features A and A' show several knots which are bright in [N II] and faint in [O III] (with [O III]/H α values ~ 1). Behind these knots, moving towards the central source, the [O III]/H α is ~ 1.5 to 2. Knots at the leading bow-shocks are the brightest features in [N II], with [N II]/H α ratios $\sim 0.5 - 0.6$. The [N II]/H α abruptly decreases upstream.

The figure 5.22 shows the relation between [O III]/H α Vs. [N III]/H α . we can see the diagnostic diagrams features A' and B' in figure (a) while the features of A and B in (b), we see the range for two diagrams is the same in [N III]/H α between 0,0 and 0.6 while [O III]/H α the range is 1.5 to 3.5 and the behavior is the same of previous PNe. The bow shock profiles of IC 4634 shows the location of A and A' in the figure 5.23 and the location of B and B' in fig. 5.24, in the both figures we can see the symmetrical intensity distribution for the structures for A and A' is $\sim \pm 11''.09$ while for B and B' are $7''.09$ and $-8''.17$ respectively and the star is in the center of profile ($0.0''$).

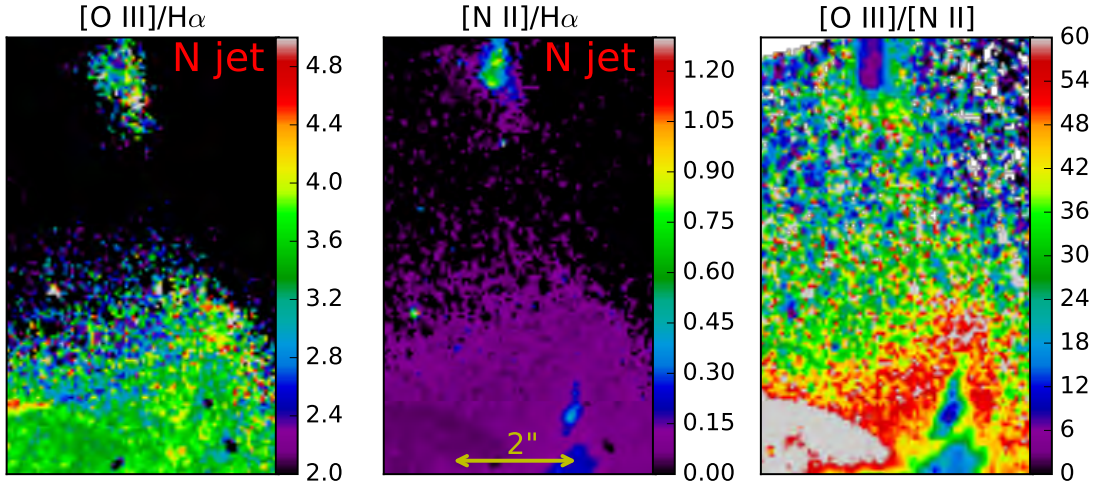


Figure 5.15: $[\text{O III}]/\text{H}\alpha$ (left), $[\text{N II}]/\text{H}\alpha$ (middle) and $[\text{O III}]/[\text{N II}]$ (right) emission line ratio maps of the northern FLIER of NGC 6210.

5.5.5. NGC 6543

NGC 6543 is a bright well-studied PN with a complex morphology (see, e.g., Balick 2004). The core of NGC 6543 has an elliptical outline. It appears as two concentric crossed ellipses, with the major axis oriented at 25° and 115° (Miranda and Solf 1992). The ellipse is aligned along the core's major axis and is the optimum structure for expansion studies because of the prominent and sharp edges along its minor axis and its well-measured expansion velocity. We know this ellipse like E25 (Reed & Balick 1999).

In addition to the ellipses, three pairs of low-ionization structures are found at the edge of the core: caps (DD'), ansae (FF') and jet-like features (JJ'), the designation of the features are those of Miranda and Solf (1992). The bright core is surrounded by a series of concentric rings; the rings are surrounded by a faint, extended, filamentary halo (Middlemass, Clegg and Walsh 1989). The distance of the nebula, measured directly from the expansion parallax, is 1.625 kpc (Bown, A.G.A., Vallenari, A., et al. (2018), GAIA Collaboration). The jet-like features (J, and J') are two thin, radial, low-ionization features that protrude from the core into the halo. They do not lay along the symmetry axis of any other feature. The Doppler shifts measured by Miranda and Solf (1992) increase from $\pm 18 \text{ km s}^{-1}$ where

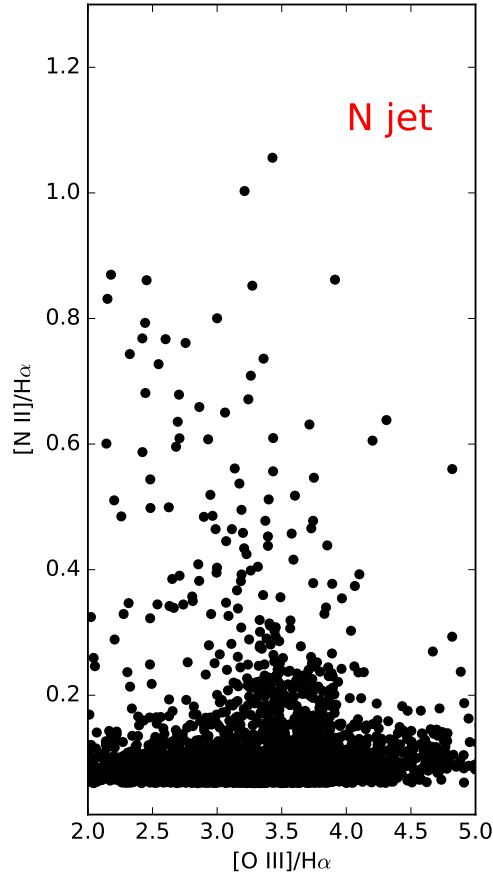


Figure 5.16: $[\text{O III}]/\text{H}\alpha$ Vs. $[\text{N II}]/\text{H}\alpha$ diagnostic diagram of morphological component of N jet of NGC 6210. The size of the box is 81 x 131 pixeles

the jet emerges from the caps to $\pm 36 \text{ km s}^{-1}$ at the outer tips.

The results obtained from the wavelet analysis of the features J, J' and the ansae F are shown in figures 5.25 and 5.26, where we analyze the spatial scales of the first maximum (i.e., $a_{x,1}$, $a_{y,1}$).

The jet-like feature J' shows a bright compact knot in all three maps (marked as BK in figure 5.27). This feature shows small scales across the flow axis in the $[\text{N II}]$ emission line, with $a_{x,1} \sim 0''.1$ (unresolved at the spatial resolution of the HST-WFPC2; i.e., $\leq 1.5 \times 10^{15} \text{ cm}$). At the innermost region of J', we see structures in $[\text{N II}]$ that are elongated along the outflow axis, with an aspect ratio ≤ 0.5 . At larger distances from the central star, the jet J' is a narrow structure, showing an $a_{x,1}/a_{y,1}$ ratio ≤ 1 . The feature J' is wider in $\text{H}\alpha$ and particularly in $[\text{O III}]$, with a more or less constant value of $0''.7$ (i.e., 10^{16} cm).

Figure 5.28 shows the spatial scales of the jet J and the ansae F as a function of position along the flow. The jet-like feature J show small transversal structures which, in the $[\text{N}$

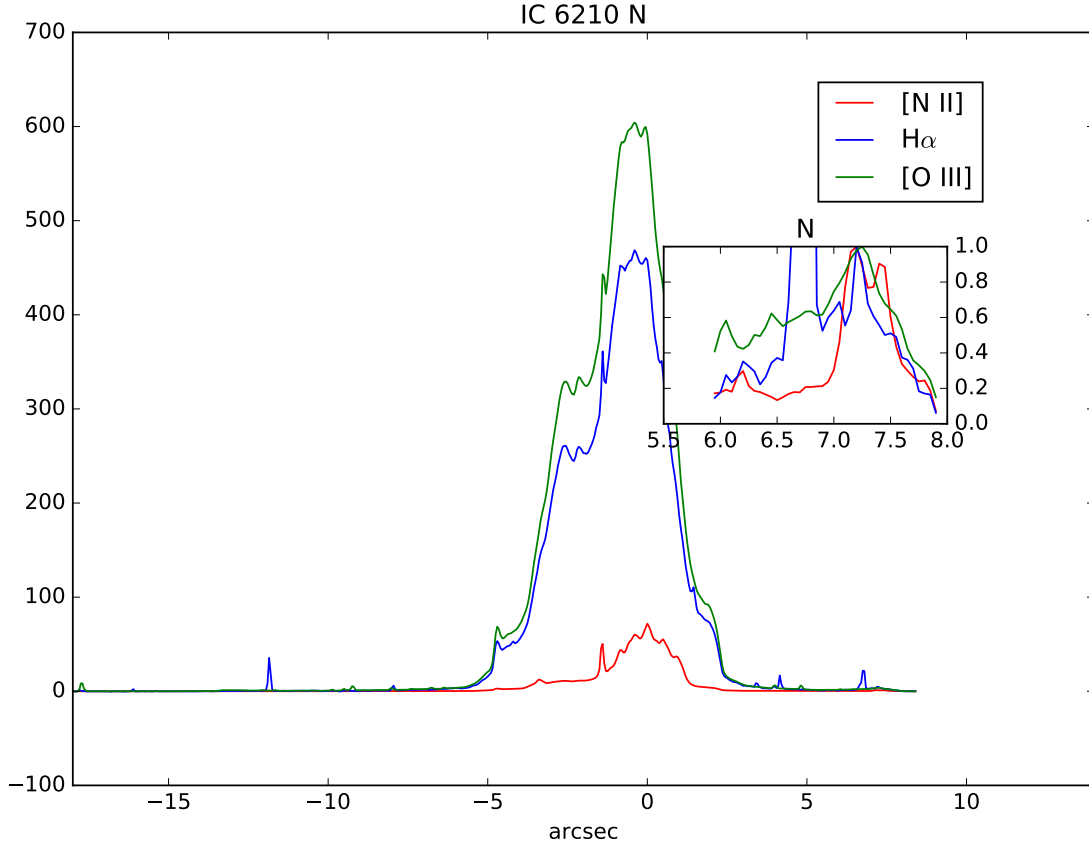


Figure 5.17: Profiles in emission lines of [O III] (red line) , [N II] (green line) and $H\alpha$ (blue line) to north structure in NGC 6210.

II] emission line, range from $0''.1$ (i.e. unresolved) up to $0''.3$ (i.e. 4.5×10^{15} cm). The widths across the flow axis are larger in the $H\alpha$ and [O III] emission line images, with a mean values of $0''.75$ ($\simeq 10^{16}$ cm). Along feature F, we see a transition from transversal structures, which are elongated across the symmetry axis, to elongated features along the flow. The largest structures across the flow have widths of $\sim 0''.6$ (i.e., 9×10^{15} cm) in [N II], and $0''.75$ in [O III] and $H\alpha$.

Figure 5.29 shows the [O III]/ $H\alpha$ and [N II]/ $H\alpha$ line ratio maps of the outer FLIERs of NGC 6543. The jet-like features J and J' are faint in [O III] and prominent in [N II]. Both features show large values of [N II]/ $H\alpha$ (~ 1.0 to 1.5), and a [O III]/ $H\alpha \sim 1.4$.

In the Figures 5.30 and 5.31 shows the features of diagnostic diagram and intensity distribution over the cross section of the structures F, F' and jet-like J-J' of NGC 6543 respectively. In the diagram see the same behavior of the previous PNe. The location for the F peak is $-6''.59$ for [N II] and $-6''.52$ for $H\alpha$ while F' are $7''.05$ and $7''.07$, the peak of

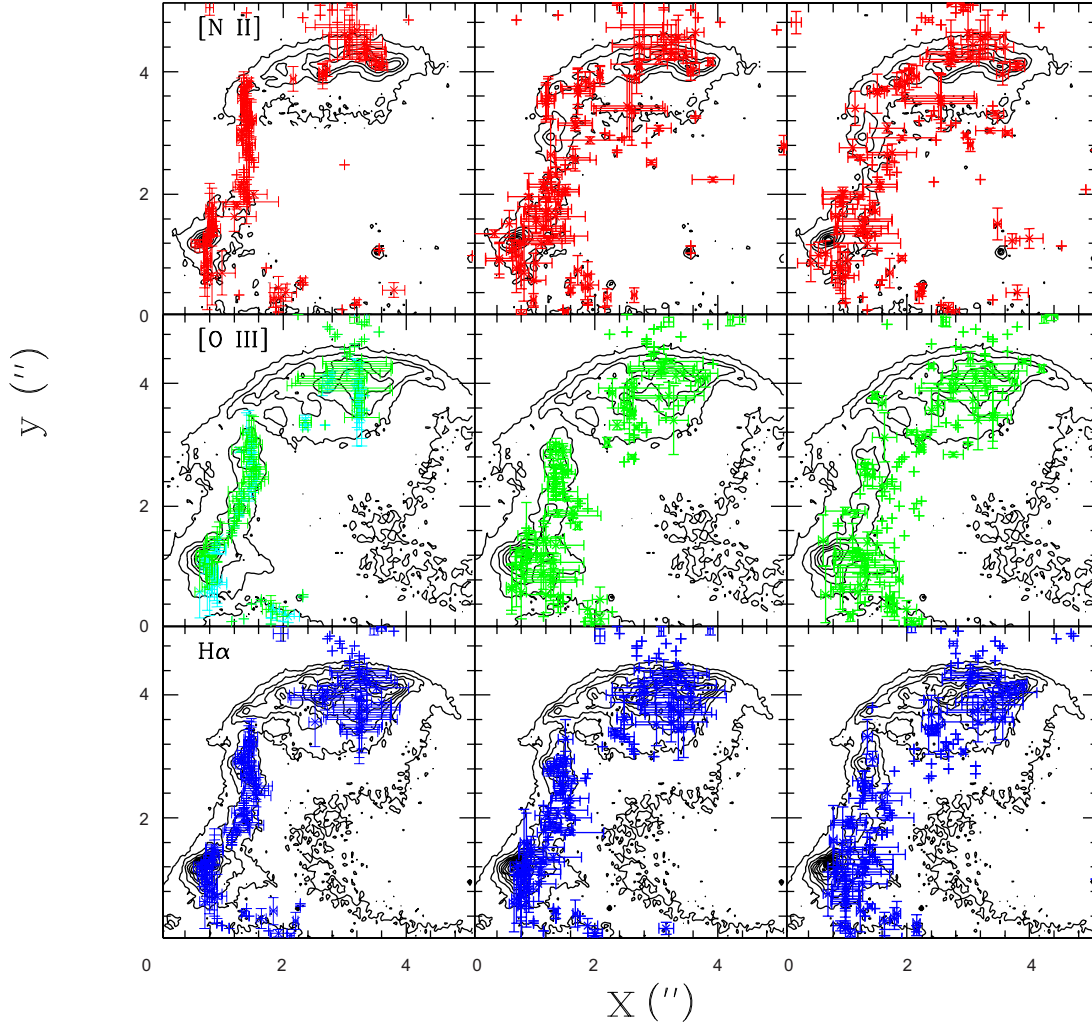


Figure 5.18: Contour plots of the structures A and B of IC 4634 where we show the positions (x_k, y) of the maxima. The characteristic sizes $((a_{x,k}, a_{y,k}))$ are shown as errorbars. [N II] (top panels, red), [O III] (middle panels, green) and H α (bottom panels, blue)

[O III] is not visible in any structure.

Figure 5.32 shows the [O III]/H α and [N II]/H α line ratio maps of the inner FLIERs of NGC 6543. The ansae features F and F' are faint in [O III] and prominent in [N II]. Both features show large values of [N II]/H α (~ 0.2 to 1.8), and a [O III]/H $\alpha \sim 1.2$ to 1.8 .

The Figure 5.33 shows the features of dispersion and see the same behavior as previous structures but in this case the points are very close to each other, and the profile in the figure 5.34 represent the structures F and F', but in this case no shows any peak.

We see in the diagnostic diagrams for both structures have the same range in [O III]/H α (1.5 to 3.0) and for [N II]/H α are 0.0 to 1.5 approximately, but the concentration in the

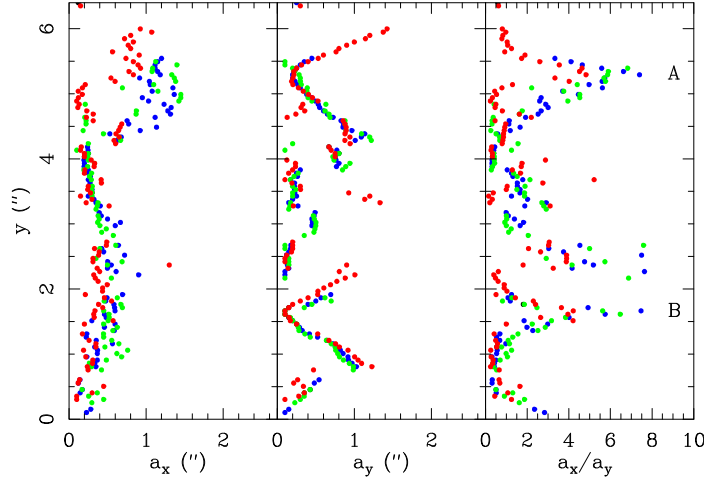


Figure 5.19: Wavelet analysis to IC 4643 in A and B features. Average $\langle a_x \rangle$ (left), $\langle a_y \rangle$ (middle), and the $\langle a_x \rangle / \langle a_y \rangle$ (right) ratio plotted as a function of relative distance to the central star. Blue circles correspond to H α , green circles correspond to [O III] 5007 Å, and red circles correspond to [N II] 6584 Å. See text for details.

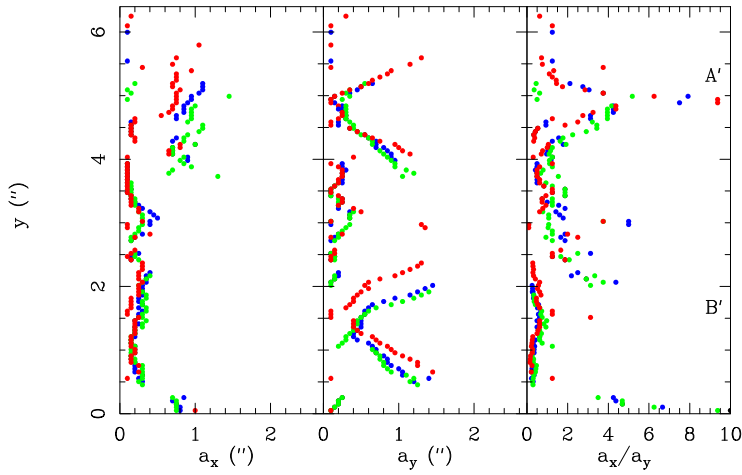


Figure 5.20: Wavelet analysis in A' and B' features. Symbols and distribution as in figure 5.19.

F'-F is more high than J'-J.

5.5.6. NGC 7009

NGC 7009 is a bright elliptical nebula with two FLIERs at a distance $\pm 24''$ west and east of the central source. These FLIERs/ansae include a pair of low-ionization knots which are connected to the core by thin tails (Goncalves et al. 2003). On a larger scale, NGC

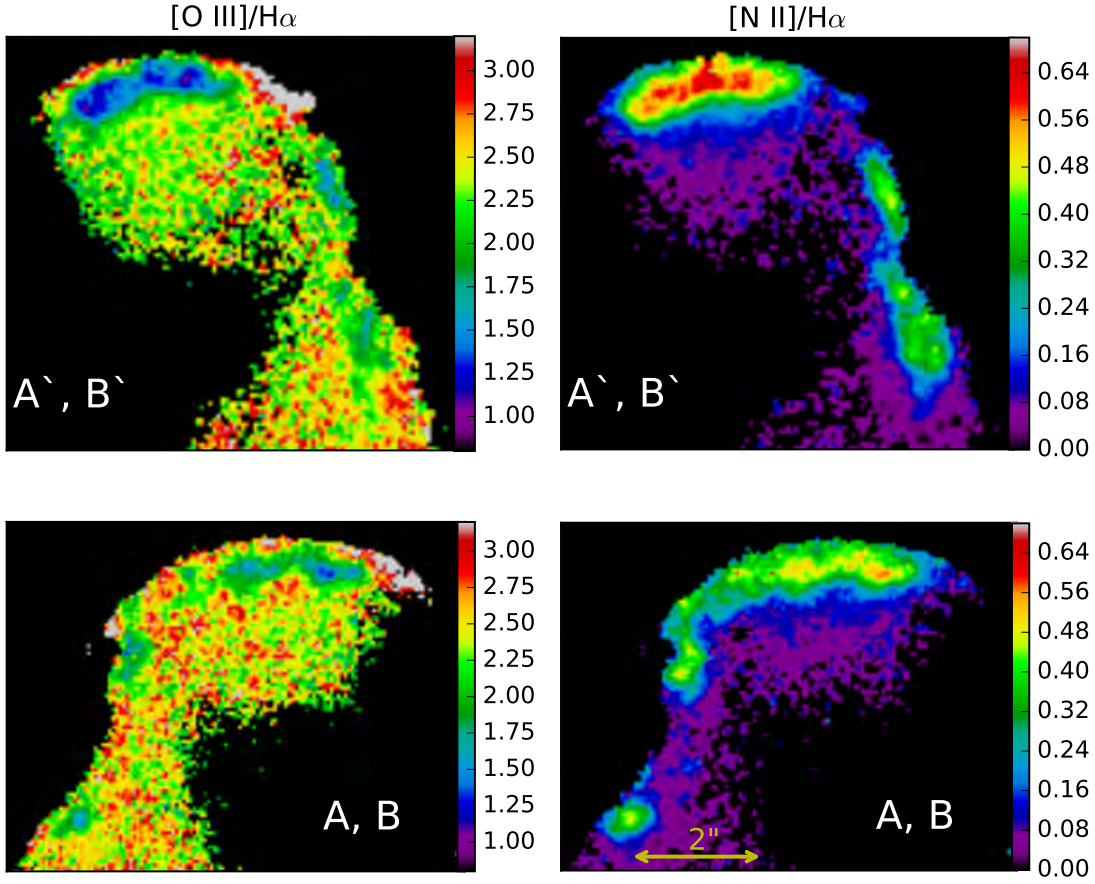


Figure 5.21: $[\text{O III}]/\text{H}\alpha$ (left column) and $[\text{N II}]/\text{H}\alpha$ (right column) ratios of the outer bow-shocks of IC 4634. The features A and B are plotted in first line in the panel, while the features A' and B' are plotted in the second line of panel.

7009 has a tenuous halo with a diameter of $4'$ (Moreno, de la Fuente & Gutiérrez 1998), which inner region displays a system of concentric rings (Corradi et al. 2004). Its central star is a H-rich O-type star, with effective temperature 82000 K (Méndez, Kudritzki & Herrero 1992). The distance adopted for this PNe is 1.154 kpc (Bown, A.G.A., Vallenari, A., et al. (2018), GAIA Collaboration).

The Doppler shifts of the outer knots are only about $\pm 6 \text{ km s}^{-1}$ (Reay & Atherton 1985), while their proper motions are $\sim 28 \text{ mas yr}^{-1}$ (Fernández, Monteiro & Schwartz 2004; Rodríguez & Gómez 2007), which suggest outflow velocities $\sim 100 \text{ km s}^{-1}$ for a distance of 0.86 kpc (Fernández, Monteiro & Schwartz 2004). We adopt the designation of the features from Gonçalves et al. (2003), where J1 and J2 are the jet feature in the west and east

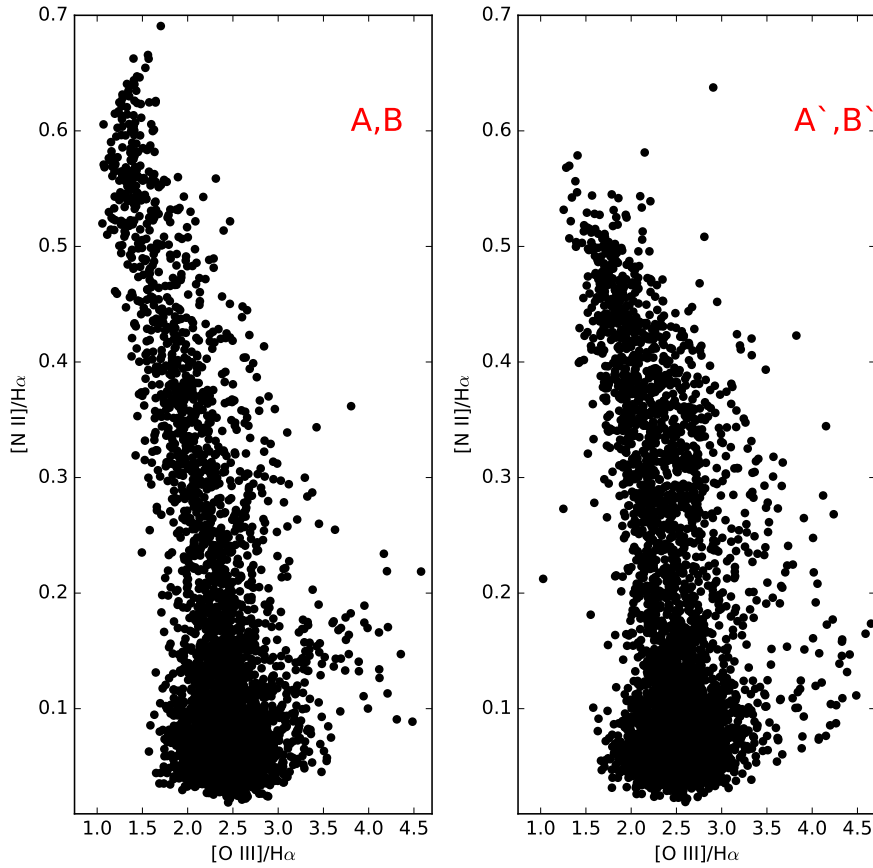


Figure 5.22: $[O III]/H\alpha$ Vs. $[N II]/H\alpha$ diagnostic diagrams of morphological component A, B (right column) and A', B' (left column) of IC 4634. The size of the box in this case is different, the left figure is 131 x 101 pixels and the other box is 111 x 101 pixels.

ansae, respectively. The outermost knots are called K1 and K4 (see figure 5.1).

Figures 5.36 and 5.38 show the characteristic sizes across and along the bipolar axis of the east and west ansae. We first describe the characteristic widths across the faint features named J1 and J2. Notice that J1 and J2 have similar spatial sizes, with a more or less constant value of the spatial length of the wavelet across the outflow $\langle a_x \rangle$ of $\sim 1''.2 - 1''.4$ (i.e., 1.5×10^{16} cm) in all emission lines. The characteristic sizes along the flow ($\langle a_y \rangle$) are $\leq 0''.4$ in $[N II]$. At the inner edge of J1 and J2, $\langle a_y \rangle$ linearly increases with distance to the source in the $[O III]$ emission line and $H\alpha$. Knot K4 shows a bright component with several clumps and a faint structure at larger distances to the central source (see figure 5.36). The bright feature shows clumps with $\langle a_x \rangle \geq 0''.4$ (i.e. 5×10^{15} cm) in $[N II]$. The width across the outflow of these structures is $\sim 0''.6$ in $H\alpha$ and up to $1''.2$ in $[O III]$. The aspect ratio of these clumps is ≤ 1 in $[N II]$. The elongation along

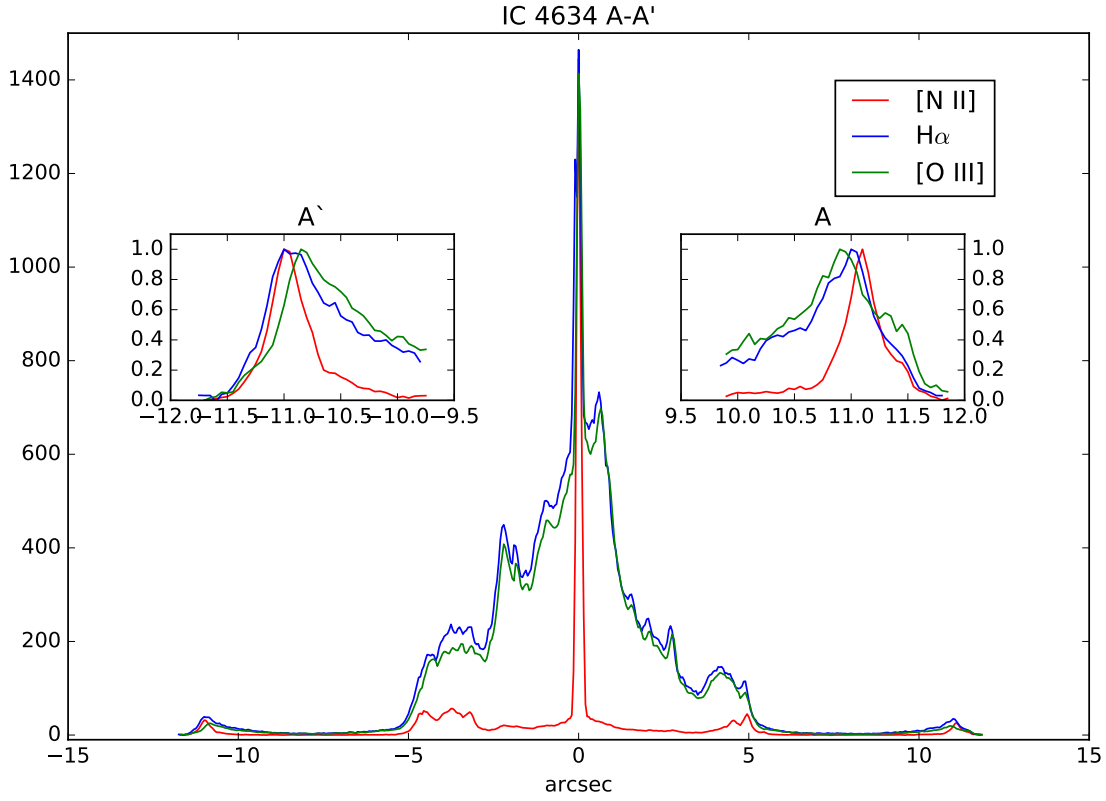


Figure 5.23: Profile A and A' in lines [O III] (green line), [N II] (red line) and H α (blue line). In the center shows the central source.

the flow axis decreases along feature K4 from $1''.4$ to $0''.4$ and increases downstream. The faint feature at larger distances from the central star, also shows $\langle a_x \rangle$ spatial size $\leq 0''.4$ in the [N II] image.

Figure 5.38 shows the characteristic sizes of knot K1, which shows several clumps at arcsecond scales in the [N II] emission line image. These features show small spatial scales across and along the outflow axis with $\langle a_x \rangle \simeq \langle a_y \rangle \simeq 0''.4$ (i.e. 5×10^{15} cm). The knot K1 is wider in the [O III] and H α ($1''.0$ to $1''.4$) emission lines.

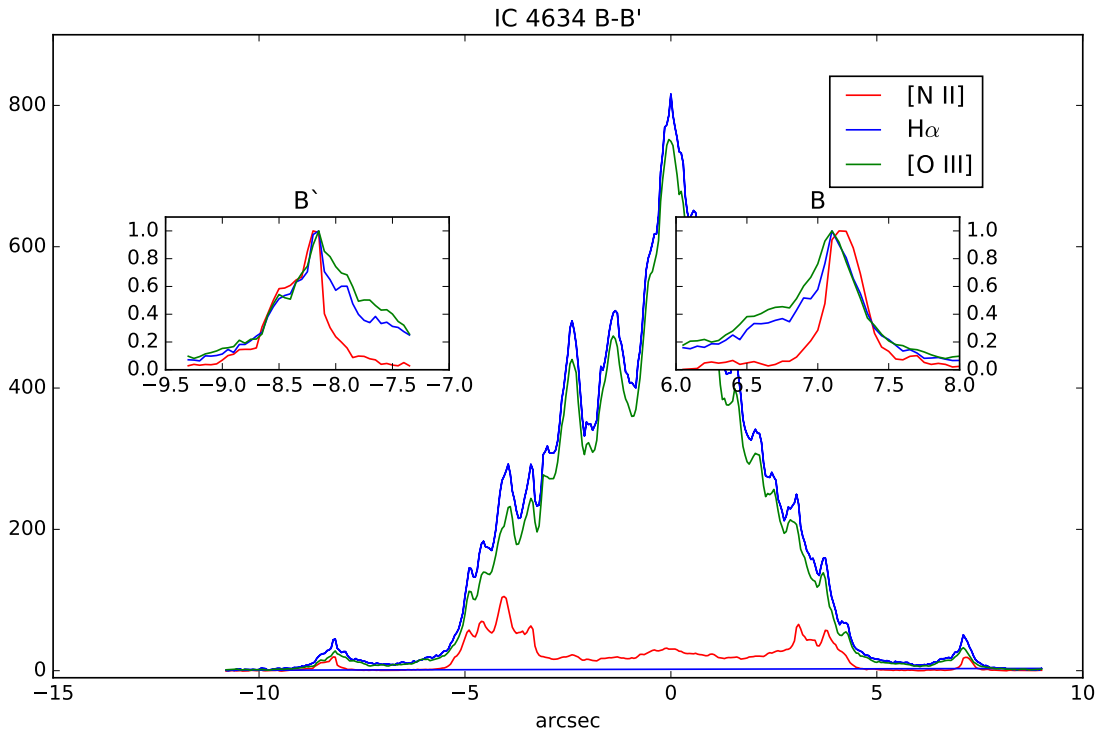


Figure 5.24: Profile B and B' in lines [O III], [N II] and H α . Colors as in figure 5.23

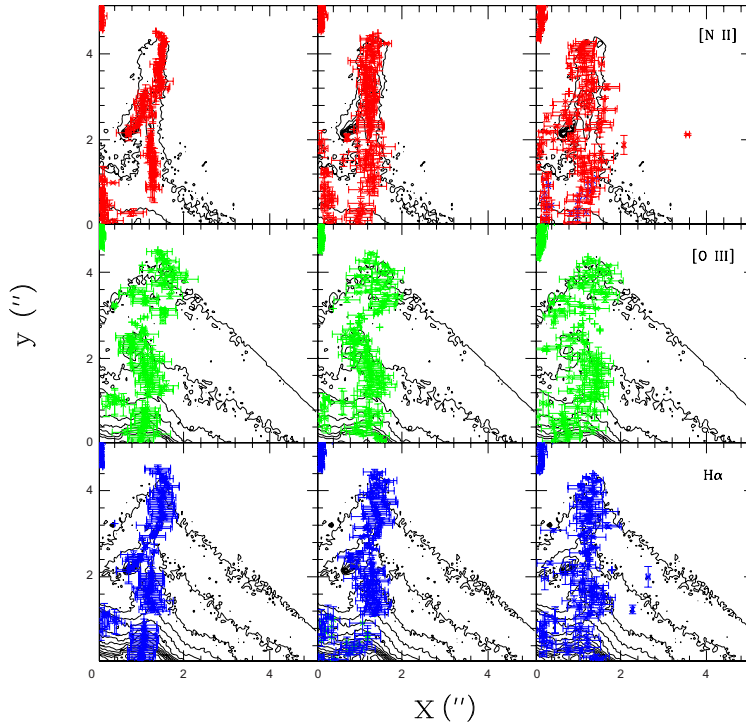


Figure 5.25: Contour maps of the feature J' to NGC 6543. [N II] (top in red), [O III] (middle in green) and H α (bottom). Symbols as in figure 5.13.

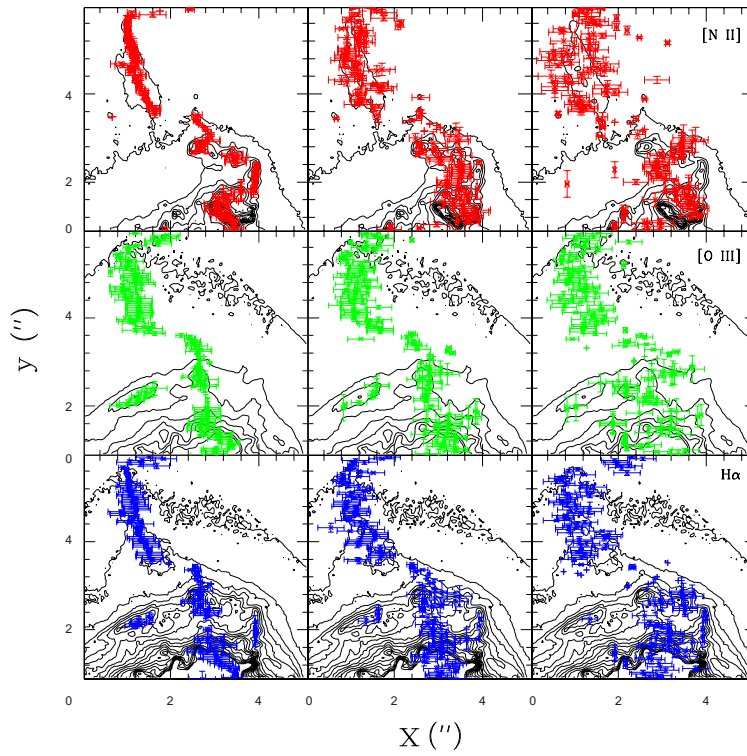


Figure 5.26: Contour maps of the features J and F to NGC 6543. [N II] (top in red), [O III] (middle in green) and H α (bottom). Symbols as in figure 5.13.

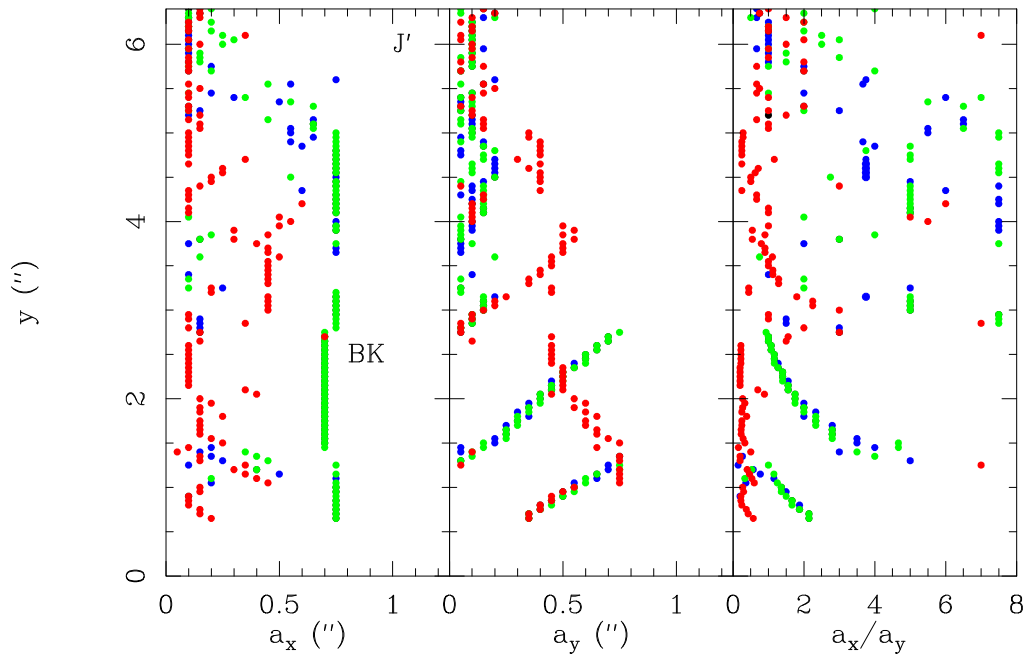


Figure 5.27: Wavelet analysis to J' feature. Average $\langle a_x \rangle$ (left), $\langle a_y \rangle$ (middle), and the $\langle a_x \rangle / \langle a_y \rangle$ (right) ratio plotted as a function of relative distance to the central star. Blue circles correspond to $H\alpha$, green circles correspond to $[O\ III]\ 5007\ \text{\AA}$, and red circles correspond to $[N\ II]\ 6584\ \text{\AA}$. See text for more details.

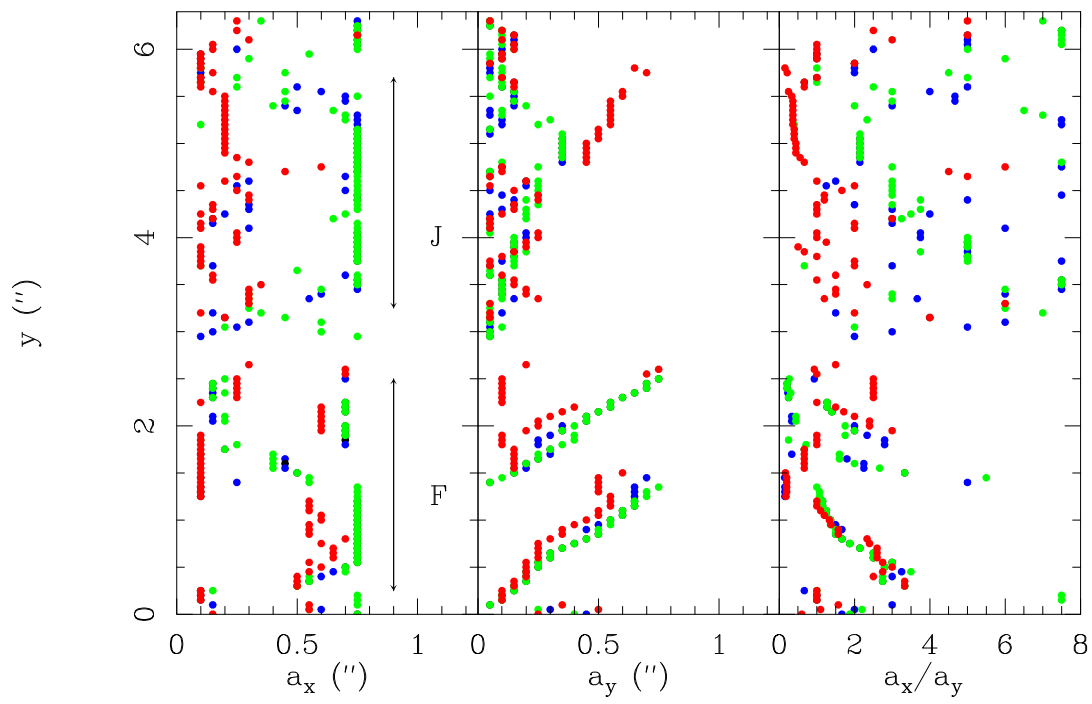


Figure 5.28: Wavelet analysis to F structure. Symbols as in figure 5.27 See text for more details.

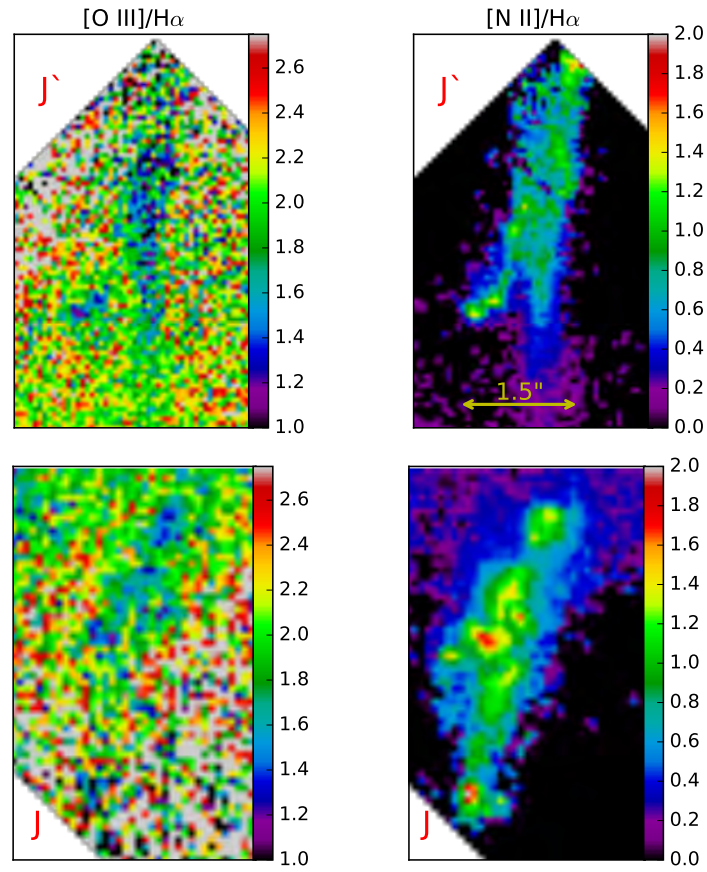


Figure 5.29: $[\text{O III}]/\text{H}\alpha$ (left panels) and $[\text{N II}]/\text{H}\alpha$ (right panels) ratio maps of the feature J' (a and b) and features J (c and d) of NGC 6543.

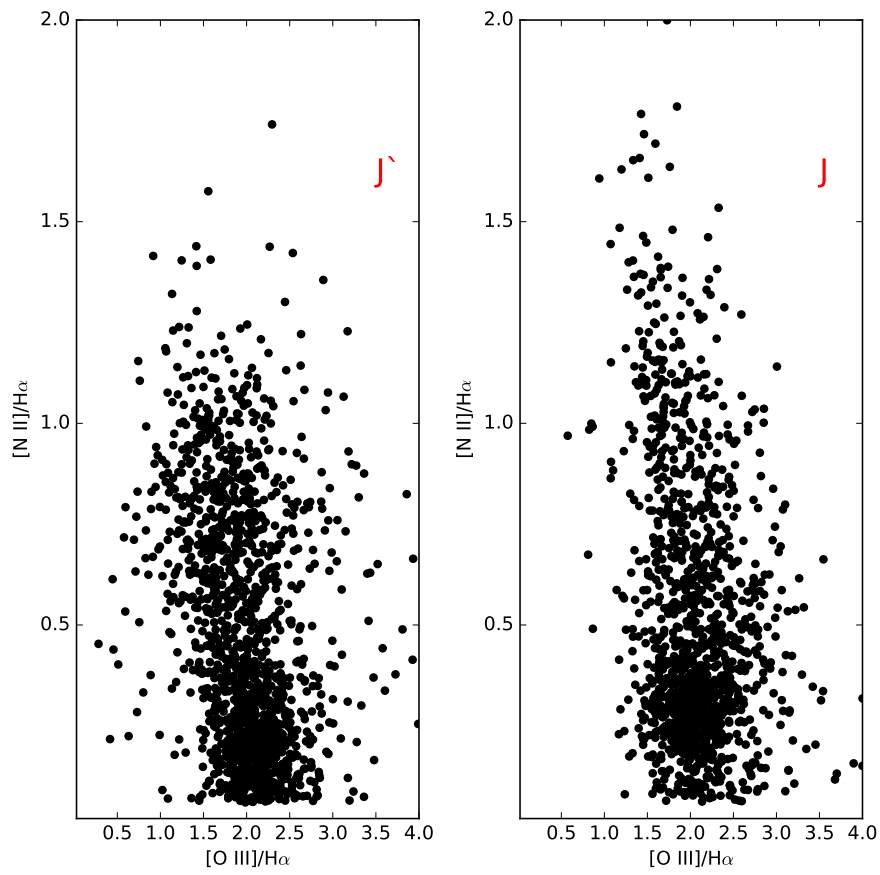


Figure 5.30: $[O\ III]/H\alpha$ Vs. $[N\ II]/H\alpha$ diagnostic diagrams of morphological component J' (right column) and J (left column) of NGC 6543 . The size of the box is 41 x 60 pixels.

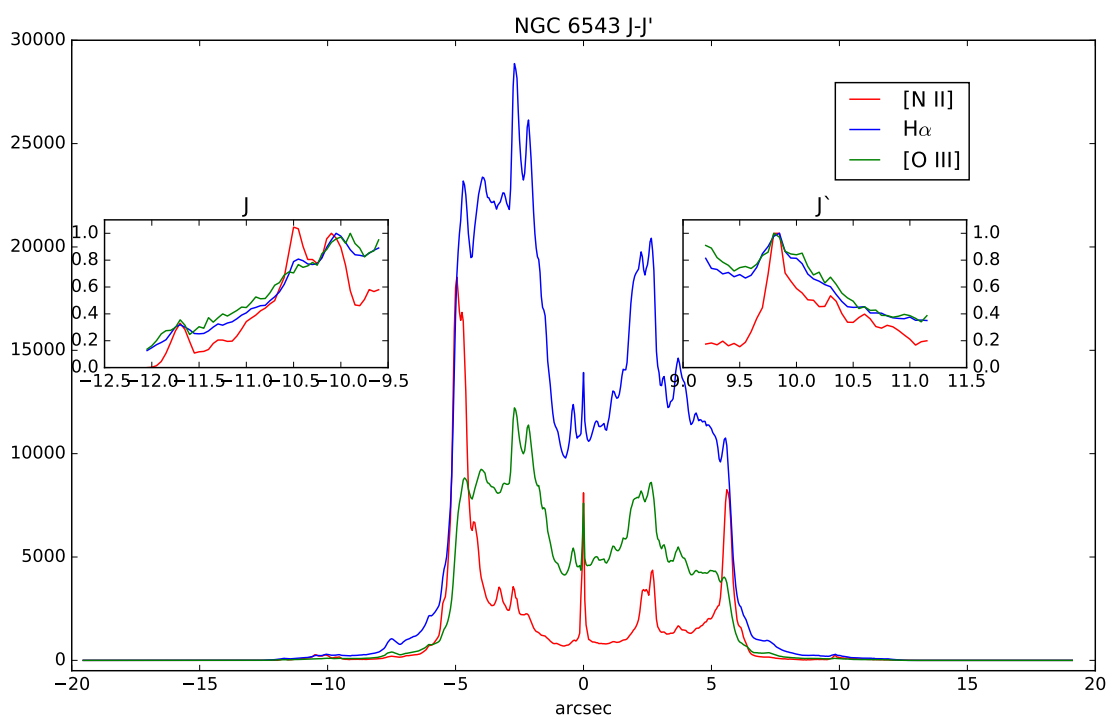


Figure 5.31: J and J' profiles in emission lines [O III], [N II] and $H\alpha$.

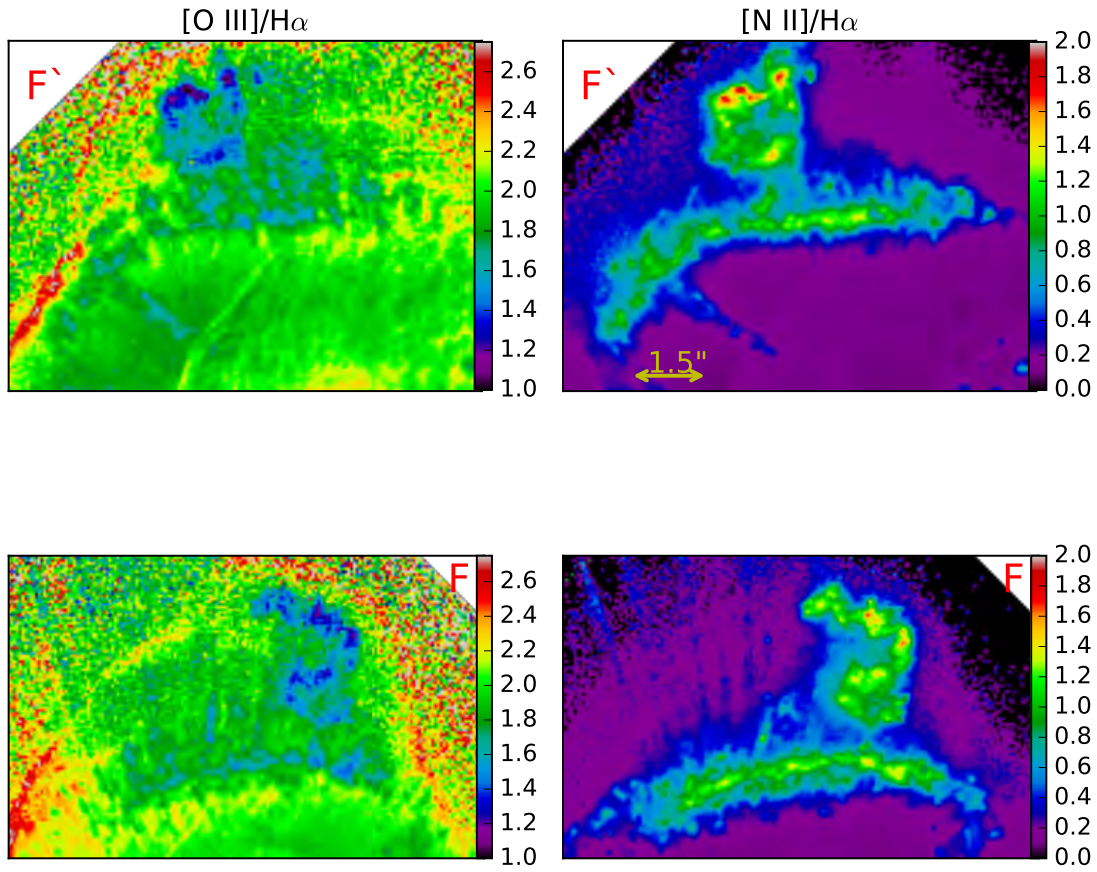


Figure 5.32: $[\text{O III}]/\text{H}\alpha$ (left panels) and $[\text{N II}]/\text{H}\alpha$ (right panels) ratio maps of the feature F' (first row) and features F (second row) of NGC 6543.

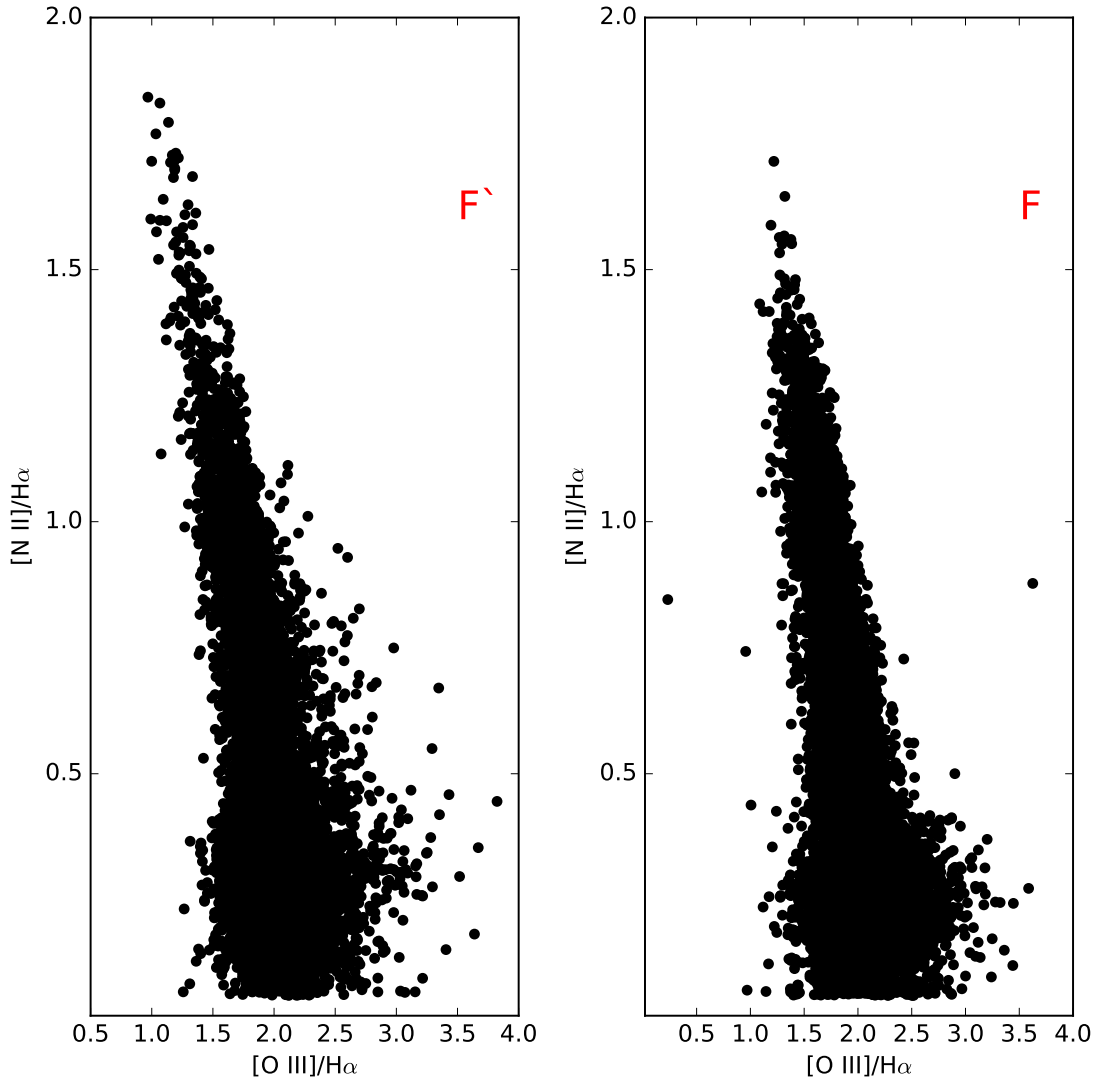


Figure 5.33: $[O III]/H\alpha$ Vs. $[N II]/H\alpha$ diagnostic diagrams of morphological component F' (right column) and F (left column) of NGC 6543. The size of the box is 176 x 112 pixels.

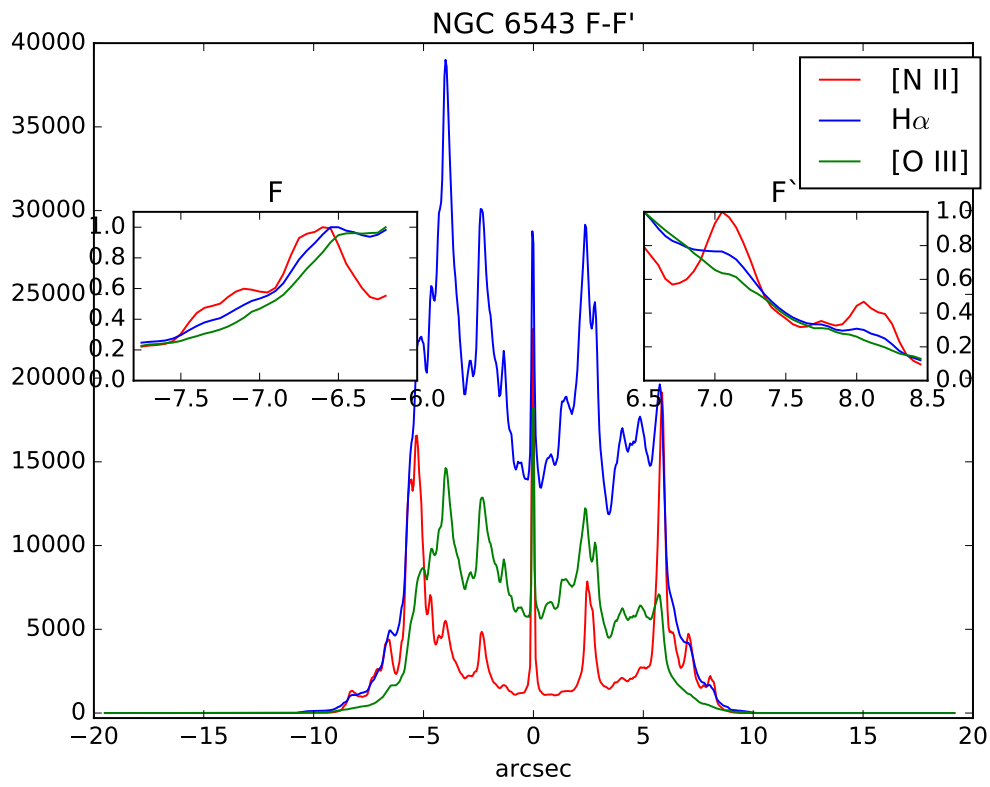


Figure 5.34: F' and F Profiles in emission lines [O III], [N II] and H α .

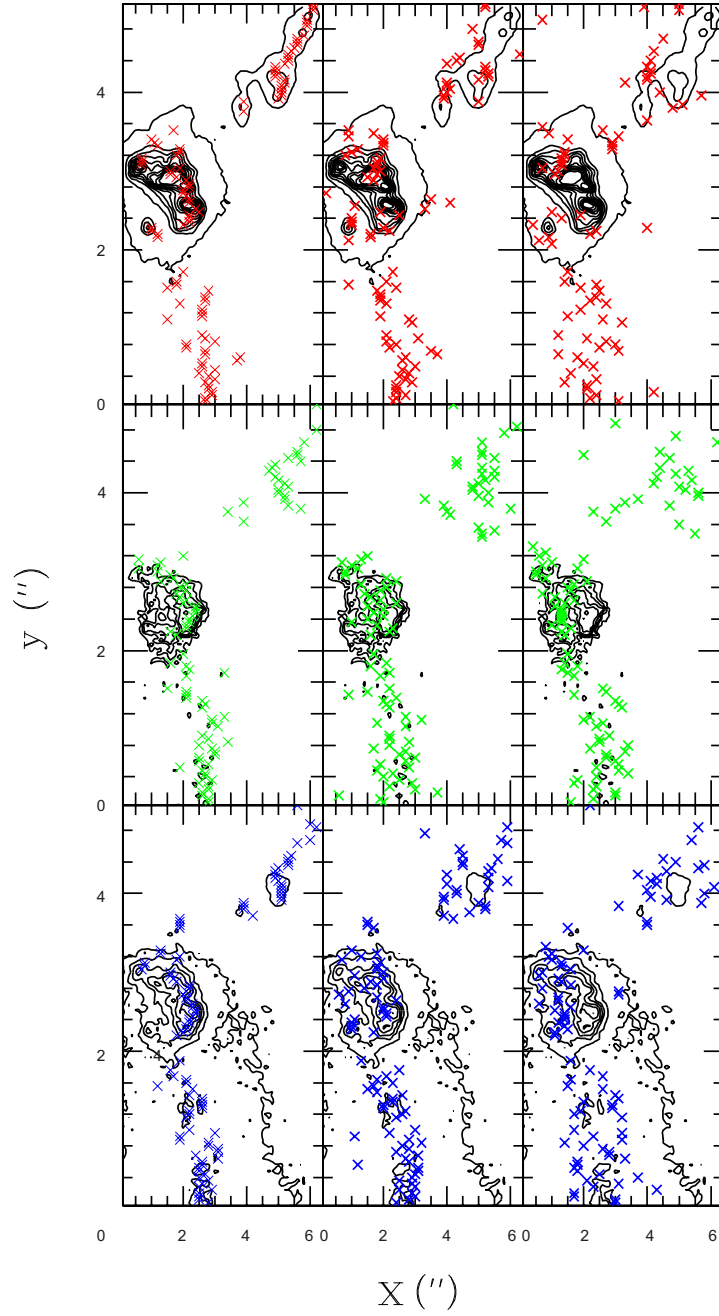


Figure 5.35: Contour maps to the feature *K4* (A and B) to NGC 7009. [N II] (top, red), [O III] (middle, green) and H α (bottom, red). Symbols as in figure 5.13.

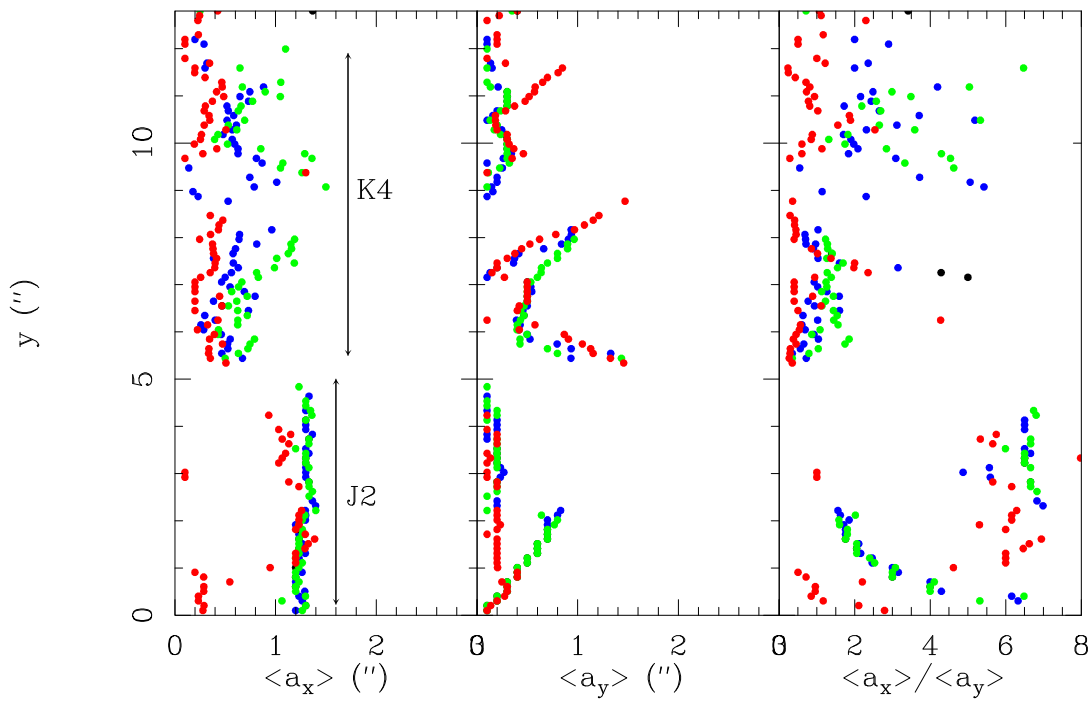


Figure 5.36: Wavelet analysis to NGC 7009. Symbols as in figure 5.19 See text for more details.

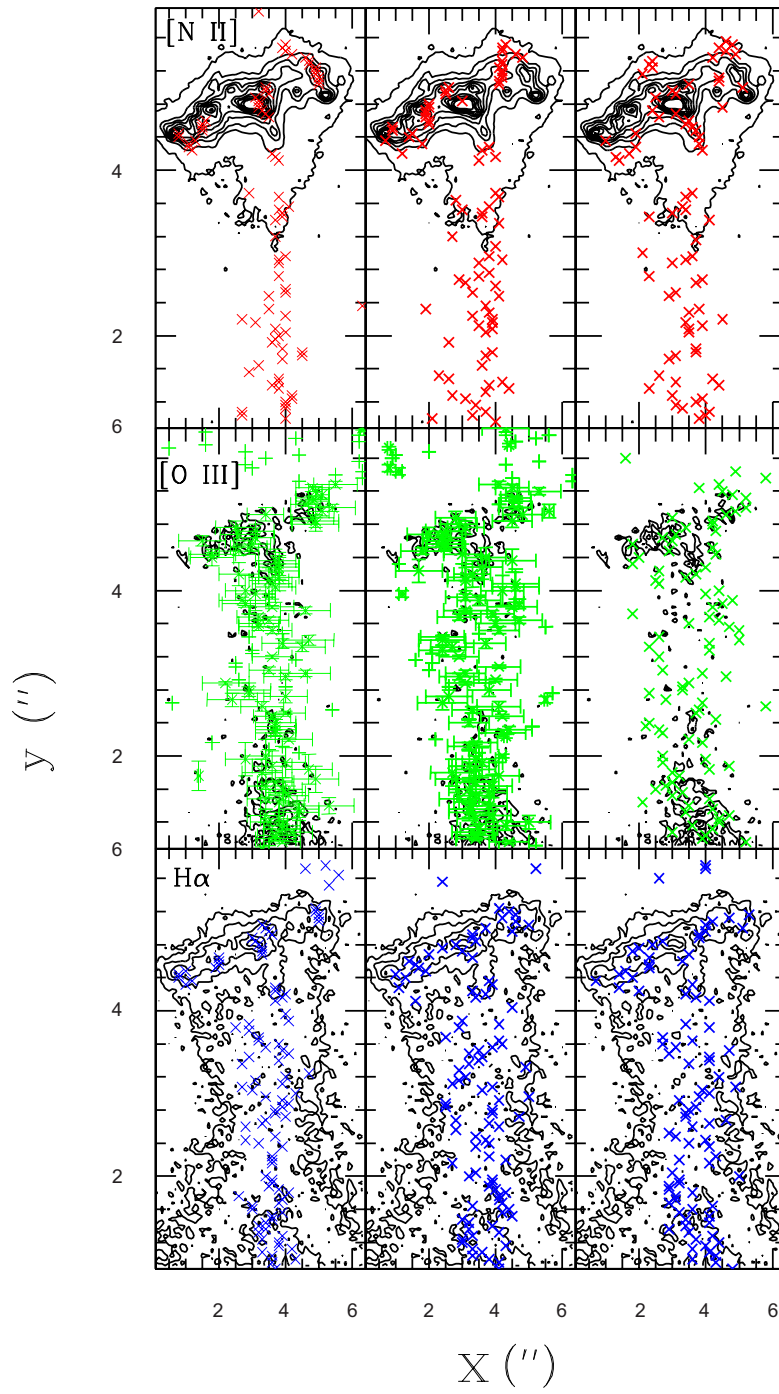


Figure 5.37: Contour maps to the feature *K1* to NGC 7009. [N II] (top, red), [O III] (middle, green) and Hα (bottom, red). Symbols as in figure 5.13.

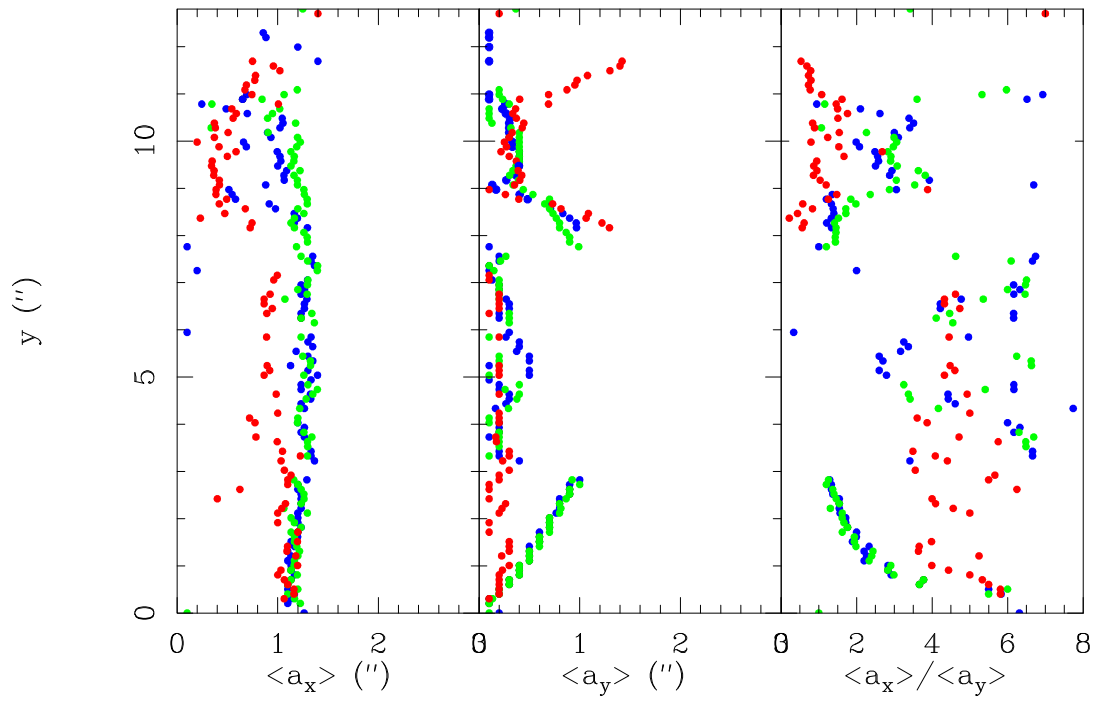


Figure 5.38: Wavelet analysis to K1 structure. Symbols as in figure 5.19 See text for more details.

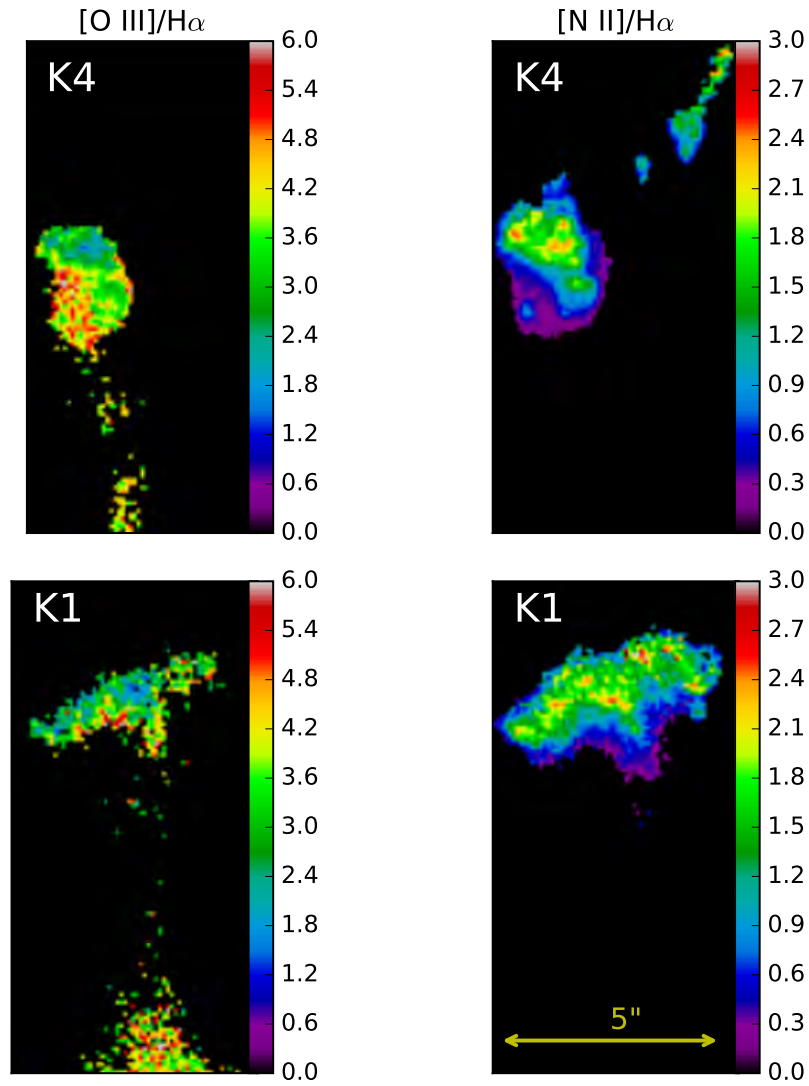


Figure 5.39: $[O III]/H\alpha$ (left panels) and $[N II]/H\alpha$ (right panels) ratio maps of the feature K4 (A and B) (first row) and features K1 (second row). In the $[O III]/H\alpha$ is not visible the structure B of NGC 7009.

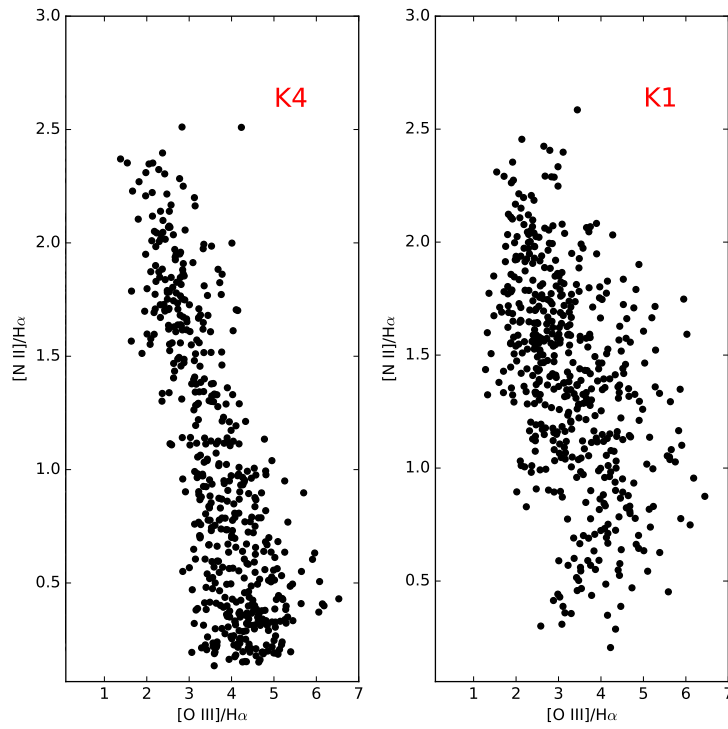


Figure 5.40: $[\text{O III}]/\text{H}\alpha$ Vs. $[\text{N II}]/\text{H}\alpha$ diagnostic diagrams of morphological component K4 (right column) and K1 (left column) of NGC 6543 . The size of the box for both structure is 64 x 128 pixels.

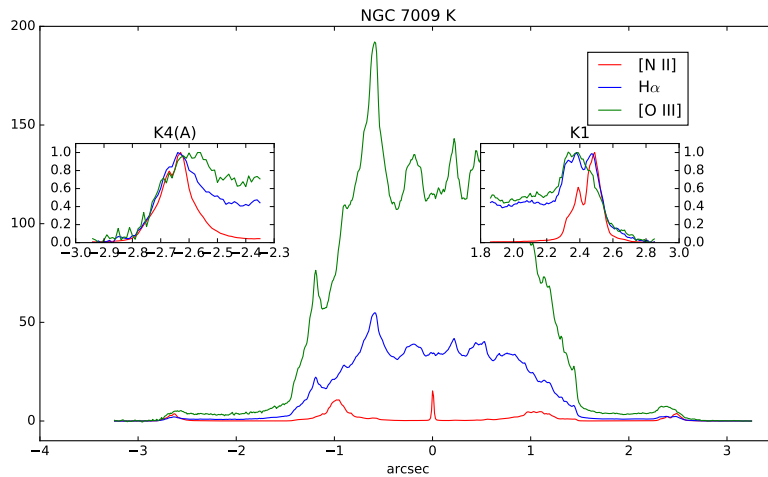


Figure 5.41: Profile in emission lines [O III] (green line), [N II] (red line) and H α (blue line) to K1 and K4 structures.

The [N II]/H α and [O III]/H α emission line ratios of the outermost knots (K1 and K4) are shown in figure 5.39. The jet-like features J1 and J2 are faint in all emission lines and therefore their emission line ratios are not described.

The [N II]/H α emission line ratios show significant changes on small scales. In both knots, the clumps (with spatial scales $\leq 0''.4$) show the largest [N II]/H α ratios, with values from ~ 2.0 to 2.4 . Around these clumps the [N II]/H α ranges from 1.0 to 1.5 . The [N II]/H α values are ≤ 1 at the inner edge of the knots (facing towards the central source). These clumps (sizes $\leq 0''.4$) show the lowest [O III]/H α line ratios with values from 1.5 to 2.5 ; we see a gradient in the [O III]/H α ratio map across knot K4, where the [O III]/H α line ratios increase from ~ 2.5 to 3.0 – 4.5 .

The figure 5.40 shows the diagnostic diagrams in the Knots K4 and K1 respectively, in the top row see K4 structure and bottom row the K1 Knot, see in this structure the dispersion is more width in the central part, but in general follow the same line to the other structures.

The profile for the Knots K4 and K1 in NGC 7009 in the figure 5.41 shows the peak of Knots K1 is more width in the top by this structure is elongated, while K4 is more sharp in the top. The intensity distribution in the knots (K4 and K1) is visible in the lines H α and [N II] and the apparent spatial separation is very small, the location of maximum peaks for the K4 is $-2''.63$, while K1 maximum peaks is $2''.48$ in both lines.

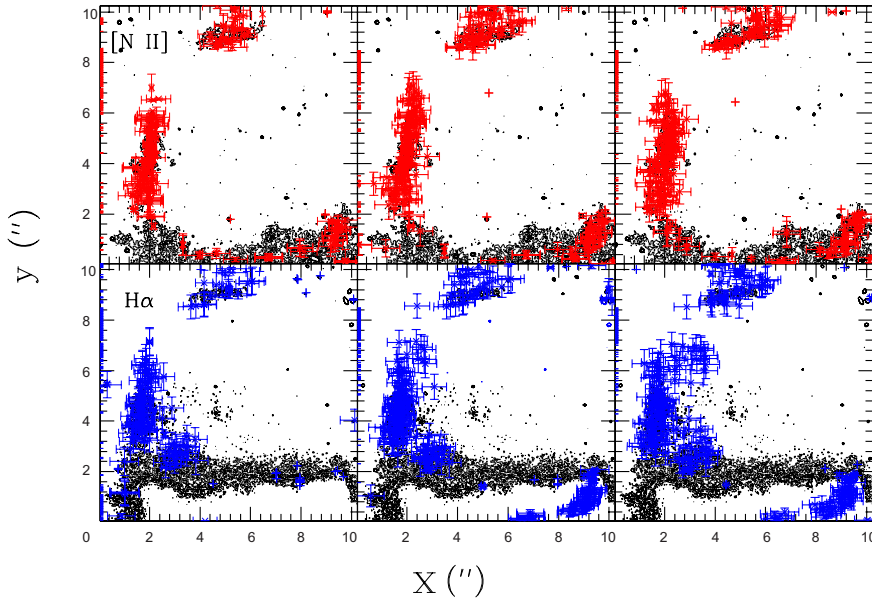


Figure 5.42: Contour plots of the emission lines of M 3-1 where we showing the positions (x_k, y) of the maxima. The characteristic sizes $((a_{x,k}, a_{y,k}))$ are shown as errorbars. [N II] (top panels, red) and H α (bottom panels in blue). Symbols as in figure 5.18.

5.5.7. Additional Objects

To increase the number of objects included in our study, we have added three more PN with FLIERs those that were at least observed with the HST in the [N II] filter.

M 3-1 was observed with the WFPC2/HST with the filters F656N and F658N (figure 5.2). *M 3-1* is a S-shaped PN with two ansae (A and A') radially symmetrical and low-ionization microstructures located at the edge of the main elliptical body of nebulae and symmetrical from the central star. These features are prominent in low ionization lines (Corradi et al. 1996), and were also described as jet-like features (Goncalves et al. 2001). The distance to *M 3-1* is estimated 6.868 kpc (Bown, A.G.A., Vallenari, A., et al. (2018), GAIA Collaboration).

The results obtained from the jet-like features wavelet analysis are shown in figures 5.42, 5.43 and 5.44. From the wavelet analysis, we find that the B feature is wider in the H α image than in the [N II] map, with a mean $\langle a_x \rangle$ in H α of $1''.2$ (i.e., 5×10^{16} cm). The aspect ratio of feature B in H α is more or less constant with a mean value of 1. The width of this feature in the [N II] map shows quite a wide scatter with values $\leq 0''.8$ (i.e. 3.5×10^{16} cm). As a result, the $\langle a_x \rangle / \langle a_y \rangle$ ratio is ≤ 0.6 along feature B. The width of the feature A is similar in both images, showing quite a wide scatter (with values $\leq 1''.0$).

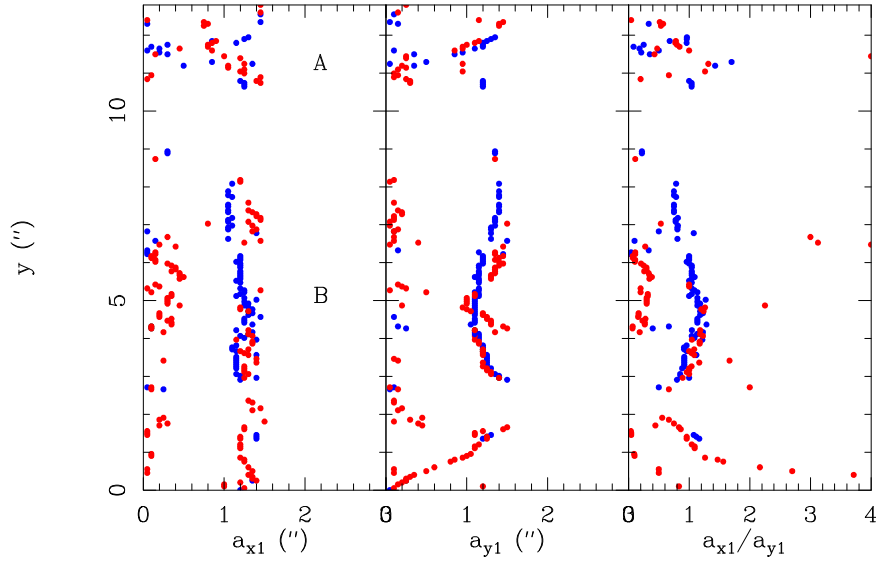


Figure 5.43: Features of wavelets in A and B in M 3-1. Blue circles correspond to $H\alpha$ and red circles correspond to $[N II] 6584 \text{ \AA}$. See text for more details.

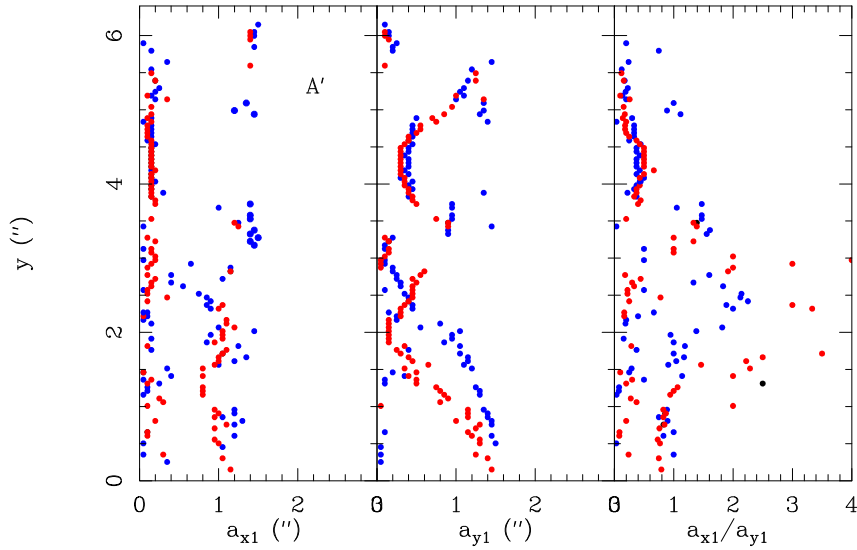


Figure 5.44: Feature wavelet analysis to A' in M 3-1. Symbols as in figure 5.43 See text for more details.

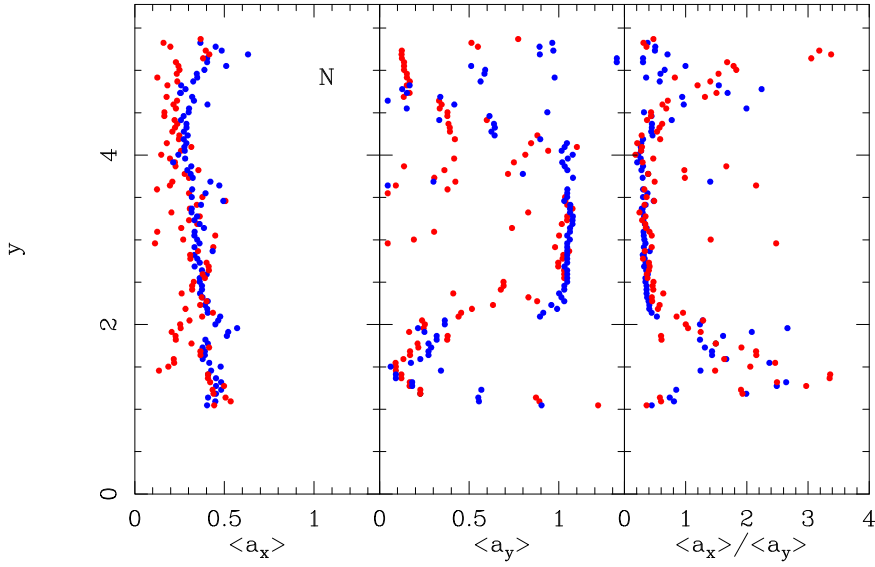


Figure 5.45: Wavelet analysis in Hb 4 to N structure. Symbols as in figure 5.43 See text for more details.

Hb 4 was observed with the WFPC2/HST with the filters F656N and F658N (figure 5.2). *Hb 4* is a high-excitation elliptical nebula with a pair of detached string of knots on either side of the nebula, at $\pm 10''$ from the central source. The major axis of the main elliptical shell seems to be perpendicular to the outflow axis. The central star has been classified as a Wolf Rayet [WC 3-4]. The outer knots (i.e., FLIERs) move at $\pm 150 \text{ km s}^{-1}$ (Danehkar, 2014; López et. al, 1993). The distance adopted to *Hb 4* is 2.297kpc ((Bown, A.G.A., Vallenari, A., et al. (2018), GAIA Collaboration).

Moving away from the central star, we detect a transition from wide to elongated structures at both knots (with an aspect ratio ~ 0.4). At the northern FLIER, the spatial scales across the outflow ($\langle a_x \rangle$) show values from $0''.5$ ($1.4 \times 10^{16} \text{ cm}$) decreasing to $0''.2$ ($5 \times 10^{15} \text{ cm}$) with distance to the central source. The southern FLIER show $\langle a_x \rangle$ from $0''.2$ to $0''.4$ ($\sim 10^{16} \text{ cm}$).

NGC 7354 was observed with the WFPC2/HST with the filters F658N and F502N (see figure 5.2). The [N II] image shows the presence of two elongated (jet-like) features lying along the symmetry axis (Contreras et al. 2010). These low ionization features are not observed in [O III]. The northern jet shows two compact knots at the edge facing the central source and a thin tail that extends away from the central star. From the wavelet analysis (shown in figure 5.47, we find that the knots have a width $\leq 0''.1$ which is unresolved at the present angular resolution. Along the N-tail, the width increases with distance to the

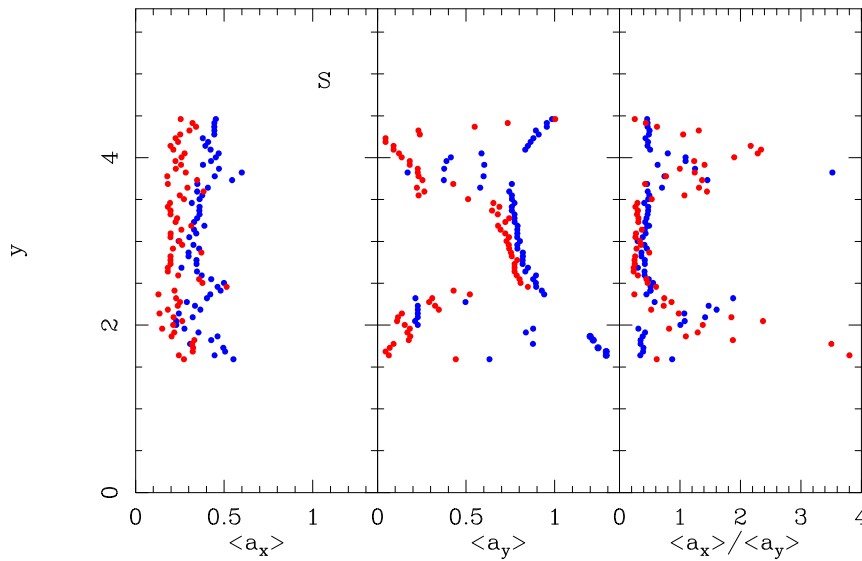


Figure 5.46: Wavelet analysis in Hb 4 to S structure. Symbols as in figure 5.43 See text for more details.

central source up to $0''.7$ (1.2×10^{16} cm). The southern feature shows a knot at the edge facing the central source and an elongated tail (figure 5.47). Its width is unresolved at the present resolution. The a_x/a_y ratio remains below 0.1 for most points. The distance adopted is 2.022 kpc ((Bown, A.G.A., Vallenari, A., et al. (2018), GAIA Collaboration).

5.6. General discussion and conclusions

The contour plot of intensity distribution reveals the apparent spatial distribution between [N II] and $H\alpha$ is displaced a maximum value of $0''.05$ in all PNe and [O III] a maximum value of $0''.18$ respect to $H\alpha$ line.

The wavelet analysis reveals in regions with shocks in the complex structure is present in the [N II]/ $H\alpha$ ratio are between 0,25 to 1,8 with exception of NGC 7009 with a increment in your values of 2,4 while the regions in [O III]/ $H\alpha$ oscillates between 2 to 4. This abrupt increase in the range is a stratification evidence and the regions with shocks.

The pattern of distribution in diagnostic diagrams obtained in the selected sample of planetary nebulae is similar for all structures. In the majority of cases the distribution in [O III]/ $H\alpha$ take values between 2,0 and 2,5 in the other case (displacement to right IC 4593; NGC 6543), while the values in [N II]/ $H\alpha$ scale, oscillate between 0 to 3 units, the segregation is not notable indicating the same excitations conditions in almost all sample.

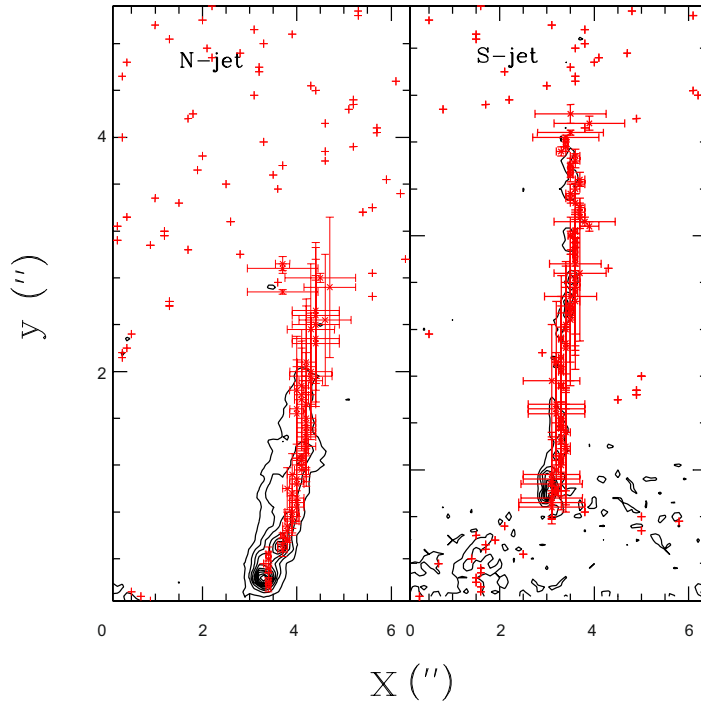


Figure 5.47: [N II] contour plots of the N-jet (left) and S-jet (right) to NGC 7354, where we show the positions of the first maxima. See text for more details.

References

- Amnuel P. R., Guseinov O. H., Novruzova H. I., Rustamov Y. S., 1984, *Ap&SS*, 107, 19.
- Balick, B. 1987, *AJ*, 94, 671.
- Balick, B., Rugers, M., Terzian, Y., & Chengalur, J. N. 1993, *ApJ*, 411, 778.
- Balick, B., Perinotto, M., Maccioni, A., Terzian, Y., & Hajian, A. 1994, *ApJ*, 424, 800.
- Balick B., Frank, A., 2002, *ARA&A*, 40, 439.
- Balick, B. 2004, *AJ*, 127, 2262.
- Bohigas, J., & Olguín, L. 1996, *Rev. Mex. AA*, 32, 47.
- Bond, H. E., Liller, W., & Mannery, E. J. 1978, *ApJ*, 223, 252.
- Bown, A.G.A., Vallenari, A., et al. (2018), *GAIA Collaboration*, Bown, A.G.A., Vallenari, A., et al. 2018, *A&A*, 616, 1.
- Cahn, J. H., Kaler, J. B., & Stanghellini, L. 1992, *A&AS*, 94, 399.
- Cardelli, J. A., Clayton, G. C., & Mathis, J. S. 1989, *ApJ*, 345, 245.
- Contreras M. E., Vázquez R., Miranda L. F., Olgun L., Zavala S., Ayala S., 2010, *AJ*, 139, 1426.
- Corradi, R. L. M., Guerrero, M., Manchado, A., & Mampaso, A. 1997a, *New Astron.*, 2,

461.

Corradi, R. L.M., Manso, R., Mampaso, A., & Schwarz, H. E. 1996, A&A, 313, 913.

Corradi, R. L. M., Perinotto, M., Villaver, E., Mampaso, A., & Gonçalves, D. R. 1999, ApJ, 523, 721.

Corradi, R. L. M., Sánchez-Blázquez, P., Mellema, G., Giammanco, C., & Schwarz, H. E. 2004, A&A, 417, 637.

Cudworth K. M., 1974, AJ, 79, 1384.

Danehkar A., 2014, PhD thesis, Macquarie University.

Ercolano, B., Morisset, C., Barlow, M. J., Storey, P. J., & Liu, X.-W. 2003, MNRAS, 340, 1153.

Faulkner D. J., 1970, ApJ, 162, 513.

Fernández, R., Schwarz, H. E & Monteiro, H. 2004, ASPC, 313, 236.

Finzi A., Wolf E. A., 1971, A&A, 11, 418.

Frew, D. 2008, Ph.D. Thesis, Macquarie University, Sydney, Australia.

Girard, T. M., Dinescu, D. I., van Altena, W. F., Platais, I., Lopez, C. E. & Monet, D. G. 2003, DDA, 34, 702.

Girard, P., Köppen, J., & Acker, A. 2007, A&A, 463, 265.

Gonçalves, D. R., Corradi, R. L. M., & Mampaso, A. 2001, ApJ, 547, 302.

Gonçalves, D. R., Corradi, R. L. M., & Mampaso, A. 2002, in Rev. Mex. Astron.Astrofis. Conf. Ser. 13, eds. W. J. Henney, W. Steffen, L. Binette, & A. Raga, 119.

Gonçalves, D. R., Corradi, R. L. M., Mampaso, A., & Perinotto, M. 2003, ApJ, 597, 975.

Gonçalves, D., Mampaso, A., Corradi, R. L. M., & Perinotto, M. 2004, in ASPConf. Ser 313, Asymmetrical Planetary Nebulae III: Winds, Structure, and the Thunderbird, ed. M. Meixner, et al. (San Francisco: ASP), 198.

Grosdidier, Y., Moffat, A. F. J., Blais-Ouellette, S., Joncas, G. & Acker, A. 2001, ApJ, 562, 753.

Guerrero, M. A., Miranda, L. F., Riera, A., et al. 2008, ApJ, 683, 272.

Guerrero, M. A., Toalá, J. A., Medina, J. J., et al. 2013, A&A, 557, A121.

Hajian A.R., Terzian Y., Bignell C., 1995, AJ, 109, 2600.

Hajian A. R., Balick B., Terzian Y., Perinotto M., 1997, ApJ, 487, 304.

Harm R., Schwarzschild M., 1975, ApJ., 200, 324.

Kutter G. S., Sparks W. M., 1974, ApJ, 192, 447.

Kwitter, K. B., & Henry, R. B. C. 1998, ApJ, 493, 247.

- Kwok S., Purton C.R. and Fitzgerald P.M., 1978,ApJ.(Letters), 219, L125.
- Liu Y., Liu X.-W., Barlow M.J., Luo S.-G., 2004, MNRAS, 353, 1251.
- Lopez, J. A., Roth, M., & Tapia, M. 1993, A&A, 267, 194.
- López J. A., Steffen W., Meaburn J., 1997, ApJ, 485, 697.
- López, J. A. 2000, in Revista Mexicana de Astronomia y Astrofisica Conference Series, Vol. 9, Revista Mexicana de Astronomia y Astrofisica. Conference Series, ed. S. J. Arthur, N. S. Brickhouse, & J. Franco, 201–209.
- López, J. A. 2002, Rev. Mex. Astron. Astrofis. Conf. Ser. 13,139.
- Lucy L. B., 1967, AJ, 72, 813.
- Maciel, W. J. 1984, A&AS, 55, 253.
- Méndez R.H., Kudritzki R.P., Herrero A., 1992, A&A, 260, 329.
- Middlemass, D., Clegg, R. E. S., & Walsh, J. R. 1989a,MNRAS, 239, 5P.
- Miranda L. F., Solf J., 1992, AAP, 260, 397.
- Miszalski, B. et al. 2009, A&A, 505, 249.
- Moreno-Corral, M., de La Fuente, E., & Gutiérrez, F. 1998, Rev. Mexicana Astron. Astrofis., 34, 117.
- O'Connor, J.A., Meburn, J., López, J.A. Redman, M.P. 1999, A&A, 346, 237.
- Patriarchi, P. & Perinotto, M. 1991a, Astronomy and Astrophysics SupplementSeries, 91, 325.
- Peña M., Stasinska G., Medina S., 2001,A&A,367, 983.
- Perinotto, M., Cerruti-Sola, M., & Lamers,H. J. G. L. M. 1989, ApJ, 337, 382.
- Phillips, J. P. 2002, ApJS, 139, 199.
- Phillips J. P., 2003,MNRAS,344, 501.
- Phillips, J. P. 2004, MNRAS, 353, 58.
- Pottasch S. R., Bernard-Salas J., Roellig T. L., 2009a,A&A,499, 249.
- Raga, A. C., Canto, J., Binette, L., & Calvet, N. 1990, ApJ, 364, 601.
- Raga A. C., Riera A., Mellema G., Esquivel A., Velázquez P. F., 2008, A&A, 489, 1141.
- Reay N. K., Atherton P. D., 1985, MNRAS, 215,233.
- Reed, D. S., Balick, B., Hajian, A. R., et al. 1999, AJ, 118, 243.
- Riera, A., Raga, A., Reipurth, B., Amram, P., Boulesteix, J., Canto, J., & Toledano, O.2003, AJ, 126, 327.
- Riera, A., Velázquez, P. F., Raga, A. C., et al. 2014, A&A, 561,A145.
- Rodríguez, L. F. & Gómez, Y. 2007, Rev. Mexicana Astron. Astrofis., 43, 173.

- Robertson-Tessi M., Garnett D. R., 2005, *ApJS*, 157, 371.
- Roxburgh I. W., 1967, *nat*, 215, 838.
- Sabbadin, F., Turatto, M., Cappellaro, E., Benetti, S., & Ragazzoni, R. 2004, *A&A*, 416, 955.
- Sahai R., Trauger J. T., 1998, *AJ*, 116, 1357.
- Smith R. L., Rose W. K., 1972, *ApJ*, 176, 395.
- Sonneborn G., Iping R.C., Herald J., 2009, in Van Steenberg M.E., Sonneborn G., Moos H.W., Blair W.P., eds, *Proc. AIP Conf. Vol. 1135, Future Directions in Ultraviolet Spectroscopy*. AIP, Maryland, p. 177.
- Stanghellini L., Corradi R. L. M., Schwarz H. E., 1993, *AAP*, 279, 521.
- Stanghellini, L., & Shaw, R. A. 2008, *ApJ*, 689, 194.
- Steffen, W., Espíndola, M., Martínez, S., & Koning, N. 2009, *Rev. Mexicana Astron. Astrofis.*, 45, 143.
- Szyszkla, C., Zijlstra, A.A., & Walsh, J.R. 2011, *MNRAS*, 416, 715.
- Toalá et al. (2020); *MNRAS* 494, 3784–3789 (2020).
- Trimble, V., Sackmann, I.-J. 1978, *MNRAS* 182, 97.
- Tuchman, Y., Sack, N., & Barkat, Z. 1979, *ApJ*, 234, 217.
- Tylenda, R., & Stasinska, G. 1994, *A&A*, 288, 897.
- Velázquez P. F., Raga A. C., Riera A., Steffen W., Esquivel A., Cantó J., Haro-Corzo S., 2012, *MNRAS*, 419, 3529.
- Wesson, R., Liu, X.-W. 2004, *MNRAS* 351, 1026.
- Wood, P. R. 1974, *ApJ*, 190, 609.

Conclusiones

El análisis de las 9 nebulosas planetarias arroja evidencias claras sobre una similitud en sus estructuras y la presencia de microestructuras, dados los patrones que arroja el análisis wavelet, donde se observan claramente patrones en forma de “V” (fig 6.1), lo que indica la presencia de knots en las zonas de ionización.

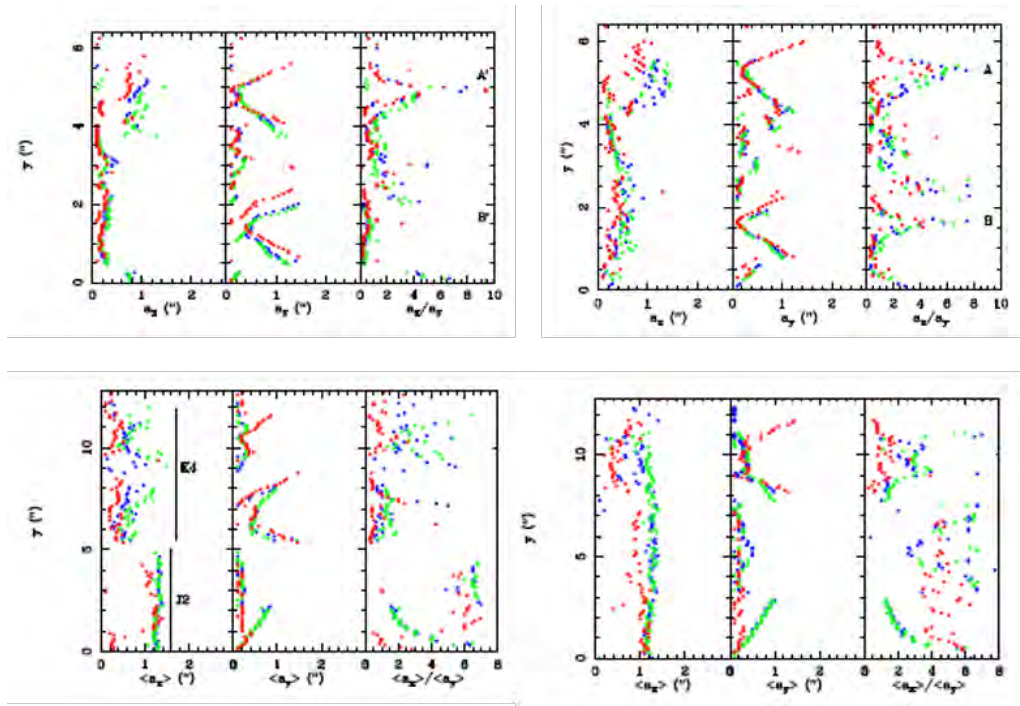


Figura 6.1: Análisis wavelet, donde se visualiza el patrón de la forma “V”. Fuente propia.

Otro de los resultados de interés es el grupo que evidencia diagonales en sus resultados de wavelet (como se ve claramente en la fig 6.2). Este patrón indica la presencia de microestructuras alargadas (jets).

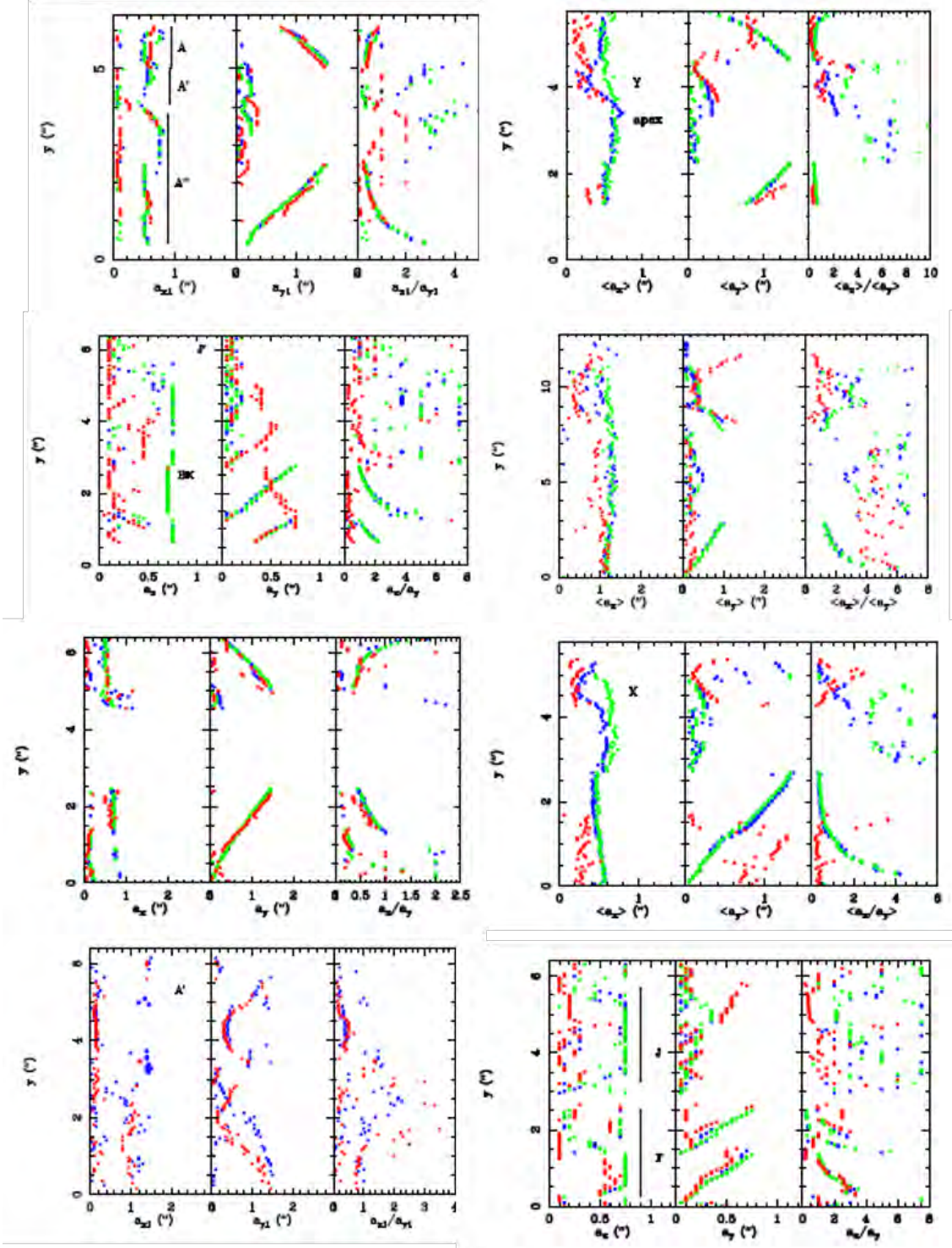


Figura 6.2: Análisis wavelet, donde se visualiza el patrón de la forma diagonal. Fuente propia.

Adicionalmente, se puede observar que todas las distribuciones son bastante compactas en su distribución, no superando $1''$, a excepción de las estructuras de NGC 7009. En general,

el análisis wavelet indica que estas nebulosas presentan microestructuras comunes a saber, knots, jets, jet-like y filamentos.

Los perfiles unidimensionales indican que las microestructuras en su mayoría no presentan desplazamiento espacial en cada una de las líneas de emisión, lo que quiere decir que se encuentran ubicadas a la misma distancia de la estrella central de la nebulosa planetaria. Los cocientes $[\text{O III}]/\text{H}\alpha$ presentan un rango de valores de 0.1 a 4.2 mientras $[\text{N II}]/\text{H}\alpha$ toma valores entre 0.2 y 2.4. Como se aprecia, el cociente de $[\text{O III}]$ dobla al valor de $[\text{N II}]$ (ver fig. 6.3). Este cambio abrupto entre las escalas indica la presencia de microestructuras en las regiones chocadas de las nebulosas planetarias.

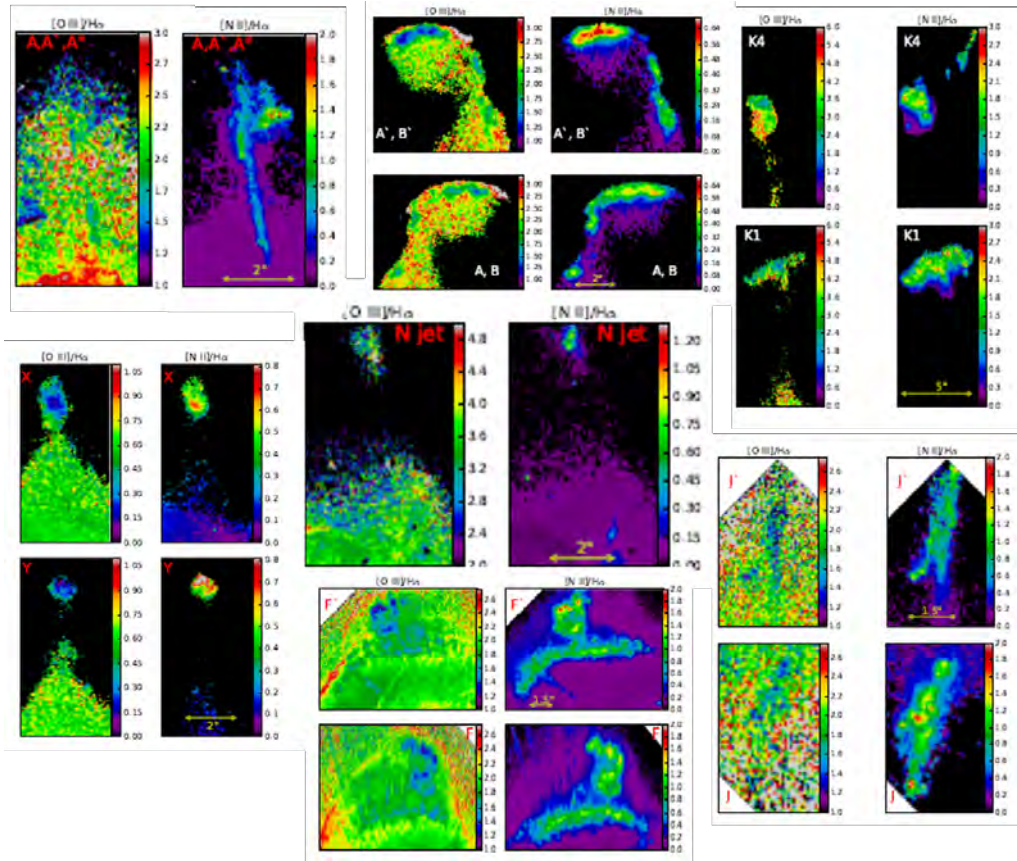


Figura 6.3: Cocientes de líneas de emisión. Fuente propia.

Los diagramas diagnósticos son un fuerte indicador de las zonas estratificadas presentes en los objetos seleccionados, dado que en su patrón de dispersión es bastante similar. Si observamos la imagen de izquierda a derecha (ver fig 6.4), se revela la existencia de 2 zonas bien delimitadas, en su mayoría son dobles ya que la muestra de objetos presenta simetría en su microestructuras. Esas dos zonas deben representar knots y jets.

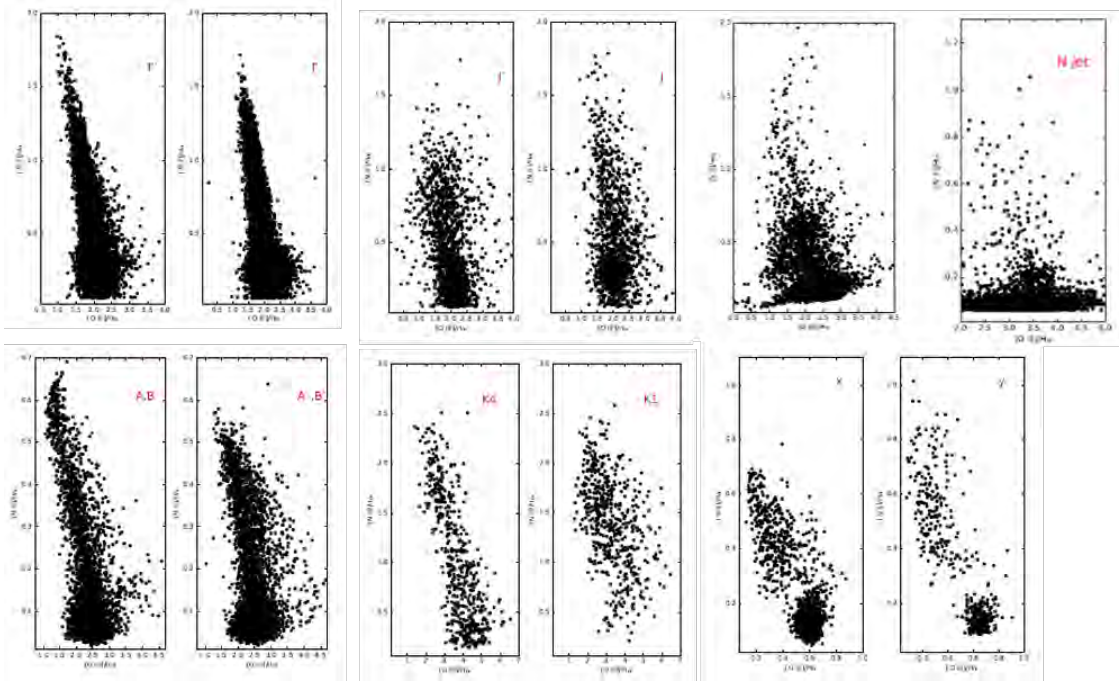


Figura 6.4: Diagramas diagn3sticos, donde se visualizan caracter3sticas similares. Fuente propia.

Para la nebulosa protoplanetaria CRL 618, encontramos que los movimientos propios se encuentran alineados con el eje de los jets y con unas velocidades tangenciales que van desde los 60 a los 430 km s⁻¹. La velocidad tangencial se puede decir que es proporcional a la distancia de la estrella central, es decir a mayor distancia del centro, mayor velocidad. Encontramos que las simulaciones num3ricas realizadas reproducen la morfolog3a y los movimientos propios de CRL 618 cuando se considera un decremento en la velocidad de los jets en funci3n del tiempo.

De la comparaci3n hecha entre la estructura y los movimientos propios observados en CRL 618 y las predicciones de la simulaci3n de jets en 3D, se encuentra que el tama3o y la morfolog3a de los l3bulos y el movimiento de expansi3n de los jets concuerda con las observaciones de CRL 618, de tal forma que se puede explicar su evoluci3n en t3rminos de una eyecci3n bipolar colimada y una precesi3n en el eje de la estrella central.

6.1. Trabajos futuros

Dado que se adquiri3 un conjunto de datos de espectroscopia 3D, se pretende ampliar el estudio de algunas de las nebulosas analizadas en esta tesis, con esta t3cnica, se puede

obtener información unidimensional y bidimensional (a partir de los cubos de datos), (fig 6.5) y de estos análisis obtener abundancias químicas, densidad y temperatura electrónica.

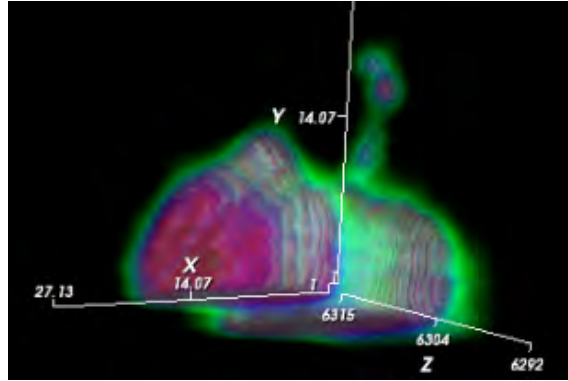


Figura 6.5: Imagen de una sección espectroscópica 3D de NGC 3918. Fuente propia.

También se podrían aplicar técnicas estadísticas, como el método de componentes principales y el método t-SNE (t-distributed stochastic neighbor embedding), las cuales permitirían clasificar y establecer mejor las zonas estratificadas en los diagramas diagnósticos.

Bibliografía

- [1] Abell, G.O. & Goldreich, P. 1966. On the Origin of Planetary Nebulae. *PASP*, 78, 232
- [2] Acker, A.; Neiner, C. 2003. *2003A&A...403..659A*
- [3] Balick, B., Perinotto, M., Maccioni, A., Terzian, Y., Hajian, A. 1994. *Ap. J.* 424, 800
- [4] Blöcker, T. 1995a. Stellar evolution of low and intermediate mass stars. II. Post-AGB evolution. *A&A*, 299, 755.
- [5] Bowen, I. S. 1928. The origin of the nebular lines and the structure of the planetary nebulae. *Apj*, 67, 1
- [6] Cardelli, J. A., Clayton, G. C., Mathis, J. S. 1989. *1989ApJ...345..245C*
- [7] Castrillón, A., Riera, A., Lopez, R., and Aquines, O. 2021. En proceso
- [8] De Boer; Seggewiss; 2008. *Stars and Stellar Evolution*. EDP Sciences
- [9] De Marco, O. 2008. *2008ASPC..391..209D*
- [10] De Marco, O; Soker, Noam. 2002. *2002PASP..114..602D*
- [11] Dopita, M. Sutherland, R. 2005. *Astrophysics of the diffuse universe*. Springer.
- [12] Faulkner, D. J. 1970, *ApJ*, 162, 513
- [13] Fernández, M. A. 2013. Estructura de ionización y composición química de nebulosas Galácticas. Tesis doctoral
- [14] Finzi, A., & Wolf, R. A. 1971, *A&A*, 11, 418
- [15] Fogel, J.; De Marco, O.; Jacoby, G. 2003. *2003IAUS..209..235F*
- [16] García, J. 2009. Abundancias químicas en regiones H II y fluctuaciones de temperatura. Tesis doctoral
- [17] Gonçalves DR, Corradi RLM, Mampaso A. 2001. *Ap. J.* 547, 302
- [18] Górny, S. K.; Stasińska, G.; Escudero, A. V. 2004. *2004A&A...427..231G*
- [19] Griffiths, M. 2012. *Planetary Nebulae and How to Observe Them*. Springer
- [20] Guerrero, Martín A. 2000. *2000ASPC..199..371G*

- [21] Habing, H. & Olofsson, H. Asymptotic Giant Branch Stars. Springer. 2004
- [22] Hajduk, M., Zijlstra, A. A., Gesicki, K. 2010. Mon. Not. R. Astron. Soc. 406, 626–633
- [23] Härm, R., & Schwarzschild, M. 1975, ApJ, 200, 324
- [24] Herschel, W. 1791. On Nebulous Stars, Properly So Called. By William Herschel, LL.D.F.R.S. Royal Society of London Philosophical Transactions Series I, 81, 71
- [25] Herwig, F. 2005. Evolution of Asymptotic Giant Branch Stars. ARA&A, 43, 435
- [26] Hubble, E.P. 1922. The source of luminosity in galactic nebulae. Apj, 56, 400
- [27] Huggins, W., & Miller, W. A. 1864. On the spectra of Some of the Nebulae. By William Huggins, F.R.A.S. A Supplement to the paper “On the Spectre of Some of the Fixed Star William Huggins F.R.A.S., and W. A. Miller, M.D., LL.D., Treas. and V.P.P.S.”. Royal Society of the London Philosophical Transactions Series I, 154, 437
- [28] Iben, Jr., I. 1995. Planetary nebulae and their central stars - origin and evolution. Phys. Rep., 250, 2
- [29] Iben, Jr., I. 1975. Thermal pulses; p capture, alpha capture, s-process nucleosynthesis; and convective mixing in a star of intermediate mass. Apj, 196, 525
- [30] Iben, Jr., I. & Renzini, A. 1983. Asymptotic giant branch evolution and beyond. ARA&A, 21, 271
- [31] Kamath, D., Wood, P., Van Wickel, H. 2015. 2015MNRAS.454.1468K
- [32] Karakas, A. I., Lattanzio, J. C. & Pols, O. R. 2002. Parameterising the Third Dredge up in Asymptotic giant Branch Stars. PASA, 19, 515.
- [33] Krugel, E. K., 2003. The Physics of Interstellar Dust. CRC Press
- [34] Kwok, S., Purton, C. R., & Fitzgerald, P. M. 1978. On the origin of planetary nebulae. Apj, 219, L125
- [35] Kwok, S. The Origin and Evolution of Planetary Nebulae. Cambridge University Press. 2000
- [36] Lattanzio, J. 2003. Planetary nebulae: Their evolution and role in the universe. IAU S, vol 209
- [37] Lattanzio, J. 2003. 3D stellar Evolution. ASP conference series, Vol. 293
- [38] Lattanzio, J., Forestini M., 1999, In: IAU Symp. 191: Asymptotic Giant Branch Stars, p. 31
- [39] López, JA., Roth, M., Tapi, M. 1993. Rev. Mex. Astron. Astrofis. 26, 110
- [40] López, JA. 1997. See Habing & Lamers 1997, p. 180
- [41] Lucy, L. B. 1967; AJ, 72, 813

-
- [42] Maciel, Costa & Idiart, 2009. *RMA&A* 45, 127
- [43] Manchado, A. Guerrero., M. A.. Stanghellini, L. and Serra-Ricart. M. 1997. he IAC morphological catalog of Northern Galactic Planetary Nebulae. Symposium - International Astronomical Union, 180, 24-25.
- [44] McMaster, Biretta, et al. 2008, *WFPC2 Instrument Handbook*, Version10.0 (Baltimore: STScI).
- [45] Meaburn, J., Clayton, CA., Bryce, M., Walsh, JR., Holloway, AJ., Steffen, W. 1998. *MNRAS* 294, 201
- [46] Menzel, D.H. 1926. The Planetary nebulae. *PASP*, 38. 295
- [47] Messier, C.1781. Catalogue des Nébuleuses & des amas d'Étoiles. Connaissance des Temps for 1784
- [48] Miszalski, B.; Acker, A.; Moffat, A. F. J.2009.*2009A&A...496..813M*
- [49] Osterbrock, D. E & Ferland, G. j. 2006. Astrophysics of gaseous nebulae and active galactic nuclei. University Science Books
- [50] Paczyński, B. 1970.*Acta Astr.* 20, 47
- [51] Paczyński, B. 1971. Evolution of Single stars. VI. Model Nuclei of Planetary Nebulae. *Acta Astronómica*, 21, 417
- [52] Paczyński, B., Ziolkowski, J. 1968. *IAUS*. 34. 396p
- [53] Pijpers FP, Habing HJ. 1989. *Astron. Astrophys.* 215, 334
- [54] Riera, A., Raga, A. C., Reipurth, B., Amram, P., Boulesteix, J., Cantó, J. & Toledano, O. 2003, *AJ*, 126, 327
- [55] A. Riera, P. F. Velázquez, A. C. Raga, R. Estalella, and A. Castrillón. 2014. *A&A* 561, A145 (2014)
- [56] Roxburgh, I. W. 1967, *Nature*, 215, 838
- [57] Salaris & Cassisi. 2005, *Evolution of Stars and Stellar Populations*. John Wiley and Sons. pp. 119–121.
- [58] Salas, J. B. 2003. Physics and Chemistry of Gas in Planetary Nebulae. PhD Thesis
- [59] Schönberner, D. 1981. Late stages of stellar evolution I- central stars of planetary nebulae. *A&A*, 103, 119
- [60] Schönberner, D. 1979. *1979A&A....79..108S*
- [61] Secchi, A. 1867. Spectral Studies on Some of the Planetary Nebulae. *Astronomical register*. 5, 40
- [62] Shklovsky, I. 1956a. *Ast. Zh.*, 33, 315

- [63] Shklovsky, I. 1956b. *Ast. Zh.* 33, 222
- [64] Smith, L. F. & Aller, L. H. 1969. On the Classification of Emission Line Spectra of Planetary Nuclei. *Apj*, 157, 1245
- [65] Smith, R. L., & Rose, W. K. 1972, *ApJ*, 176, 395
- [66] Szyszka, C., Zijlstra, A., Walsh, J. 2011. *Mon. Not. R. Astrn. Soc.* 416, 715-726
- [67] Trimble, V., & Sackman, I. J. 1978, *MNRAS*, 182, 97
- [68] Tylenda, R.; Stasińska, G. 1989. 1989A&A...217..209T
- [69] Tylenda, R.; Acker, A.; Stenholm, B. 1993. 1993A&AS..102..595T
- [70] Vassiliadis, E. & Wood, P. R. 1993. Evolution of low and intermediate mass stars to the end of the asymptotic giant branch with mass loss. *Apj*, 413, 641.
- [71] Vassiliadis, E. & Wood, P. R. 1994. *ApjS*, 92, 125.
- [72] Weidmann, W., Méndez, R., Gamen, R. 2015 *A&A*, 579 (2015) A86
- [73] Werner, K. & Herwig, F. 2006. *PASP*, 118, 183.
- [74] Wood, P. R. 1974. *ApJ*, 190, 609
- [75] Zanstra, H. 1927. An Application of the Quantum Theory to the Luminosity of Diffuse Nebulae. *Apj*, 65, 50

A

Apéndice 1

A.1. Imágenes

A continuación se presentan las imágenes de las nebulosas planetarias analizadas en esta tesis.

A.1.1. IC 4634

Nebulosa planetaria

ID: IC 4634

Constelación: Ophiuchus



Figura A.1: IC 4634. Fuente: <https://esahubble.org/images/potw1003a/>

A.1.2. IC 4593

Nebulosa planetaria

ID: IC 4593

Constelación: Hercules



Figura A.2: IC 4593. Fuente: <https://esahubble.org/images/opo0733d/>

A.1.3. NGC 3918

Nebulosa planetaria

ID: NGC 3918 - Saturn nebula

Constelación: Centaurus



Figura A.3: NGC 3918. Fuente: <https://esahubble.org/images/potw1015a/>

A.1.4. NGC 6210

Nebulosa planetaria

ID: NGC 6210

Constelación: Hercules

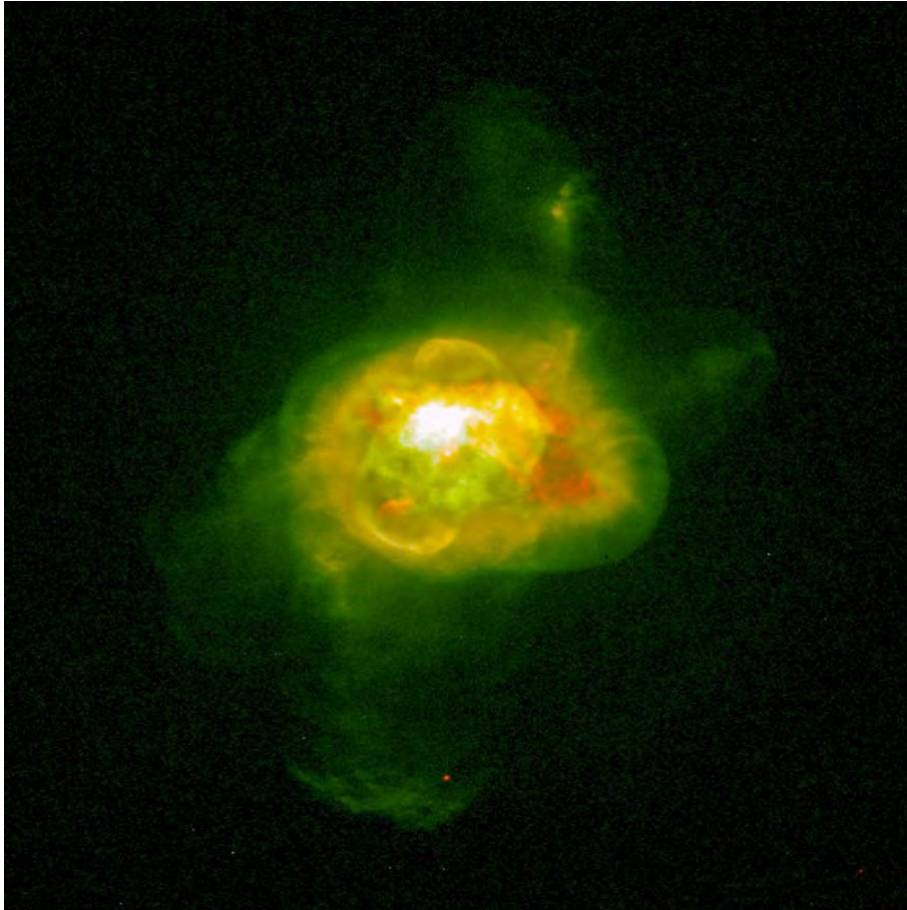


Figura A.4: NGC 6210. Fuente: <https://esahubble.org/images/opo9836f/>

A.1.5. NGC 6543

Nebulosa planetaria

ID: NGC 6543 - Cat's Eye Nebula

Constelación: Draco



Figura A.5: NGC 6543. Fuente: <https://esahubble.org/images/heic0414a/>

A.1.6. NGC 7009

Nebulosa planetaria

ID: NGC 7009 - Saturn nebula

Constelación: Aquarius



Figura A.6: NGC 7009. <https://esahubble.org/images/opo9738g/>

A.1.7. NGC 7354

Nebulosa planetaria

ID: NGC 7354

Constelación: Cepheus

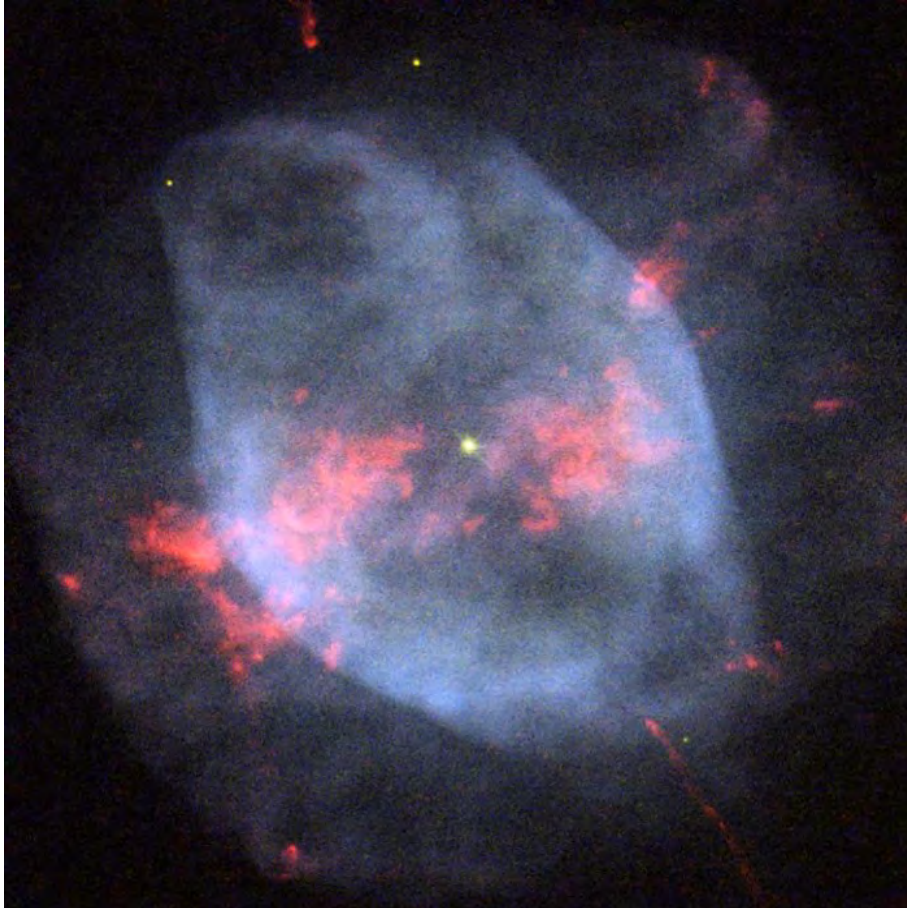


Figura A.7: NGC 7354. <https://esahubble.org/images/potw1250a/>

A.1.8. PN Hb 4

Nebulosa planetaria

ID: PN Hb4

Constelación: Ophiuchus



Figura A.8: PN Hb4.

https://faculty.washington.edu/balick/PNIC/PNimages_by_galcoord/003-102.9.Hb4hst.jpg

A.1.9. M 3-1

Nebulosa planetaria

ID: M 3-1

Constelación: Canis Major



Figura A.9: M 3-1. <https://www.flickr.com/photos/geckzilla/43710246990/in/photolist-29AwrA7>

A.1.10. CRL 618

Nebulosa protoplanetaria

ID: CRL 618- Westbrock nebula

Constelación: Auriga

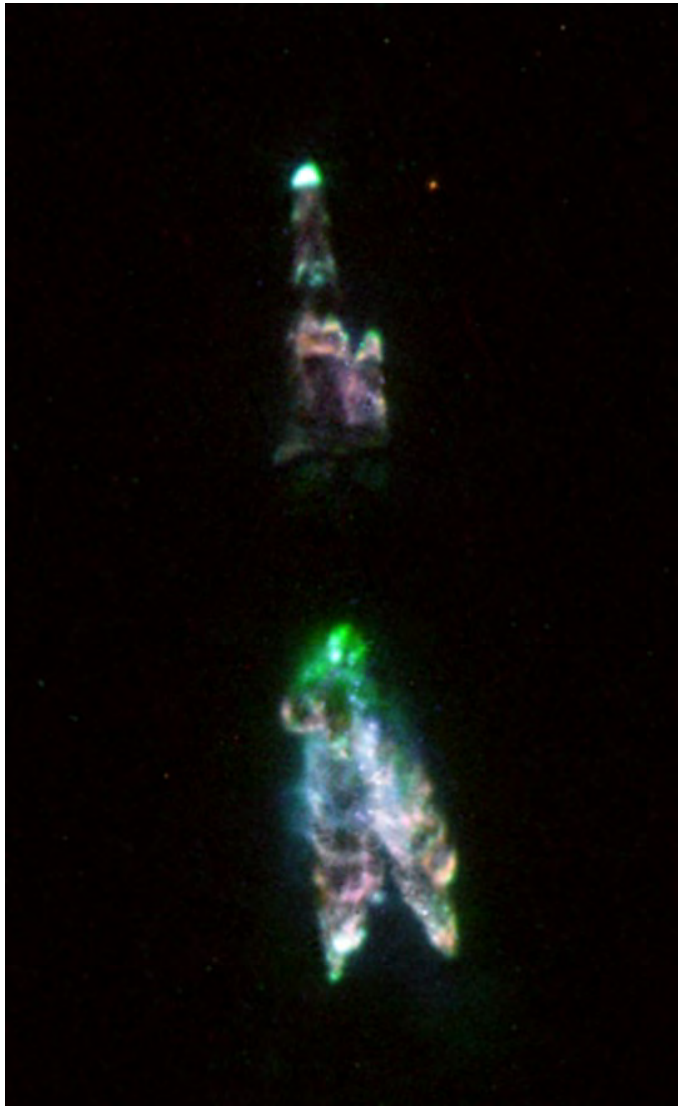


Figura A.10: Nebulosa protoplanetaria CRL 618. Fuente: [https://esahubble.org/images-heic0004a/](https://esahubble.org/images/heic0004a/)